Master Thesis in Geographical Information Science nr 214

Machine Learning–Driven Assessment of Urban Heat Island Intensity in Athens: Integrating Remote Sensing, Landscape Metrics, and Green Infrastructure for Climate-Resilient Urban Planning.

Athanasios Fyntanidis

2026

Department of Earth and

Environmental Sciences (MGeo)

Lund University
Sölvegatan 12

S-223 62 Lund

Sweden

Athanasios Fyntanidis (2026)

Title: Machine Learning–Driven Assessment of Urban Heat Island Intensity in Athens: Integrating Remote Sensing, Landscape Metrics, and Green Infrastructure for Climate-Resilient Urban Planning.

Master thesis, 30 credits in Master in Geographical Information Science

Supervisors: Pengxiang Zhao and Rachid Oucheikh,

Department of Earth and Environmental Sciences (MGeo), Lund University

Page intentionally left blank

Machine Learning–Driven Assessment of Urban Heat Island Intensity in Athens: Integrating Remote Sensing, Landscape Metrics, and Green Infrastructure for Climate-Resilient Urban Planning.

Athanasios Fyntanidis

Master thesis, 30 credits in Master in Geographical Information Science

Supervisors: Pengxiang Zhao Rachid Oucheikh,

Department of Earth and Environmental Sciences (MGeo), Lund University

Acknowledgements

This thesis signifies the final step of my studies in the Master’s Program in Geographic Information Systems at Lund University. I would first like to express my sincere gratitude to my supervisors, Pengxiang Zhao and Rachid Oucheikh, for their continuous guidance, encouragement, and constructive feedback throughout this project. Their insights and support were essential in shaping both the direction and the quality of this research.

Most importantly, I wish to thank my wife, Magdalini Kontidou, for her endless patience, understanding, and love. To my children, Angeliki and Michail, thank you for your smile every day and night. I hope I was an example for you, to never stop gaining knowledge.

Page intentionally left blank

Abstract

Environmental and health risks are increasing in large Mediterranean cities like Athens, where high urban density and limited vegetation intensify the Urban Heat Island (UHI) effect. This study analyzes the spatial patterns of surface urban heat in Athens, Greece, using satellite-derived Land Surface Temperature (LST) as a proxy for UHI conditions. LST datasets were derived from Landsat 8 thermal imagery and Sentinel-2 forecasts within Google Earth Engine (GEE) to achieve a high-resolution 10 m grid. Environmental variables, including vegetation (NDVI), building intensity (NDBI), and topography (DEM and slope), were analyzed alongside landscape metrics (PLAND, LPI, FRAC, ED, and LSI) to quantify the influence of both urban composition and spatial configuration.

The research implemented a dual-track predictive framework: neighborhood-level machine learning models—Random Forest (RF), Support Vector Regression (SVR), Decision Tree (DT), and XGBoost—and a pixel-level Convolutional Neural Network (CNN) for spatial prediction. Results demonstrate that building intensity (NDBI) is the dominant driver of higher surface temperatures, while vegetation (NDVI) and topography contribute to localized cooling. Among the neighborhood-level models, Random Forest demonstrated the most consistent performance, achieving a maximum coefficient of determination (R^2) of 0.5153 in August and a Root Mean Squared Error (RMSE) of approximately 1.75°C. In contrast, although the CNN model had low statistical accuracy ($R^2 < 0.20$), due to data configurations and sensor noise, it managed to capture thermal points that were invisible in tables.

Finally, the study highlights the great importance of integrating remote sensing, GIS-based landscape measurements, and machine learning for the changes that the climate crisis will bring. It thus appears that urban planning, at least in Mediterranean cities, should go a step beyond simple green space and, to more effectively address heat, should take into account spatial geometry and topographic factors. However, the study was limited by the small sample size of 53 administrative neighborhoods, thus limiting the statistical power of high-variance models such as XGBoost and CNN.

Keywords: Urban Heat Island (UHI); Land Surface Temperature (LST); Athens; Remote Sensing; Google Earth Engine (GEE); Landscape Metrics; Machine Learning; Support Vector Regression (SVR); Random Forest (RF); Convolutional Neural Network (CNN); Urban Planning; Climate Resilience.

Page intentionally left blank

Table of contents

Contents

List of Figures

List of Tables

List of Abbreviations

ABBREVIATION	DEFINITION
AOI	Area of Interest
CNN	Convolutional Neural Network
DEM	Digital Elevation Model
DT	Decision Tree
ED	Edge Density
ESA	European Space Agency
FRAC	Fractal Dimension Index
GEE	Google Earth Engine
GIS	Geographic Information System
GWR	Geographically Weighted Regression
HR	High Resolution
LPI	Largest Patch Index
LST	Land Surface Temperature
LSI	Landscape Shape Index
MAE	Mean Absolute Error
ML	Machine Learning
MSE	Mean Squared Error
NDBI	Normalized Difference Built-Up Index
NDVI	Normalized Difference Vegetation Index
PLAND	Percentage of Landscape
RF	Random Forest
RMSE	Root Mean Square Error
R^2	Coefficient of Determination
SRTM	Shuttle Radar Topography Mission
SVR	Support Vector Regression
SWIR	Shortwave Infrared
TOA	Top of Atmosphere
UHI	Urban Heat Island

UTM	Universal Transverse Mercator
VIS	Visible (spectral region)

Glossary

TERM	DEFINITION
ACCURACY ASSESSMENT	The evaluation of how closely predicted or classified values match reference or observed data. In this study, model accuracy was expressed through statistical metrics such as R^2, MAE, and MSE.
AREA OF INTEREST (AOI)	The spatial boundary used to subset and analyze geospatial data — in this case, the administrative limits of Athens and its neighborhoods.
CONVOLUTIONAL NEURAL NETWORK (CNN)	A deep learning architecture capable of detecting spatial patterns and contextual relationships within raster data. Used here to predict pixel-level LST.
DIGITAL ELEVATION MODEL (DEM)	A raster dataset representing the elevation of the Earth's surface. Used to calculate slope, aspect, and hillshade for topographic analysis.
EDGE DENSITY (ED)	A landscape metric expressing the total length of edge segments per unit area, indicating spatial fragmentation.
EMISSIVITY	The efficiency of a surface in emitting thermal radiation compared to a perfect blackbody; a key factor in LST derivation.
FRACTAL DIMENSION INDEX (FRAC)	A measure of the complexity of patch shape in landscape analysis. Higher FRAC values indicate more irregular patch geometry.
GEOGRAPHICALLY WEIGHTED REGRESSION (GWR)	A spatial statistical technique that allows model parameters to vary across space, capturing local variations in relationships.
GOOGLE EARTH ENGINE (GEE)	A cloud-based geospatial platform used for large-scale environmental data analysis and remote sensing processing.
LAND COVER	The physical material present on the Earth's surface, such as vegetation, built-up areas, water, or bare soil.
LAND SURFACE TEMPERATURE (LST)	The radiative skin temperature of the land derived from thermal infrared satellite data; used as a proxy for Urban Heat Island analysis.

LANDSCAPE METRICS	Quantitative indicators describing the composition and spatial configuration of land-cover patches within a landscape (e.g., PLAND, LPI, FRAC, ED, LSI).
LARGEST PATCH INDEX (LPI)	The percentage of total landscape area occupied by the largest patch of a given land-cover class.
MEAN ABSOLUTE ERROR (MAE)	The average magnitude of prediction errors in a regression model, measured in degrees Celsius for LST.
MEAN SQUARED ERROR (MSE)	The average of squared prediction errors, reflecting both the variance and bias of model predictions.
NORMALIZED DIFFERENCE BUILT-UP INDEX (NDBI)	A spectral index derived from SWIR and NIR bands to quantify built-up surface intensity.
NORMALIZED DIFFERENCE VEGETATION INDEX (NDVI)	A spectral index derived from NIR and red bands to measure vegetation greenness and health.
PERCENTAGE OF LANDSCAPE (PLAND)	The proportion (%) of a particular land-cover class within the total landscape area.
RANDOM FOREST (RF)	An ensemble machine-learning algorithm that builds multiple decision trees and averages their outputs to improve prediction accuracy and reduce overfitting.
SUPPORT VECTOR REGRESSION (SVR)	A regression algorithm based on support vector machines that finds a hyperplane minimizing prediction error while maximizing generalization.
URBAN HEAT ISLAND (UHI)	A climatological phenomenon where urban areas experience higher temperatures than surrounding rural areas due to human activities and surface modifications.
XGBOOST (EXTREME GRADIENT BOOSTING)	A high-performance tree-based algorithm that improves predictive accuracy through boosting and regularization techniques.

1.Introduction

1.1 Background

The land cover and thermal dynamics of cities have changed dramatically due to urbanization, resulting in an increased Urban Heat Island (UHI) effect. In Mediterranean cities (such as Athens), heat stress is worsened by dense built forms, with limited vegetation and complex topographies (Zoulia et al., 2009; (Georgakis & Santamouris, 2020). The UHI phenomenon is not only a climate issue but is also, increasingly, a public health issue; heat-related mortality is on the rise across Europe (Schwaab et al., 2023).

Advanced remote sensing technologies—particularly Landsat 8 and Sentinel-2—have facilitated high-resolution mapping of Land Surface Temperature (LST), and have provide new insights into spatial patterns of urban heat. While the Urban Heat Island (UHI) phenomenon refers to differences in near-surface air temperature between urban and rural environments, satellite-derived LST is widely used as a proxy to analyze surface expressions of urban heat. At the same time, these data sources can be combined with a corresponding range of GIS-based landscape metrics and topographic analysis, enabling researchers to expose spatial relationships between heat intensity, vegetation cover, and urban form (Liu et al., 2022).

Green infrastructure, particularly green roofs and urban trees, is essential to reducing UHI through shading and evapotranspiration. Research conducted in Athens and other European cities has shown that increased vegetation significantly decreases LST (Spyrou et al., 2024; Schwaab et al., 2023; Lacroix & Stamatiou, 2021). Additionally, the ability of urban trees to withstand climate stresses is important for long-term urban adaptation.

1.2 Problem Statement and Research Objectives

While there has been an increasing recognition of the Urban Heat Island (UHI) phenomenon and its negative impacts on the environment and public health, there are few predictive models that combine Land Surface Temperature (LST) data with urban characteristics at a detailed scale, especially in Mediterranean cities like Athens. Previous research has generally measured temperature distributions using spatial analysis, or examining the simple relationship between temperature and vegetation and/or built environment indices. However, urban heat dynamics are highly heterogenous and are strongly influenced at the neighborhood scale by neighborhood-specific characteristics, including vegetation cover, density of the built environment, and topography (Herold et al., 2005).

There are some research gaps that remain evident in the literature. There is a lack of neighborhood scale studies of UHI Patterns, where different urban morphologies can lead to various local thermal conditions (McGarigal et al., 2015) There is limited use of landscape analysis Tools, such as FRAGSTATS, to quantify spatial patterns as predictors within Machine Learning models for

UHI studies (McGarigal et al., 2015). Traditional Statistical Techniques often do not account for the Nonlinear Nature of Urban Heat Processes, thus, there is a need for Machine Learning Techniques to model Complex Spatial Relationships (Breiman, 2001; Chen & Guestrin, 2016;Smola & Schölkopf; 2004,Vapnik, 1995).

This study aims to address these gaps by integrating remote sensing–derived LST data, GIS-based landscape metrics, and machine learning techniques to analyze and predict spatial patterns of urban heat in Athens.

1.3 Research Questions

This study is guided by the following research questions:

- **Primary Question:**

  How can machine learning models be used to analyze spatial patterns of surface urban heat in Athens using satellite-derived Land Surface Temperature (LST), and what relationships can be identified between LST and environmental factors such as vegetation cover, built-up intensity, landscape structure, and topography?

- **Secondary Questions:**

  What are the spatial patterns of surface urban heat across Athens based on LST data, and how do these patterns vary among neighborhoods with different levels of vegetation and built-up density?

  Which environmental variables—such as NDVI, NDBI, landscape metrics (PLAND, LPI, ED, FRAC, LSI), and topographic factors (DEM and slope)—are the most significant predictors of LST, and which machine learning models provide the highest predictive accuracy?

To answer these questions, we will create a GIS-based analytic framework that synthesizes remote sensing data, landscape metrics, and machine learning approaches. This will allow us to characterize the principal drivers of UHI intensity and provide spatially explicit, data-driven recommendations for sustainable urban development and climate adaptation strategies for Athens.

1.4 Significance of the Study

The present study contributes to the interdisciplinary area of geospatial climate analytics by incorporating remote sensing, GIS, and ML to address issues of urban heat, building on of recent studies in landscape ecology, urban sustainability, and smart city planning (Birch & Wachter, 2011). The findings are expected to support evidence-based planning for climate resilience, public health, and sustainable urban design—especially in Mediterranean cities facing increasing thermal stress (Alberti, 2005; Gill et al., 2007).

2.Literature Review

2.1 Urban Heat Island (UHI) and Land Surface Temperature (LST)

The Urban Heat Island (UHI) refers to the observed occurrence of cities having higher temperatures than surrounding rural areas due to human heat, impervious or built surfaces, and a lack of vegetation. The UHI effect is intensified in cities in the Mediterranean region such as Athens due to urban morphology (the way in which buildings are built) and insufficient green infrastructure (Zoulia et al., 2009; Georgakis & Santamouris, 2020). Land surface temperature (LST) from thermal remote sensing is a key metric for measuring surface heat and for mapping UHI (Weng, 2004).

Recent advances in satellite remote sensing, particularly through datasets such as Landsat 8 and Sentinel-2, have improved the spatial analysis of urban heat phenomena. Some of the bands of Landsat 8 (Thermal infrared) can be applied to calculate Land Surface Temperature (LST), and high-resolution optical imagery from Sentinel-2 can be used to create auxiliary indexes (e.g., NDVI, NDBI) and assist in the spatial analysis of urban areas (Zha et al., 2003). Using cloud-based platforms for processing and integrating these datasets can support mapping urban thermal patterns (Spyrou et al., 2024; Onačillová et al., 2022). Weather stations cannot provide high-resolution spatial detail, such as satellite-derived land surface temperature (LST), and so a major limitation is the reliance on "snapshots" that do not measure daily heat absorption and release (Yu et al., 2020).

2.2 Urban Greenery and UHI Mitigation

Urban vegetation areas play an important role in mitigating city heat through shading, evapotranspiration, and surface cooling processes. A lot of studies for large cities have demonstrated a significant relationship between vegetation regions and drops in land surface temperature (LST), particularly in areas with tree canopy density and green zones such as parks and green roofs (Schwaab et al., 2023, Lacroix & Stamatiou, 2021). In Greece, and particularly in Athens, recent research has shown that green solutions, including urban green zones and green roofs, can significantly reduce surface temperatures during heat waves (Spyrou et al., 2024).

However, other research suggests that spatial configuration influences urban thermal patterns, not only the quantity of vegetation referred to above. The spatial arrangement, fragmentation, and connectivity of green spaces can affect local cooling efficiency and heat distribution across the urban landscape. Landscape metrics can quantify these spatial characteristics, some of which are patch density, edge density, and landscape shape indices, and have been applied in many studies examining relationships between urban arrangement and LST patterns (McGarigal et al., 2015). These metrics can be calculated using tools such as FRAGSTATS, which aids the systematic analysis of spatial landscape structure and its influence on environmental processes (McGarigal et al., 2015). Thus, landscape metrics can provide useful information for including spatial patterns of vegetation and built-up areas into urban heat modelling. Where studies focus on the total percentage of vegetation (PLAND), they overlook how and whether spatial configuration – that is, the fragmentation or geometric complexity of green areas – limits cooling in nearby residential blocks.

2.3 Built Environment and Topography

The physical characteristics of the built environment, usually referred to as urban form, and influence the intensity and spatial distribution of Urban Heat Islands (UHI). High amounts of impervious surfaces and dense built-up structures result in increased surface temperatures because they store and re-emit the solar radiation, while reducing evapotranspiration and airflow within the urban fabric (Oke, 1982; Santamouris, 2015; Georgakis & Santamouris, 2020). In this study, characteristics of urban areas are represented with the help of remote sensing indices and landscape metrics, including the Normalized Difference Built-up Index (NDBI) and spatial configuration metrics such as PLAND, LPI, FRAC, ED, and LSI (McGarigal et al., 2015). These indicators capture the spatial distribution and fragmentation of built-up and green areas, which are the most important in influencing surface thermal patterns.

In addition to building structures, some topographic characteristics can affect surface temperature. Elevation and slope affect local microclimates because they distribute solar radiation exposure, air circulation, and cold air drainage. In a very complex urban environment such as Athens, where terrain varies between plains and surrounding hills near the coast, Digital Elevation Model (DEM) and slope data help the spatial representation of thermal variability (Roukounakis et al., 2023; Cetin 2021). Finally, topographic variables such as slope and elevation often should not be excluded from urban thermal models in cities such as Athens, due to their role in defining ventilation corridors.

Urban greenery has the potential to cool the area and the built environment has the potential to retain heat. In an environment like Athens, it is possible that high-density “urban canyons” that restrict air flow can neutralize any temperature reduction from a green park. Therefore, understanding the Urban Heat Island (UHI) and analyzing the biophysical cooling factors and the structural heating factors becomes essential (Georgakis & Santamouris, 2020; Oke 1982).

2.4 GIS and Remote Sensing Applications

Remote sensing and Geographic Information Systems (GIS) are essential for analyzing the urban heat island characteristics because they allow the processing of spatial data as well as visualizing that data and developing models of the urban environment. Researchers can combine satellite imagery, environmental variables, and spatial analyses together on platforms like ArcGIS Pro and Google Earth Engine (GEE) to study where urban heat is located and why it occurs (Weng, 2004; Li et al.,2013; Onačillová et al.,2022).

A lot of tools and workflows have been created that support GIS-based analyses of UHI. One such tool is the ArcUHI add-in that combines machine learning with spatial analysis to create a geospatial workflow. Other tools provide analytical applications but not universally suitable models, and the new automated UHI modelling which work with machine-learning, remains an area of research in progress (Stessens et al., 2021; Higgs et al., 2021).

GIS methods have also been used to create UHI maps and more, as well as analyze spatial distribution and access to green space in a city environment. These analyses have demonstrated examples of spatial inequalities in urban green space and have provided insight into how these inequalities affect future strategies for localized cooling in urban areas. (Stessens et al., 2021; Higgs et al., 2021).

2.5 Machine Learning in UHI Modeling

Machine learning (ML) techniques have increasingly been applied to model Urban heat islands (UHI) and land surface temperature (LST) dynamics, and other complex urban environmental phenomena. ML algorithms capture nonlinear interactions and spatial heterogeneity between environmental and urban factors, but traditional statistical approaches fail to do so. Therefore, algorithms used in the study, such as Random Forest, Support Vector Regression (SVR), and Convolutional Neural Networks (CNNs), have the ability to predict LST patterns and identify urban hot spots, and geospatial predictors derived from remote sensing and GIS were incorporated (Snaiki & Merabtine 2025).

The advantage to ML models is their ability to learn nonlinear relationships and spatial heterogeneity in ways that traditional statistical models can't. In addition, models benefit from using ensemble learning or hyperparameter tuning to increase performance and generalizability (Miniandi et al., 2025).

In Athens, data-driven approaches for urban planning and climate adaptation have benefited from the use of machine learning (ML)-based simulations to evaluate land cover and the possible influence on UHI intensity (Spyrou et al., 2024; Georgakis & Santamouris, 2020).

The literature suggests that machine learning can perform better at capturing nonlinear relationships than traditional statistics, although much of the work suffers from “small-n” problems. Convolutional Neural Networks (CNNs) are implemented on a limited number of datasets, i.e. 53 neighborhoods, and are likely to overfit or generalize poorly. This is why more robust ensemble methods, such as Random Forest, are used in this study to determine the most reliable scale for neighborhood analysis.

2.6 Research Gaps and Motivation

There are several studies related to the modeling of urban heat island (UHI) and land surface temperature (LST) but there are still several limitations, especially in Mediterranean urban environments (Santamouris, 2015; Founda & Santamouris, 2017; Roukounakis et al., 2023). Other studies are based on traditional machine learning approaches (e.g. Random Forest) and regression models, however, studies with applications of deep learning techniques are limited especially in areas with distinct climatic and urban characteristics (Breiman, 2001; Hoang & Nguyen, 2025; Snaiki & Merabtine, 2025). In addition, NDVI and NDBI indices effectively represent vegetation, built-up area in cities and can describe land cover but are unable to effectively represent the effects of spatial configuration and geometric complexity in urban environments. Thus, there seems to be a limitation in the fuller understanding of how the complex manifestations of urbanity affect thermal dynamics (McGarigal et al., 2015).

That is, cities are often treated as two-dimensional systems and topographic variables such as altitude and slope are neglected. Athens is a city that has particular variability in its terrain and is affected by air flow, surface exposure to the sun and by extension the distribution of heat (Cetin, 2021; Roukounakis et al., 2023). Methodologically, the study applies a unified and analytical approach, that is, it develops integrated frameworks that combine remote sensing, spatial analysis of GIS and machine learning to evaluate heat in the urban environment of Athens.

Additionally, there is a gap in comparative analysis between models, Convolutional Neural Networks (CNN) as deep learning methods have been adopted, and are often applied but, usually with insufficient evaluation compared to simpler, interpretable models, because e.g. they are applied to small sample sizes with possible overfitting (Hoang & Nguyen, 2025; Breiman, 2001; Chen & Guestrin, 2016). Therefore, there is a need for studies with comparisons and different modeling strategies to achieve better application to issues of urban climate.

The present study addresses such gaps because it is based on a combination of GIS, remote sensing data, landscape measurements and topographic variables to analyze and predict spatial patterns of surface heat in Athens. Incorporating NDVI and NDBI measurements and modulation (e.g., FRAC, LSI, ED), comparisons of multiple modeling approaches were made, and the study provides a more comprehensive and spatially explicit understanding of urban heat dynamics. It includes evidence for urban planning for the upcoming climate change in Mediterranean cities (McGarigal et al., 2015; Hoang & Nguyen, 2025).

3.Methodology

3.1 Overview, Model Evaluation and Workflow Summary

Various statistical measures were used to evaluate the model performance to find the agreement between observed and predicted Land Surface Temperature (LST) values. The coefficient of determination (R^2) was used to measure the percentage of the variation in LST explained by the models, indicating the overall goodness of fit between predicted and observed values (McCarty et al., 2021). Also, by calculating the Mean Absolute Error (MAE) it is possible to quantify the average prediction error in degrees Celsius, having an interpretable measure of the model accuracy (Li et al., 2022). Finally, the Mean Square Error (MSE) was also calculated, giving as a result the magnitude of the prediction errors and to calculate the largest deviations between predicted and observed values (Hodson, 2022).

The interpretation of the influence of environmental predictors was made by analyzing the importance rankings of variables derived from models based on large green areas, and identifying the most important variables that help predict LST. Spatial validation maps were also created to visually compare observed and predicted LST patterns across neighborhoods, and along with numerical evaluation metrics, the spatial consistency of the model predictions was assessed. (Breiman, 2001; Chen & Guestrin, 2016).

The overall methodological workflow of the study can be summarized as follows: The methodological workflow began with data acquisition and preprocessing of satellite imagery and ancillary datasets. Remote-sensing indices (NDVI, NDBI) and land-cover layers were then computed, followed by the calculation of landscape metrics that described urban spatial structure. These environmental variables were integrated with LST data to build neighborhood-level machine learning models (Random Forest, SVR, XGBoost, Decision Trees) and pixel-level CNN models for high-resolution prediction. Finally, model performance was evaluated and spatial patterns of urban heat were mapped across the study area.

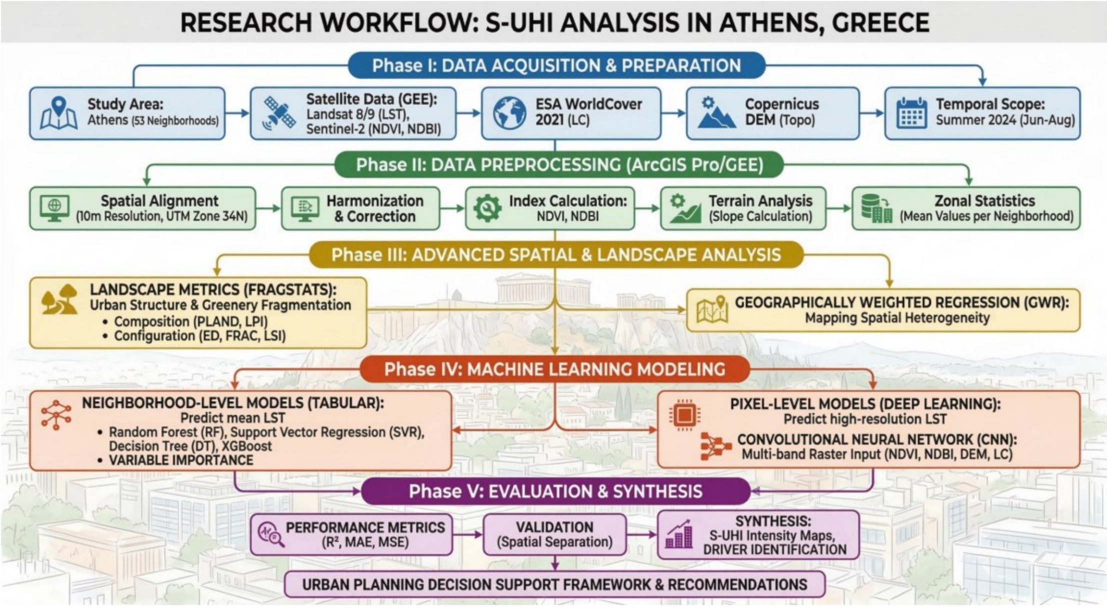

Figure 1 Workflow of thesis

3.2 Study Area

The study area includes the central region of Athens, a city with high density of population and a very heat-stressed city. Previous studies highlight Athens as a UHI hotspot due to its dense urban fabric, limited vegetation, and complex terrain (Zoulia et al., 2009; Spyrou et al., 2024).

Neighborhood boundaries (geitonies.shp) were used as spatial analysis units to capture intra-urban temperature variations, as suggested in earlier UHI research (Roukoukanis et al., 2023).

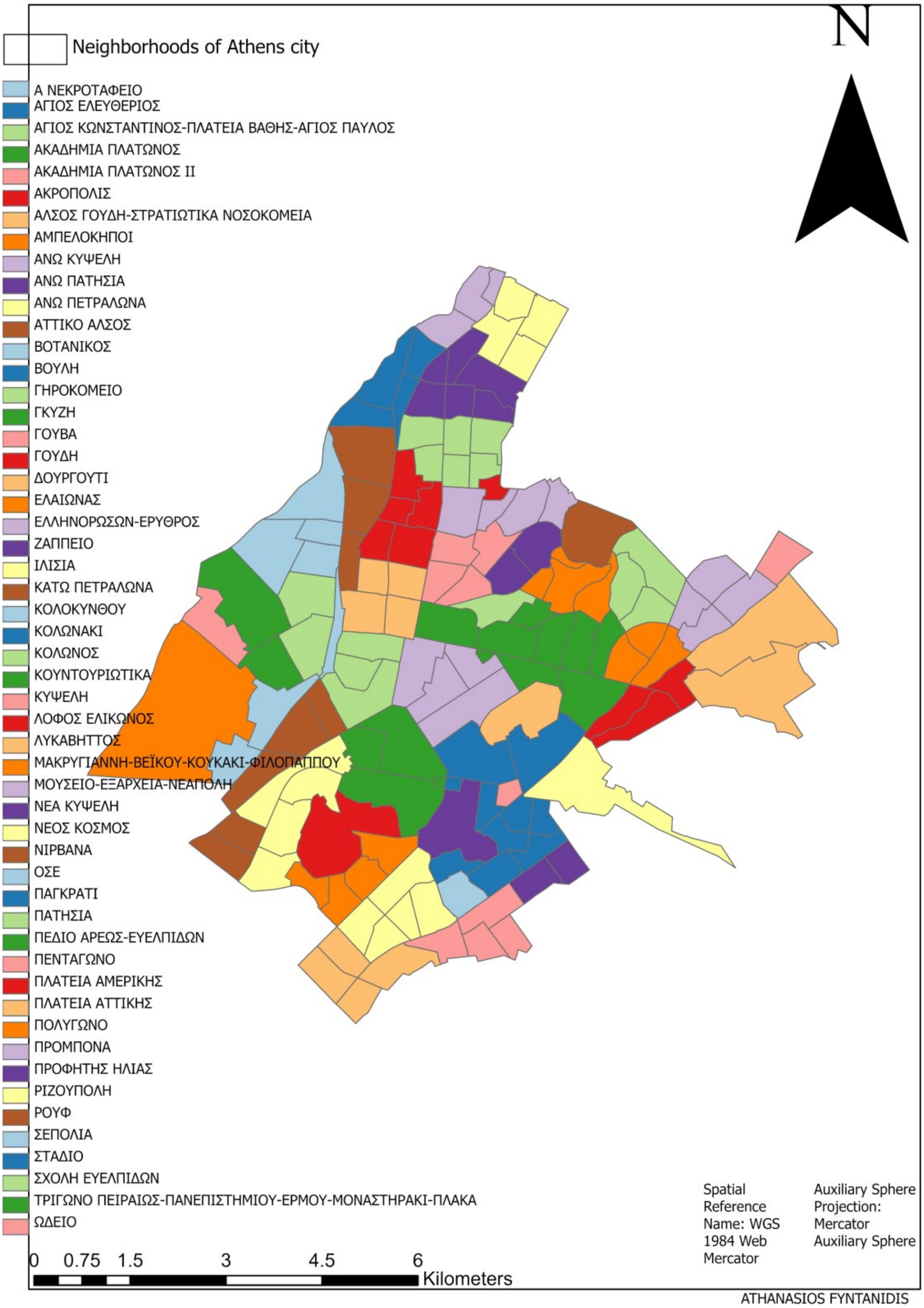

Figure 2 Study Area with the names of neighborhoods.

3.3 Data Sources

Land Surface Temperature (LST): Landsat satellite images provide land surface temperature data and provide thermal infrared observations suitable for surface temperature retrieval. The Landsat 8 thermal zones (originally 100 m, resampled to 30 m) and the Copernicus GLO-30 DEM (i.e. 30 m) were integrated with Sentinel-2 markers at 10 m resolution. Also, to ensure accuracy in all variables, all 30 m datasets after resampling were scaled to a common 10 m spatial grid using bilinear interpolation in Google Earth Engine (GEE). The 10 m resolution was used as the final resolution scale for the needs of this study, i.e. for machine learning modeling as well as spatial mapping. As is well known, Sentinel-2 images do not contain thermal zones but were only used to calculate auxiliary indices such as NDVI and NDBI, which supported spatial upscaling and environmental analysis.

The spatial grid used was a 10 m spatial grid, allowing the integration of Sentinel-2 derived indices, land cover information and topographic variables. This spatial analysis was used both for machine learning modeling and for the production of spatial maps of surface urban temperature patterns across Athens ((NASA, n.d.).

LST data were extracted for the summer months of June, July and August 2024, which represent the period of highest heat stress in the region. These months were chosen because they provided satellite observations with no or low cloud cover and are representative of peak summer heat conditions in Athens, which are usually associated with intense urban heat island effects (Founda & Santamouris, 2017; Keramitsoglou et al., 2011).

3.4 Data Preprocessing

All datasets were harmonized to a spatial resolution of 10 m, like the Sentinel-2 images. Since the 100 m resampled Landsat 8 thermal data had a resolution of 30 m, they were finally downscaled to 10 m after using the Sentinel-2 derived predictors for the best result in the high-resolution analysis. Initial data processing was performed in ArcGIS Pro 3.2 and Google Earth Engine (GEE) to spatially match and be compatible with each other; the dataset used in the analysis.

The Sentinel-2 images used in this study were obtained from the Surface Reflectance Level-2A product, which is atmospherically corrected using the Sen2Cor processing algorithm. And for this reason, no additional atmospheric correction was performed before calculating the spectral indices. The vegetation and structured growth indices (NDVI and NDBI) were calculated from these surface reflectance bands.

All raster datasets were cropped to the Area of Interest (AOI) corresponding to the administrative boundaries of Athens. To ensure consistency, all layers were initially processed at 10 m resolution. While EPSG:4326 / WGS 1984 was used for cloud-based processing in GEE, all datasets were subsequently reprojected to ETRS89 / UTM Zone 34N. This metric projection was essential for calculating landscape metrics (e.g., Edge Density and Shape Index), as it preserves accurate area and distance measurements.

The different resolutions of the Copernicus DEM and Landsat LST products had to be harmonized and were resampled from 30 meters to 10 meters using bilinear interpolation to maintain surface continuity. Categorical data, such as ESA WorldCover 2021 (originally 10 meters), were preserved using nearest neighbor interpolation to maintain distinct class boundaries. The land cover classes were simplified to two classes (urban and vegetated) and exported as integer rasters for spatial analysis.

Terrain derivatives were generated from the DEM in Google Earth Engine, where slope values were calculated in degrees to account for topographic influences on solar exposure and local airflow patterns.

For the neighborhood-level machine learning models, the raster datasets were summarized using zonal statistics, producing tabulated datasets containing mean values of NDVI, NDBI, DEM, slope, and landscape measurements for each neighborhood unit. For the pixel-level CNN models, the raster layers representing NDVI, NDBI, DEM, and land cover were combined via zonal stacking to create composite multizonal rasters. These composites were then exported as 256 × 256 pixel tiles, which served as input patches for the CNN model implemented in Google Colab.

Finally, visual checks were performed against high-resolution base maps, while summary statistics were used to confirm that the elevation, slope, and spectral index values fall within the expected ranges for the study area.

3.5 Remote Sensing Indices and Landscape Metrics

Combined remote sensing data and land cover information to represent vegetation, built-up area. Two widely used spectral indices were calculated from Sentinel-2 images to characterize vegetation and built-up areas.

The Normalized Difference Vegetation Index (NDVI) was calculated as: NDVI = (NIR − Red) / (NIR + Red). NDVI provides an indicator of vegetation density and health, with higher values corresponding to areas with greater vegetation cover (Cetin 2015). It is known that vegetation is an important factor in mitigating urban heat due to shading and evapotranspiration, which can reduce surface temperatures.

The Normalized Difference Vegetation Index (NDBI) was calculated as: NDBI = (SWIR − NIR) / (SWIR + NIR). The NDBI highlights built-up surfaces and their impervious materials, which are commonly found in urban areas (Zha et al., 2003). Higher NDBI values generally correspond to areas with dense built-up infrastructure, which tends to retain heat and contribute to increased surface temperatures.

These indices have been used extensively in many studies with results investigating the relationships between vegetation cover, urban development, and urban heat island patterns (Zoulia et al., 2009; Georgakis & Santamouris, 2020).

In addition to spectral indices, some quantification of the spatial configuration of built and green areas was also required, for which landscape metrics were calculated. The latter describe the composition and spatial structure of land cover segments and are reportedly widely used in landscape ecology and urban environment studies (McGarigal et al., 2012). The following metrics were selected for this study:

• PLAND (Landscape Percent): Represents the percentage of the landscape occupied by a specific land cover category.

• LPI (Largest Patch Index): Indicates the dominance of the largest patch within the landscape.

• ED (Edge Density): Measures the total length of the edges of the segments per unit area, representing the fragmentation of the landscape.

• FRAC (Fractal Dimension Index): Describes the geometric complexity of the shapes of the segments.

• LSI (Landscape Shape Index): Quantifies the overall shape complexity of the segments within the landscape.

These metrics were calculated at the neighborhood scale for both built and green land cover categories, in order to study and present the spatial heterogeneity of urban form. By integrating spectral indices with landscape metrics, the analysis takes into account not only the presence of vegetation or built surfaces, but also their spatial arrangement within the urban environment, which has been shown to influence urban thermal patterns (Zoulia et al., 2009; Chen et al., 2014).

The resulting variables were then used as predictor variables in machine learning models to analyze and predict spatial land surface temperature patterns across Athens.

3.6 Machine Learning Models

The following modeling approaches were applied to analyze and predict spatial patterns of urban heat in Athens, in the Google Colab environment.

(a) Neighborhood-level models

Tabular datasets summarizing environmental variables at the neighborhood scale were used to train several machine learning models. The predictor variables included NDVI, NDBI, DEM, land-cover fractions, and landscape metrics calculated for each neighborhood unit. The following algorithms were applied:

• Decision Trees (DT): Interpretable rule-based models capable of identifying hierarchical relationships between environmental predictors and land surface temperature.

• Random Forest (RF): An ensemble learning method that improves prediction stability and allows assessment of variable importance (Breiman, 2001).

• Support Vector Regression (SVR): A kernel-based method suitable for modeling nonlinear relationships between environmental variables and temperature patterns (Smola & Schölkopf, 2004; Vapnik, 1995).

• XGBoost: A gradient boosting algorithm designed to improve predictive accuracy and handle complex interactions among predictors.

These models were trained using neighborhood-level datasets derived from zonal statistics, enabling interpretable relationships between urban environmental characteristics and LST patterns (Breiman, 2001; Chen & Guestrin, 2016; Smola & Schölkopf, 2004).

(b) Pixel-level models (Convolutional Neural Networks)

To capture fine-scale spatial patterns of urban heat, Convolutional Neural Networks (CNNs) were applied at the pixel level. CNN models were implemented in Google Colab using TensorFlow/Keras.

The model inputs consisted of multi-band raster patches including NDVI, NDBI, DEM, and land-cover layers, while the output variable corresponded to pixel-level LST values. Raster datasets were divided into 256 × 256 pixel tiles that served as input samples for the CNN model (Hoang & Nguyen, 2025).

To avoid data leakage, training and testing datasets were separated based on spatial partitions, ensuring that tiles originating from the same neighborhoods or overlapping spatial regions were not included in both training and testing datasets. This spatial separation helps ensure that model evaluation reflects true predictive performance rather than spatial autocorrelation effects.

The CNN architecture consisted of sequential convolutional layers with pooling operations followed by regression output layers designed to predict LST values. Model performance was evaluated using Mean Absolute Error (MAE) as the primary accuracy metric.

Regarding the outlier handling in LST data, some extreme LST values were observed in the satellite-derived datasets (e.g., values exceeding 55–60 °C or below 20 °C during summer months). Such outliers can occur due to residual atmospheric effects, sensor noise, mixed pixels, or variations in surface emissivity in thermal satellite measurements (Li et al., 2013; Yu et al., 2020). In the figures of LST it is seen that the maximum temperatures exceed 70°C because this is characteristic of the radiation temperature of impervious urban surfaces (such as asphalt or tarmac) during the summer day due to intense solar exposure, which can certainly exceed considerably the ambient air temperature recorded by local weather stations.

In order to preserve the full spectral and spatial variability of the dataset, these values were retained during model training. However, interpretation of urban thermal patterns focused primarily on the realistic temperature range for Athens during summer conditions (approximately 30–50 °C), as reported in previous studies of urban climate in the region (Founda & Santamouris, 2017).

3.7 Land Surface Temperature Data Extraction Using Google Earth Engine

The Google Earth Engine (GEE) platform, which provides cloud access to large satellite data sets and geospatial processing tools, collected the Land Surface Temperature (LST) data for the summer period of 2024. Satellite images from the Landsat mission were used to extract LST values for the study area (Founda & Santamouris, 2017).

In GEE, the boundaries of the area of interest (AOI), which correspond to the administrative boundaries of Athens, were defined and used to clip all satellite images. Representative summer dates of the months of June, July and August of 2024 were selected to extract the LST datasets, in order to identify seasonal variations in surface temperature during the summer period where high temperatures are detected.

Spectral indices, including Normalized Difference Vegetation Index (NDVI), Normalized Difference Structured Index (NDBI), and Normalized Difference Water Index (NDWI), were also calculated within GEE using standard zone ratio formulas. This represented vegetation cover, structured surface intensity, and surface moisture conditions, respectively. Scatter plots and regression analyses were generated in GEE to explore the relationships between LST and the spectral indices (Zha et al., 2003). The resulting datasets were exported for further spatial analysis and visualization in ArcGIS Pro.

3.8 Core Landscape Metrics for Urban Analysis

Landscape metrics were used to quantify the composition and spatial configuration of built-up and vegetated areas at the neighborhood scale. The study focused on a core set of widely used indicators that capture area share, fragmentation, patch dominance, and shape complexity:

Table 1 Landscape Metrics for Urban Analysis

Metric	Formula (plain text)	Description	Units	Notes
LSI (Landscape Shape Index)	LSI = E/(2*sqrt(pi*A))	Patch shape complexity vs a circle, higher = more irregular/fragmented.	Unitless	E: total edge length, A: area. Per class/zone.
ED (Edge Density)	ED = E / A	Total edge length per unit area, higher = more fragmented landscape.	m/ha or m/km²	E: edge length, A: landscape area.
LPI (Largest Patch Index)	LPI = 100*(Amax/Atotal)	Percent of landscape occupied by the largest patch of a class.	%	0–100, by class (built-up, green).

PD (Patch Density)	PD = (N/A)* 10,000	Patches per 100 ha, higher = more fragmented.	patches/100 ha	N: number of patches, A: area (ha).
PLAND (Class % Area)	PLAND = 100* (Aclass/Atotal)	Percent of landscape covered by the class.	%	Use for urban vs green share.
FRAC (Fractal Dimension Index)	FRAC = [2*ln(0.25*P)] / ln(A)	Patch shape complexity	Unitless	Per patch, P: perimeter, A: area.

These metrics were computed separately for urban and vegetated classes for each of the 53 neighborhoods using FRAGSTATS, based on a simplified two-class land-cover map distinguishing urban from green areas. Within this framework, PLAND and LPI quantify how dominant built-up or green areas are in each neighborhood, while ED, PD, LSI and FRAC describe the degree of fragmentation and geometric complexity of the corresponding patches, thereby supporting subsequent analysis of how the spatial configuration of urban and vegetated surfaces relates to observed LST patterns.

4 Results

4.1 Spatial Context and Explanatory Variables.

Like many Mediterranean cities, Athens is an urban center with high density elements in structure and is dominated by impervious surfaces, and in contrast, green areas are found in areas around the city but also in small areas. Figure 3 shows the land cover distribution of Athens, which is the basic area for the analysis of spatial composition in this study. These surface data complement the contrasts in the topographic context of the city and these range from about 9 meters in the coastal lowlands to almost 330 meters in the surrounding hilly and mountainous areas. And it has been reported that elevation differences affect local microclimates, almost directly, due to topographic shading and the exchange of surface-atmosphere energy.

From the Sentinel-2 images, spectral indicators are derived to further define the environmental analysis of the city. The Normalized Difference Building Index (NDBI) shows the spatial intensity of high density of impervious materials, and the homogeneous urbanization in the central areas of the city is visible, the values reaching up to 0.95. On the contrary, the areas around the center appear with lower or even negative NDBI values, showing the influence of the various land uses.

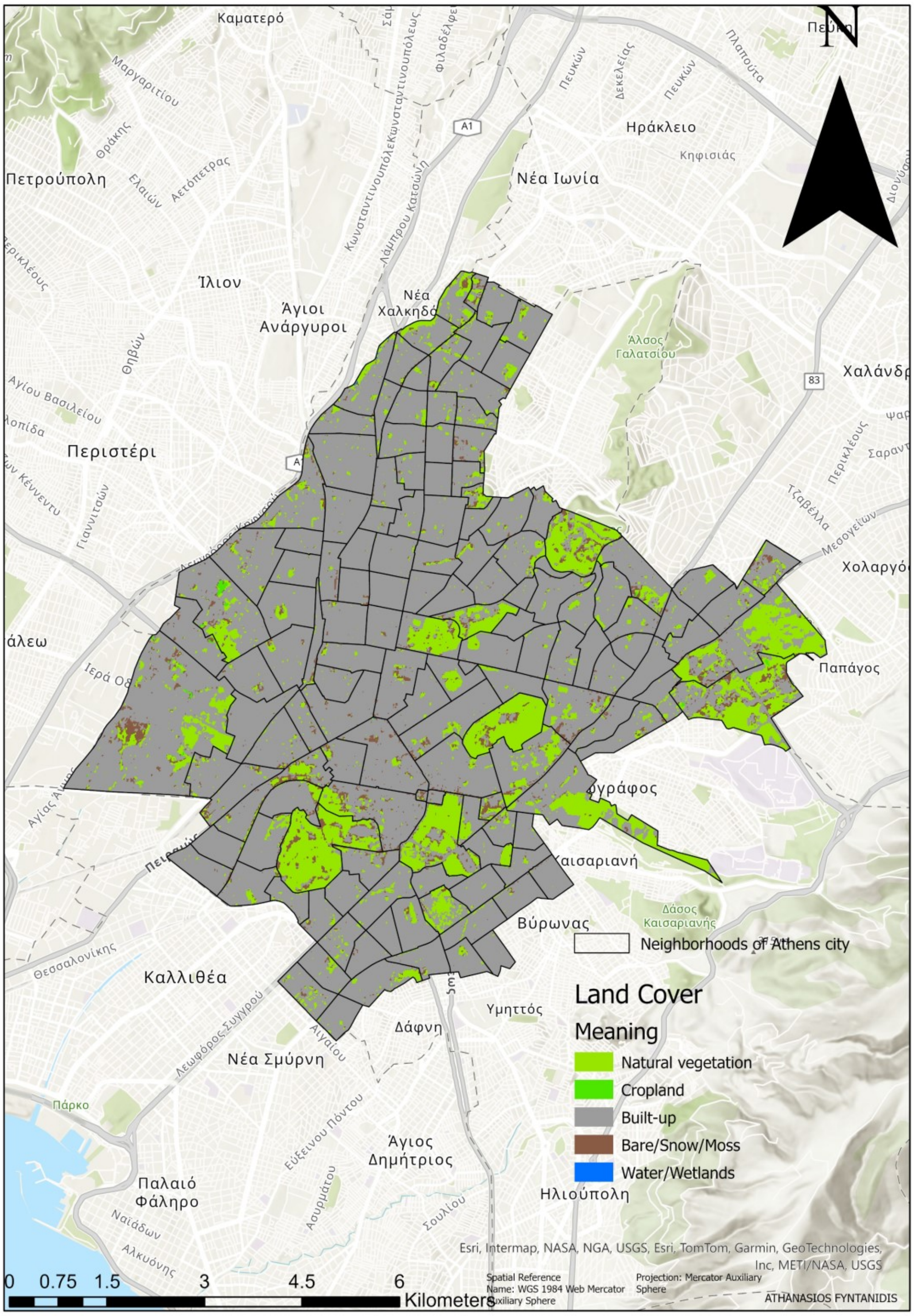

Figure 3 Land Cover map of Athens city (Source: ESA WorldCover 2021).[1]

[1] The land cover classification of Athens was obtained from the ESA WorldCover 2021 product, which is derived from a fusion of Sentinel-1 and Sentinel-2 imagery at a 10 m spatial resolution, providing essential spatial information on built-up areas, vegetation, cropland, and water bodies. As shown in Figure 3, the urban core is dominated by impervious surfaces, while patches of natural vegetation and cropland are located primarily in peripheral neighborhoods. This classification provides a useful representation of the spatial composition of the urban environment and supports the interpretation of landscape metrics used in the analysis. (Zha, Gao, & Ni, 2003; Guha et al., 2018).

The spatial configuration of built-up and vegetated areas was measured using landscape metrics including PLAND (percentage of landscape), Edge Density (ED), and Largest Patch Index (LPI). These landscape metrics can identify how much land covers vary by type and how they are spatially arranged. For example, a neighborhood with a large single continuous built-up area may have a high amount of impervious surface area but will likely have a lower ED, whereas an area with a greater number of fragmented green and built areas may have higher EDs.

Examining land cover types in relation to how different types of land are arranged spatially helps to better understand how the spatial arrangement of urban surfaces and vegetation affects the urban thermal environment. Past studies have demonstrated that the amount of urban greenery and how urban greenery is spatially arranged affect surface temperature patterns in Mediterranean cities, particularly in cities such as Athens. (Founda & Santamouris, 2017).

4.2 Landscape Metrics

The composition and spatial configuration of the urban field of Athens is quantified by landscape measurements, so at the neighborhood level there is the structural basis for the study of this thermal variation. As summarized in Table 1, landscape measurements describe the complexity, fragmentation and dominance of land cover areas.

A gradient is seen, going from the compact urban core to the fragmented outskirts, in the spatial configuration. Centrally, the shapes are characterized by geometrically uniform urban building blocks with low Shape Indices (LSI < 2.0) and low Fractal Dimension Indices (FRAC < 1.1), demonstrating the true image of the center, i.e. with high density development in the structural element. For this reason, the percentage of built-up area (PLAND) often exceeds 85%, leaving little space for open or green areas.

In contrast, around the center, surfaces with a high fragmentation value are presented, but also Edge Density (ED) values in the outskirts can exceed 400 m/ha, indicating scattered structures interspersed with open spaces (Figure 4). Which is further confirmed by the higher FRAC values (> 1.2), which indicates the irregular spread on the urban fringes. In addition, the urban cores do not have large contiguous green areas (LPI < 40%), the peripheral zones e.g. near the Hymettus forests maintain green cores that help to cool the areas. Complete maps for all landscape measurements are provided in Appendix F.

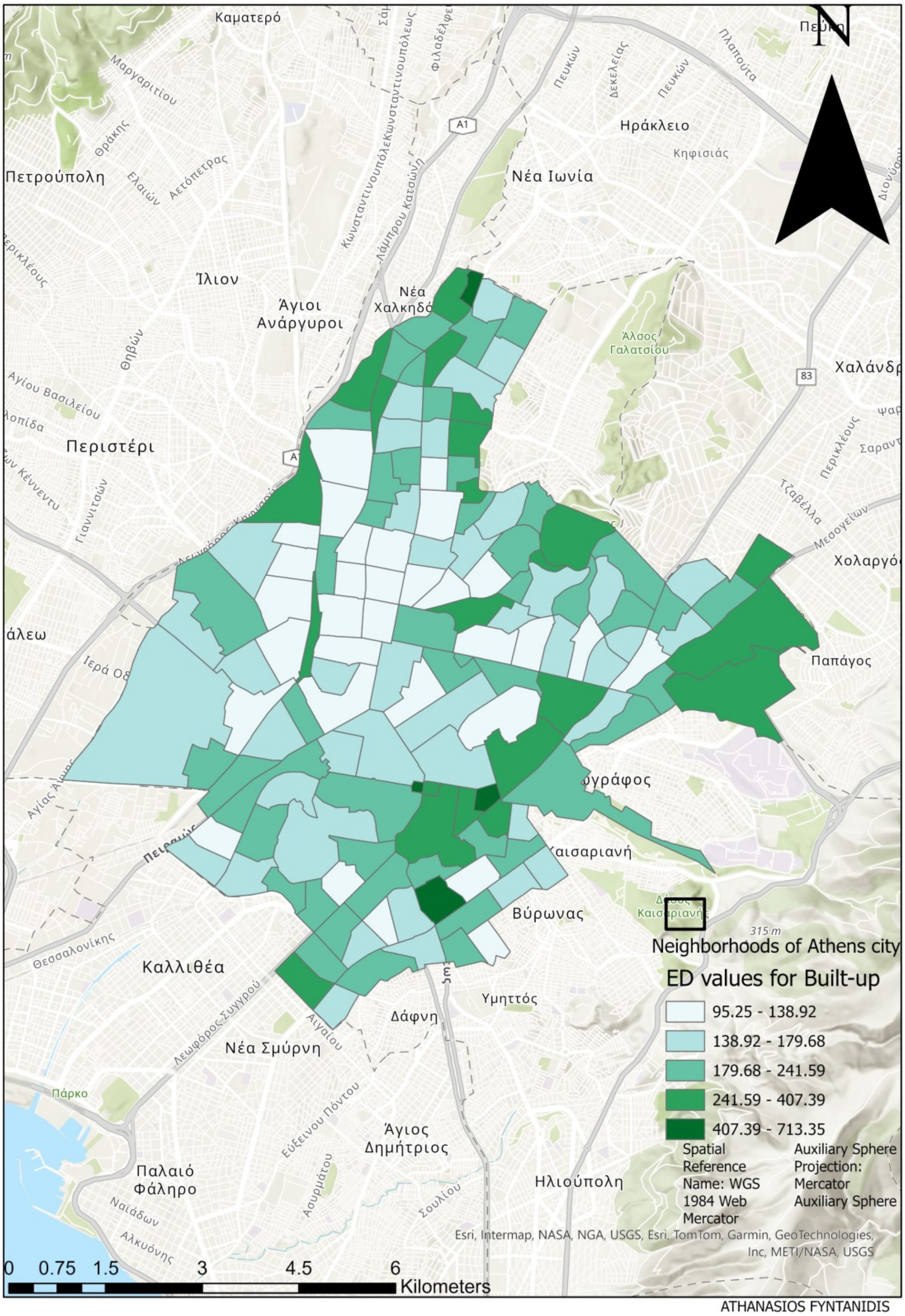

Figure 4 ED map for Built-up in Athens city.[2]

2 The Edge Density (ED) in built-up areas of Athens varies and ranging from about 95.2 to 713.3 meters per hectare. This variation indicates a *diverse urban structure* across the city. Central districts typically have low ED values, approximately 140 m/ha, due to dense urban blocks that limit the perimeter exposure for each area. Others neighborhoods usually show intermediate ED values between 140 and 240 m/ha, which suggests a *mix of land uses and moderate fragmentation*. Higher ED values, exceeding 400 m/ha, are found mainly in the outskirts of the city, especially in newly developed or semi-urban areas where built structures are more scattered among open or green

4.3 Spatial Patterns of LST

The summer of 2024 was a very hot summer in Athens and heat accumulation intensified throughout the city, with the highest temperatures occurring in July. Although the patterns for June and August are presented in Appendix F, July is the month that appears to have the highest Urban Heat Island (UHI) intensity. On 13 July 2024, the satellite-derived Land Surface Temperature (LST) reached a maximum of 86.23°C on impervious surfaces (Figure 5). It should be noted that these extreme values are characteristic of the skin radiation temperature of low albedo urban materials - such as asphalt and concrete - and this is because these materials absorb and retain intense solar radiation during heatwave conditions. The maps show the extent of hot spots almost throughout the central and western study area, where the high density of buildings and the limited green area contributed to the phenomenon of thermal retention.

The highest temperatures occur in a compact built-up area and large roads and, in contrast, the lowest temperatures occur in green surfaces and elevated ground, demonstrating how important the role of vegetation and topography is in regulating the microclimate. Spatially, this distribution shows where heat is stored and that it is a typical phenomenon for cities like Athens during a very hot summer.

spaces. This distribution represents a change from dense urban centers to more fragmented suburban regions, showing how urban growth and discontinuous development create distinct edge interfaces—a trend often seen in Mediterranean cities. (Bajocco et al., 2012).

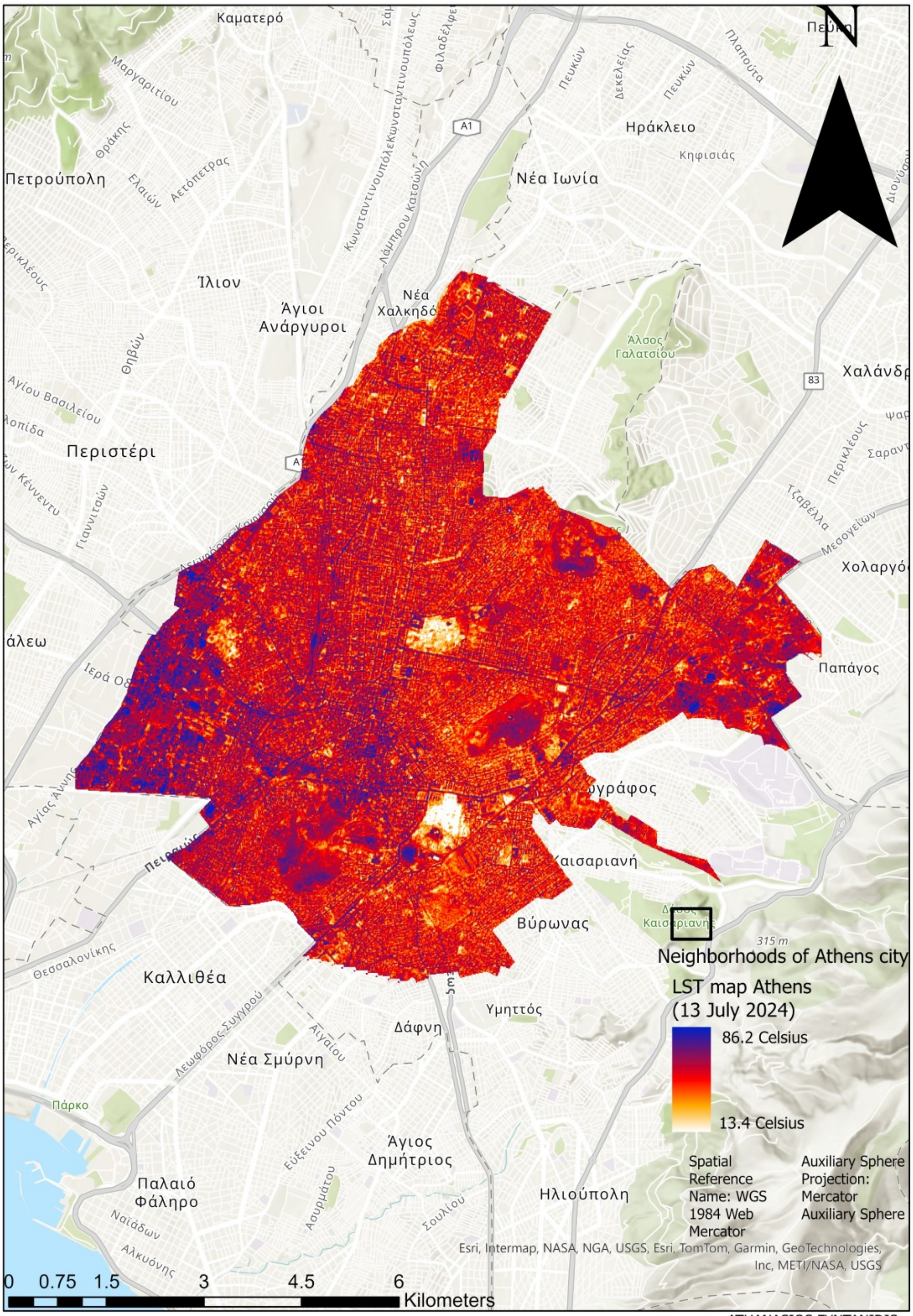

ATHANASIOS FYNTANIDIS

Figure 5 LST map in Athens's city (13 July 2024)[3]

[3] The LST map for 13 July 2024 shows an increase of surface heating, with temperatures reaching up to 86.23 °C, indicating peak midsummer conditions. The values of temperature are high but are aligned with the known behavior of impervious surfaces due to low reflectivity in urban areas during heat waves and it appears that surface-air temperature gradients can be wide. It is clear that hotspots become more extensive across the central and southern Athens districts, with high-density building coverage and slight vegetation contribute to extreme heat preservation. Some of the warmest clusters appear around industrial areas, major road corridors, and compact residential grids.

4.4 Relationships between LST and Predictors

The relationship between Land Surface Temperature (LST) and urban environmental factors was analyzed both through global correlations in Google Earth Engine (GEE) and local spatial regressions using Geographically Weighted Regression (GWR). The GEE analysis revealed that spectral indices adequately explain the phenomenon as it intensified as the summer progressed. A weak relationship between LST and the examined indices is shown during the month of June. However, from July onwards, the relationship with the Normalized Difference Built Area Index (NDBI) became stronger (R^2 = 0.14), indicating that built surfaces are the main contributor to surface heat when summer temperatures rise.

In contrast, the Normalized Difference Water Index (NDWI) showed a weak, negative correlation throughout the summer, marginally indicating that it may have a cooling effect due to surface moisture. The spatial heterogeneity of the above relationships in the study area is also seen with the GWR modeling. Thus, it appears that the NDBI coefficients have a strong positive connection with LST in almost all neighborhoods, proving once again that the high intensity of the built-up area is the most serious local factor of heat accumulation. The local spatial structure also played a critical role. Additionally, the positive coefficients for the Landscape Shape Index (LSI) and Edge Density (ED) in the city center indicate the irregular and fragmented built forms as other factors that intensify local heating (Figure 6).

Finally, in contrast to the built environment factors that led to warming, topographic and vegetation variables had the opposite effect and provided local cooling. Negative GWR coefficients are present for elevation (DEM) and NDVI, mainly in the western and southern areas near the foothills of Hymettus, and thus a temperature drop is caused by elevation and improved airflow resulting in a reduction of the Urban Heat Island (UHI) effect. Detailed GWR coefficient maps for these secondary topographic and vegetation factors are provided in Appendix F. The overall coefficient of determination (R^2) and the Akaike Information Criterion (AIC), which were used to measure the explanatory power of the model and the quality by balancing goodness of fit and model complexity, respectively, show how spatially varying relationships improve model performance compared to global regression approaches.

This pattern was further examined using Geographically Weighted Regression (GWR). The GWR model was applied at the neighborhood level, with mean LST as the dependent variable and neighborhood-level environmental predictors, including NDBI, NDVI, DEM, slope, ED, and LSI, as explanatory variables. The resulting local coefficient maps were used to evaluate how the strength and

---

Cooler temperatures persist only in parks, peri-urban green zones, and elevated terrain, demonstrating the critical role of vegetation and topography in moderating heat. The expanded extent of high-temperature zones compared to June reflects cumulative heat storage typical of Mediterranean summers.

direction of these relationships varied across Athens. Where positive local coefficients were observed for ED and LSI, particularly in central urban areas, the results suggest that more fragmented and irregular built-up structures were associated with higher LST. This indicates that the relationship between urban form and surface heat is spatially heterogeneous rather than uniform across the study area.

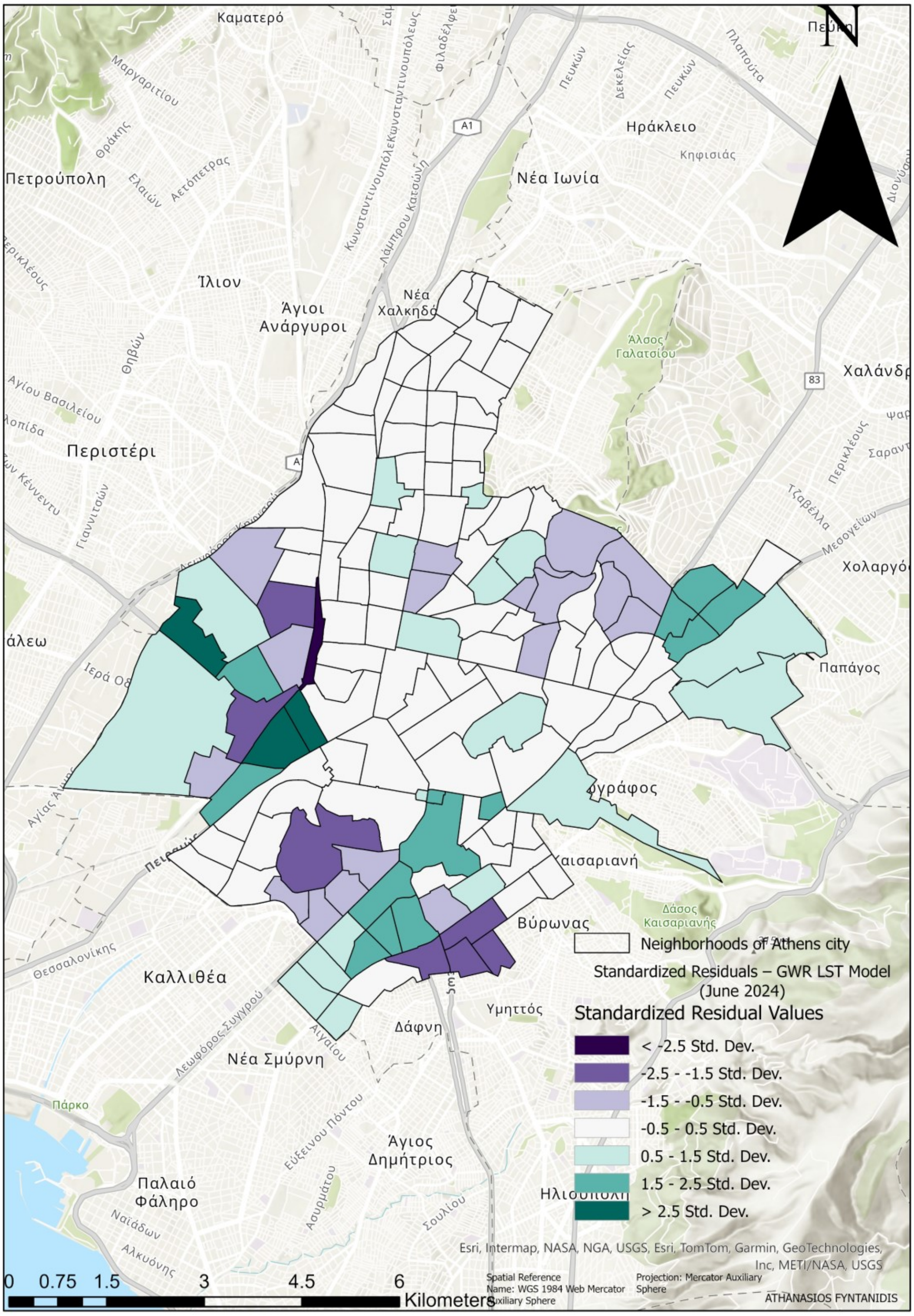

Figure 6 GWR map (LST model)

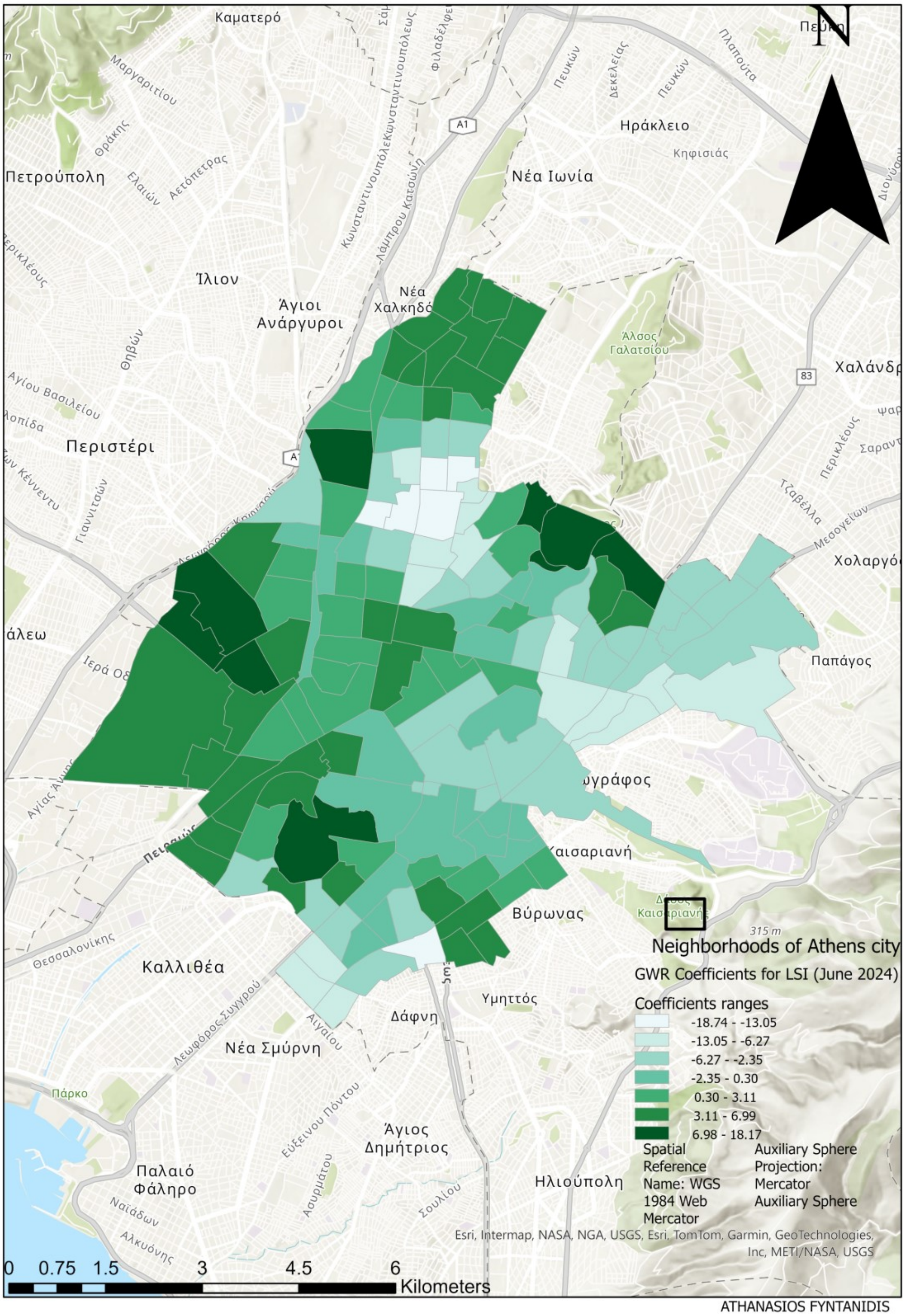

Figure 7 GWR map (LSI model)

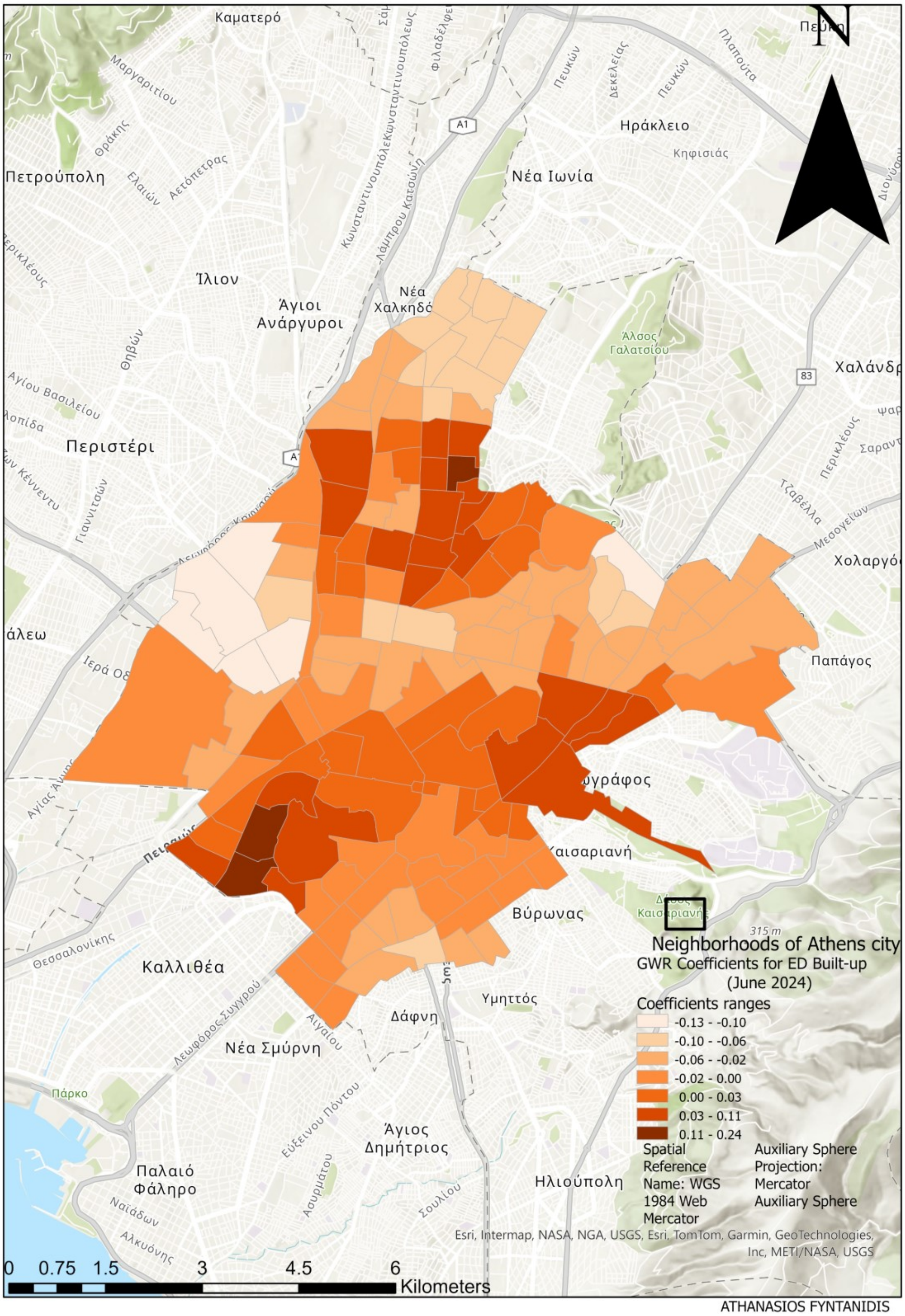

Figure 8 GWR map (ED model)

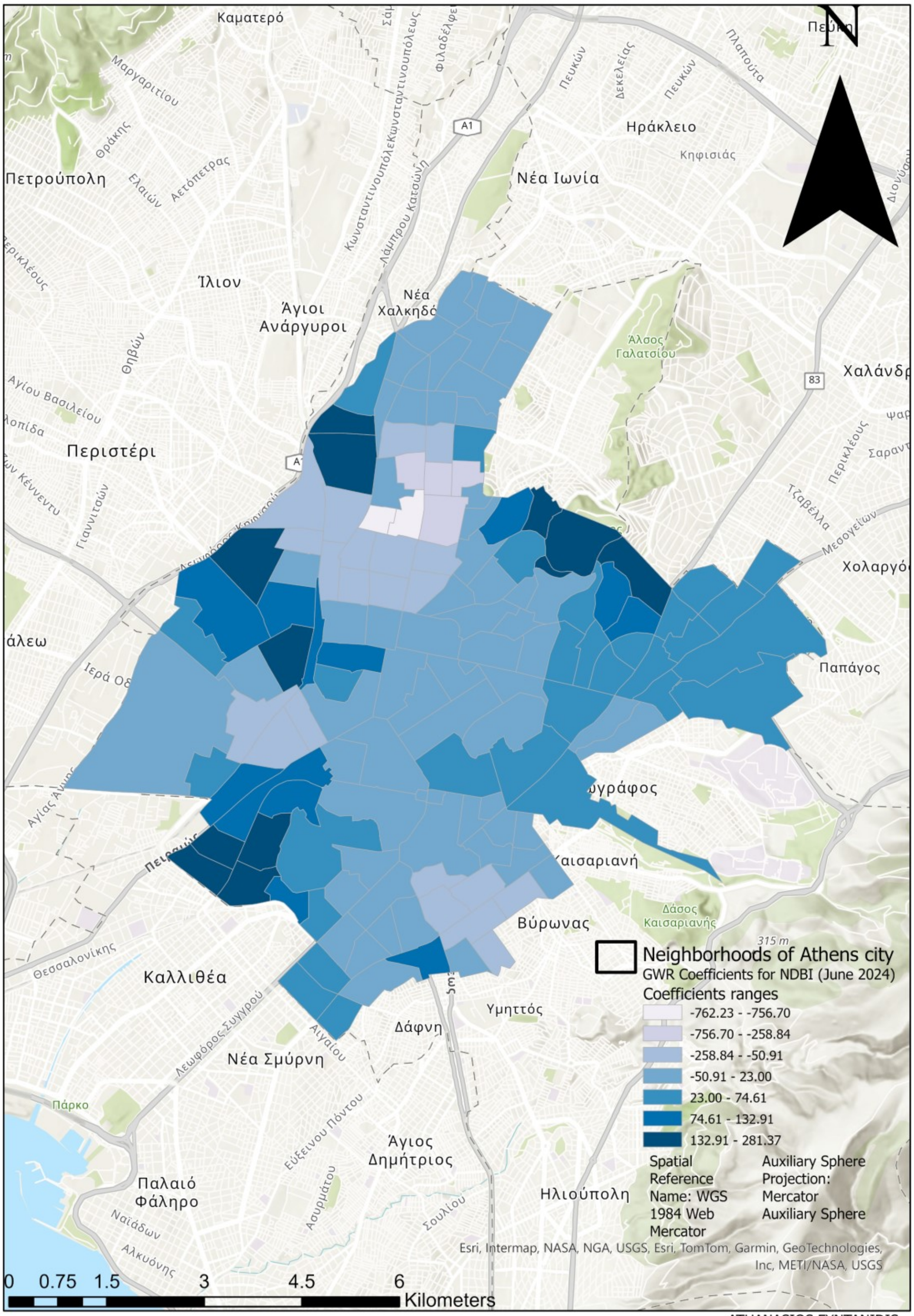

ATHANASIOS FYNTANIDIS

Figure 9 GWR map (NDBI model)

4.5 Machine Learning Results

In this study, the predictive performance of machine learning models was evaluated at two spatial scales, at the neighborhood level (administrative units) and at the pixel level (10 m resolution). The results show that tree-based ensemble methods prove to be the most reliable for predicting LST at the neighborhood scale. The predictive performance of the machine learning models was evaluated using independent test datasets (30% separation) with temperature values scaled to degrees Celsius to ensure natural interpretability. Throughout the study period (summer 2024), the models varied in their ability to capture the nonlinear relationships between environmental predictors and land surface temperature (LST), but demonstrated consistent but varied predictive abilities.

4.5.1 Neighborhood-Level Model Comparison

At the neighborhood level, Random Forest (RF) consistently had the highest predictive accuracy in the summer months of the study, with a maximum R^2 value of 0.5153 in August. It also showed the best balance between good fit and low prediction error (RMSE of approximately 1.75°C). In contrast, Decision Trees (DT), although they identified hierarchical relationships and critical thresholds for NDBI and NDVI, were not as consistent as RF. On the contrary, Support Vector Regression (SVR), which is a kernel-based model, and XGBoost, which is a gradient boosting model, showed less consistency. Due to the small sample size (n=53 neighborhoods), the above models showed significant sensitivity, resulting in lower R^2 values and therefore somewhat higher error rates as the summer months passed. It was confirmed that building density (NDBI) was the dominant factor for predicting LST, from the analysis of variable importance (RF models), followed by elevation (DEM) and vegetation (NDVI).

Table 2 Model performance for June (neighborhood level; test set). Models are evaluated using coefficient of determination (R^2), root mean squared error (RMSE, °C), and mean absolute error (MAE, °C).

Model	R^2	RMSE (°C)	MAE
Random Forest	0.4849	1.7441	1.3259
SVR	0.3724	1.9252	1.4107
Decision Tree	0.2911	2.0462	1.5472
XGBoost	0.2747	2.0697	1.6635

Table 3 Model performance for July (neighborhood level; test set). Models are evaluated using coefficient of determination (R^2), root mean squared error (RMSE, °C), and mean absolute error (MAE, °C).

Model	R^2	RMSE (°C)	MAE
Random Forest	0.4892	1.7459	1.4145
SVR	0.2181	2.1601	1.3970
Decision Tree	0.5029	1.7224	1.4469
XGBoost	0.1935	1.9882	1.5040

Table 4 Model performance for August (neighborhood level; test set). Models are evaluated using coefficient of determination (R^2), root mean squared error (RMSE, °C), and mean absolute error (MAE, °C).

Model	R^2	RMSE (°C)	MAE
Random Forest	0.5153	1.7472	1.4623
SVR	0.1240	2.3488	1.6965
Decision Tree	0.4003	1.9434	1.5427
XGBoost	0.1576	2.3033	1.7498

4.5.1.1. Decision Tree Interpretation

The Decision Tree model interprets the representation of the relationships between environmental variables and LST. For the months of the study, building intensity combined with minimal vegetation cover is associated with increased average surface temperature values in each neighborhood, while neighborhoods with higher vegetation density and/or higher altitude show lower LST. The Decision Tree model highlights key threshold relationships such as critical NDBI and NDVI values and provides useful information on the structure of thermal factors that are less transparent in ensemble models, but presents lower predictive performance than Random Forest.

4.5.1.2. XGBoost Performance

The XGBoost model captures nonlinear interactions between predictors and LST, but has less consistent performance than Random Forest and Decision Tree. The R^2 values are lower and the RMSE and MAE values are higher, because the number of study neighborhoods is relatively small for a fully optimized slope boosting approach. Even with these limitations, XGBoost is able to confirm the main patterns observed in other models, in particular the dominant role of building intensity (NDBI) and the effect of vegetation (NDVI). Given the modest sample size of the study and the sensitivity of the boosting algorithms to parameter tuning, the XGBoost results should perhaps be considered exploratory rather than definitive, and mainly as a check on the findings from the Random Forest and Decision Tree analyses.

4.5.2 Pixel-Level Spatial Prediction (CNN)

By applying the Convolutional Neural Network (CNN) we have captured fine-scale spatial dependencies that the tabular neighborhood models could not resolve. Realistic spatial maps were successfully produced (represented on Appendix), showing where the warmest urban cores are, distinguishing them from the cooler areas, where vegetation was reported. However, the R^2 values (between 0.11 and 0.19) indicate that its statistical predictive performance remained low. As will be discussed in the next chapter, although deep learning is a powerful tool for identifying hot spots, the current data configuration and sensor noise at the 10 m pixel level limited its predictive accuracy.

Table 4 CNN performance for June, July and August (pixel level; test tiles). Metrics include mean absolute error (MAE, °C), mean squared error (MSE, °C^2), and coefficient of determination (R^2) between observed and predicted LST.

Metric	Value (JUNE)	Value (JULY)	Value (AUGUST)
MAE	3.4846	4.4307	3.8803
MSE	4.5074	5.6039	4.9144
r^2	0.1116	0.1935	0.1585

The use of a 70–30 test split and appropriate preprocessing help to limit overfitting and yielded metrics that better approximate the model's behavior in unseen data. At the same time, the spatial nature of the data and the close neighborhoods are similar, random splits can produce R^2, RMSE, and MAE values that are optimistic. The reported metrics should therefore be interpreted as optimistic upper bounds on predictive performance, and model differences—especially when small—should be treated with caution.

5. Discussion and Recommendations

5.1 Interpretation of Thermal Factors and Seasonal Dynamics

It was shown that for all models, the most important explanatory factor for modeling Land Surface Temperature (LST) is the Normalized Difference Building Index (NDBI), a result consistent with the findings of Zoulia et al. (2009) and Georgakis and Santamouris (2020). The latter have also found that the maximization of heat storage and the limitation of airflow are common phenomena in cities such as Athens and other Mediterranean densely populated cities. However, from this study, a seasonal shift in environmental predictors is seen, challenging the simplest models. The NDVI index is a recognizable cooling factor, but its correlation with LST "disappeared" during the extreme heat of July (with an R^2 value of approximately 0). It is thus suggested that during periods of extreme heat, Mediterranean urban greenery needs water so much that evapotranspiration reaches its limits and does not yield the maximum degree of cooling that is possible. It is said, however, that the NDWI index has the potential to be the most important factor in August ($R^2 = 0.172$), and thus at the end of summer, surface humidity affects the thermal gradients of August.

The Random Forest variable-importance results suggest that built-up intensity, represented by NDBI, was one of the most influential predictors of neighborhood-level LST across the summer months. This is consistent with the interpretation that impervious urban surfaces are strongly associated with surface heat in Athens. However, the thermal response is not explained by built-up intensity alone. Vegetation, represented by NDVI, appears to contribute to local cooling, while topographic variables such as elevation and slope may influence LST through differences in exposure, airflow, and terrain position. Landscape metrics such as LSI and FRAC provide additional information about the spatial configuration and complexity of urban form, although their influence appears secondary compared with the main spectral and topographic predictors. Therefore, surface heat patterns in Athens should be interpreted as the result of interacting built-up, vegetation, landscape-configuration, and topographic factors.

5.2 Comparative Analysis of Models Strategies

The use of machine-learning and spatial regression approaches provided complementary insights, as Geographically Weighted Regression (GWR) quantified local parameter variation, while the machine-learning models achieved higher predictive power and captured nonlinear relationships between predictors and LST.

Random Forest (RF) proved to be the most reliable predictive model for neighborhood-level datasets, with its ensemble-tree logic successfully balancing generalization with robustness and explaining approximately 48–52% of LST variation, while also providing interpretable variable-importance rankings. Support Vector Regression (SVR) demonstrated stable results in June ($R^2 = 0.3724$) but showed sensitivity to data complexity as the summer progressed, with accuracy decreasing in peak-heat months. XGBoost and Decision Trees, although capable of capturing threshold relationships, exhibited greater variability, indicating that gradient boosting is highly sensitive to the small sample size (n = 53) inherent to neighborhood-level administrative data.

Finally, the Convolutional Neural Network (CNN) extended the analysis to the pixel level; although its R^2 was lower on the independent test set (range 0.11–0.19), it remains a critical tool for revealing fine-scale spatial continuity and identifying sub-neighborhood hotspots that tabular models cannot resolve (set of CNN maps is provided in Appendix)

The predictive performance of the machine learning models in this study is lower than previous ones, and this difference is due to the spatial scale of analysis and the structure of the data set. The models were developed at the neighborhood level (n = 53), and environmental variables and LST values were aggregated using zonal statistics. This reduced spatial variability and smoothed out local extremes, so the models did not capture fine-scale thermal patterns.

Furthermore, each neighborhood in Athens is a heterogeneous spatial unit and contains a mixture of built-up areas, vegetation and open spaces. Providing another explanation for the reduced model performance, because a single aggregate value usually does not fully represent complex local conditions.

Therefore, the performance in this study is considered moderate and can be interpreted in the context of the chosen spatial scale and data structure. Finally, beyond the limitations discussed, the spatial approach of the study provides valuable information for urban planning and decision-making processes.

5.3 Synthesis of Quantitative Results

Regarding the analysis of remote sensing data and the use of machine learning models for Athens in the summer of 2024, the intensity of the Urban Heat Island in the city is confirmed, determined by densely built-up areas and spatial configuration. The Normalized Difference Building Index (NDBI) appeared as the most important explanatory factor for modeling Land Surface Temperature (LST) in all models and months. On the other hand, vegetation (NDVI) and topography (DEM), were considered as cooling factors, since they exhibited negative correlation with LST in the city. At the neighborhood level, Random Forest (RF) was reliable, with predictive performance (R^2 approx. 0.51), and at the pixel level, Convolutional Neural Network (CNN) managed to map points with higher temperature within blocks but had low statistical accuracy ($R^2 < 0.20$).

5.4 Technical Discussion of Spatial Patterns

Spatially studying the thermal concentration points of the urban core with high building density (mainly west and center), LST values are observed on impervious surfaces reaching a maximum of 86.23°C on July 13 (explaining the high value above figure 5)). Similar patterns were observed throughout the summer. This was validated through Geographically Weighted Regression (GWR), and the importance of spatial heterogeneity was confirmed, namely the influence of factors such as Edge Density (ED) and Landscape Shape Index (LSI), since they show how fragmented the built forms are.

5.5 Implications for Urban Planning and Policy

Future-oriented urban design in Mediterranean cities can directly build on these findings by translating thermal patterns into targeted planning actions. CNN outputs can guide greening strategies and vegetation corridors, helping planners pinpoint specific urban blocks for tree canopy expansion or green roof installation, especially in congested central neighborhoods with high NDBI and low LPI of greenery. At the same time, landscape metrics support configuration for enhanced cooling: The Fractal Dimension Index (FRAC) translates into a practical recommendation to promote more organic and irregular outlines, meaning higher FRAC values, when designing new green infrastructure instead of adopting simple, rectangular shapes, since increased shape complexity improves air exchange and the cooling efficiency of green spaces.

Moreover, topography-sensitive planning is essential: higher and sloping areas exhibit naturally lower LST, so urban expansion in these zones needs to maintain vegetative buffers to preserve natural air corridors and the altitude-induced cooling documented in the GWR results. Complementary measures include using reflective and permeable materials instead of darker pavements to reduce surface heat, and integrating remote-sensing–derived LST into municipal GIS so cities can continuously monitor urban temperature and implement targeted mitigation policies; overall, the study demonstrates that spatial modelling based on data can support the development of climate-resilient Mediterranean cities.

5.6 Limitations of the Study

A number of methodological and data limitations need to be mentioned: 53 neighborhoods were used for analysis, a relatively small sample that reduces the statistical power of ensemble models (represents a small sample size for complex machine-learning algorithms like XGBoost and CNN, which reduced their overall predictive power (R^2) at the neighborhood scale). LST was estimated from satellite imagery and may deviate from near-surface air temperature. Only summer months (June–August 2024) were examined, seasonality was not complete (it may deviate from the near-surface air temperatures experienced by citizens at ground level). Training of CNN was constrained by computational resources and limited labeled pixels. Anthropogenic heat releases and socio-economic factors were excluded. These limitations do not decrease the validity of analysis but indicate methods for improvements.

5.7 Recommendations for Future Research

Future research could build on this study by expanding the temporal, methodological, and socio-environmental scope of the analysis. A first priority is to extend the modelling framework to multi-year and multi-season datasets in order to capture both annual and interannual variability of the Urban Heat

Island (UHI) and avoid relying on one exceptionally hot summer for inference. A second direction is to combine satellite-derived Land Surface Temperature (LST) with in situ air temperature measurements, enabling better calibration of the models and narrowing the gap between radiative “skin” temperature and conditions experienced by residents. In addition, future work should incorporate social, economic, and demographic indicators to examine environmental justice dimensions of heat exposure, such as whether vulnerable groups are disproportionately concentrated in hotter neighborhoods. Finally, the methodological framework that integrates remote sensing, landscape metrics, topography, and machine learning in this study could be applied to other Mediterranean cities to test its transferability under different urban morphologies and climatic conditions, helping to develop a more general regional understanding of UHI dynamics.

6. References

Alberti, M. (2005). The effects of urban patterns on ecosystem function. *International Regional Science Review, 28*(2), 168–192.

Bajocco, S., De Angelis, A., Perini, L., Ferrara, A., & Salvati, L. (2012). The impact of land use/land cover changes on land degradation dynamics: A Mediterranean case study. *Environmental Management, 49*, 980–989.

Batty, M., & Longley, P. (1994). *Fractal cities: A geometry of form and function*. Academic Press.

Birch, E. L., & Wachter, S. M. (Eds.). (2011). *Growing greener cities: Urban sustainability in the twenty-first century*. University of Pennsylvania Press.

Breiman, L. (2001). Random forests. *Machine Learning, 45*(1), 5–32.

Cetin, M. (2021). Evaluating the effects of terrain and vegetation on urban heat islands using DEM and remote sensing. *Environmental Monitoring and Assessment, 193*(4), 1–14. https://doi.org/10.1007/s10661-021-08961-2

Chen, A., Yao, L., Sun, R., & Chen, L. (2014). How many metrics are required to identify the effects of the landscape pattern on land surface temperature? *Ecological Indicators, 45*, 424–433. https://doi.org/10.1016/j.ecolind.2014.05.002

Chen, T., & Guestrin, C. (2016). XGBoost: A scalable tree boosting system. In *Proceedings of the 22nd ACM SIGKDD International Conference on Knowledge Discovery and Data Mining* (pp. 785–794).

European Environment Agency. (2019). *CORINE Land Cover 2018*. https://land.copernicus.eu/pan-european/corine-land-cover

Forman, R. T. T. (2014). *Urban ecology: Science of cities*. Cambridge University Press.

Founda, D., & Santamouris, M. (2017). Synergies between urban heat island and heat waves in Athens (Greece) during an extremely hot summer (2012). *Scientific Reports, 7*(1), Article 10973. https://doi.org/10.1038/s41598-017-11407-6

Georgakis, C., & Santamouris, M. (2020). Determination of the surface and canopy urban heat island in Athens central zone using advanced monitoring. *Sustainable Cities and Society, 52*, Article 101856.

Gill, S. E., Handley, J. F., Ennos, A. R., & Pauleit, S. (2007). Adapting cities for climate change: The role of the green infrastructure. *Built Environment, 33*(1), 115–133.

Guha, S., Kumar, R., Dutta, B. B., & Bhanja, A. A. (2018). Assessment of surface urban heat islands over Delhi using thermal remote sensing data. *Urban Climate, 24*, 103–120. https://doi.org/10.1016/j.uclim.2017.12.008

Herold, M., Couclelis, H., & Clarke, K. (2005). The role of spatial metrics in the analysis and modeling of urban land use change. *Landscape Ecology, 20*(5), 361–374.

Higgs, G., Fry, R., & Langford, M. (2021). Accessibility to urban green spaces: A comparative GIS-based analysis. *Landscape and Urban Planning, 214*, Article 104186. https://doi.org/10.1016/j.landurbplan.2021.104186

Hoang, N.-D., & Nguyen, Q.-L. (2025). Geospatial analysis and machine learning framework for urban heat island intensity prediction: Natural gradient boosting and deep neural network regressors with multisource remote sensing data. *Sustainability, 17*(10), Article 4287. https://doi.org/10.3390/su17104287

Hodson, T. O. (2022). Root-mean-square error (RMSE) or mean absolute error (MAE): When to use them or not. *Geoscientific Model Development, 15*(14), 5481–5487. https://doi.org/10.5194/gmd-15-5481-2022

Kabisch, N., Strohbach, M., Haase, D., & Kronenberg, J. (2016). Urban green space availability in European cities. *Ecological Indicators, 70*, 586–596.

Keramitsoglou, I., Kiranoudis, C. T., Ceriola, G., Weng, Q., & Rajasekar, U. (2011). Identification and analysis of urban surface temperature patterns in Greater Athens, Greece, using MODIS imagery. *Remote Sensing of Environment, 115*(12), 3080–3090. https://doi.org/10.1016/j.rse.2011.06.014

Lacroix, R. N., & Stamatiou, E. (2021). Improving the quality of life in Athens with green roofs. *Energy and Buildings, 250*, Article 111298. https://doi.org/10.1016/j.enbuild.2021.111298

Lahoti, S., Kefi, M., Lahoti, A., & Saito, O. (2019). Mapping methodology of public urban green spaces using GIS: An example of Nagpur City, India. *Sustainability, 11*(7), Article 2166. https://doi.org/10.3390/su11072166

Li, Z., Zhang, F., Guo, P., & Jin, X. (2013). Remote sensing of land surface temperature: Progress and perspectives. *Journal of Geophysical Research: Atmospheres, 118*(10), 5111–5130. https://doi.org/10.1002/jgrd.50541

Lin, X., Cui, Y., Hao, S., Zhu, C., Zhang, P., & Zhao, H. (2024). Influence of urban landscape pattern on summer surface temperature and its spatial scale effects. *Geocarto International, 40*(1). https://doi.org/10.1080/10106049.2024.2441370

Liu, D., Tang, M., & Dong, N. (2022). Green city landscape design and planning based on GIS and analytic hierarchy process model. *Environmental Modeling and Assessment, 27*, 419–430.

Luck, M., & Wu, J. (2002). A gradient analysis of urban landscape pattern: A case study from the Phoenix metropolitan region, Arizona, USA. *Landscape Ecology, 17*(4), 327–339.

McGarigal, K., Cushman, S., & Ene, E. (2015). *FRAGSTATS v4: Spatial pattern analysis program for categorical maps*. University of Massachusetts Amherst. https://www.umass.edu/landeco/research/fragstats/fragstats.html

Miniandi, N. D., Jamal, M. H., Muhammad, M. K. I., & Shahid, S. (2025). Machine learning in modeling urban heat islands: A data-driven approach for Kuala Lumpur. *Earth Systems and Environment, 9*(3). https://doi.org/10.1007/s41748-025-00584-4

Morini, E., Touchaei, A. G., Castellani, B., Rossi, F., & Cotana, F. (2016). The impact of albedo increase to mitigate the urban heat island in Terni (Italy) using the WRF model. *Sustainability, 8*(10), Article 999. https://doi.org/10.3390/su8100999

NASA. (n.d.). *Landsat 8*. NASA Science. Retrieved April 15, 2026, from https://science.nasa.gov/mission/landsat-8/

Oke, T. R. (1982). The energetic basis of the urban heat island. *Quarterly Journal of the Royal Meteorological Society, 108*(455), 1–24.

Onačillová, M., Šúri, M., Šúriová, M., & Šúri, M. (2022). Combining Landsat 8 and Sentinel-2 data in Google Earth Engine to derive higher resolution land surface temperature maps in urban environment. *Remote Sensing, 14*(23), Article 6103. https://doi.org/10.3390/rs14236103

Rakshit, A., et al. (Eds.). (2022). *Soils in urban ecosystem*. Springer.

Romero Rodríguez, L., Sánchez Ramos, J., Guerrero Delgado, M. C., & Álvarez Domínguez, S. (2022). Implications of the urban heat island on the selection of optimal retrofitting strategies: A case study in a Mediterranean climate. *Urban Climate*. https://doi.org/10.1016/j.uclim.2022.101234

Roukounakis, N., Varotsos, K. V., Katsanos, D., Lemesios, I., Giannakopoulos, C., & Retalis, A. (2023). High resolution WRF modelling of extreme heat events and mapping of the urban heat island characteristics in Athens, Greece. *Sustainability, 15*(23), Article 16509. https://doi.org/10.3390/su152316509

Salvati, L., & Zitti, M. (2009). Territorial disparities, natural resource distribution, and land degradation: A case study in Southern Europe. *GeoJournal, 74*, 339–350.

Salvati, L., Sateriano, A., & Grigoriadis, S. (2013). Crisis and the city: Urban shrinkage in the Mediterranean region. *Environment and Planning A, 45*, 1471–1488.

Santamouris, M. (2015). Analyzing the heat island magnitude and characteristics in one hundred Asian and Australian cities and regions. *Science of the Total Environment, 512–513*, 582–598. https://doi.org/10.1016/j.scitotenv.2015.01.060

Schwaab, J., Meier, M., & Patt, A. (2023). Tree canopy expansion as a cooling strategy in European cities. *Environmental Research Letters, 18*(2), Article 024012. https://doi.org/10.1088/1748-9326/acb3a2

Smola, A., & Schölkopf, B. (2004). A tutorial on support vector regression. *Statistics and Computing, 14*(3), 199–222.

Spyrou, C., Koukoula, M., Saviolakis, P.-M., Zerefos, C., Loupis, M., Masouras, C., Pappa, A., & Katsafados, P. (2024). Green roofs as a nature-based solution to mitigate urban heating during a heatwave event in the city of Athens, Greece. *Sustainability, 16*(22), Article 9729. https://doi.org/10.3390/su16229729

Stessens, P., Canters, F., Huysmans, M., & Khan, A. Z. (2021). Urban green space qualities: An integrated approach towards GIS-based assessment reflecting user perception. *Urban Forestry & Urban Greening, 57*, Article 126938.

Vapnik, V. N. (1995). *The nature of statistical learning theory*. Springer.

Weng, Q. (2004). Thermal infrared remote sensing for urban climate and environmental studies: Methods, applications, and trends. *ISPRS Journal of Photogrammetry and Remote Sensing, 59*(4), 273–286.

Yu, X., Guo, Q., & Wu, Y. (2020). Analysis of the impact of mixed pixels on land surface temperature retrieval from remote sensing data. *Remote Sensing, 12*(6), Article 925. https://doi.org/10.3390/rs12060925

Zha, Y., Gao, J., & Ni, S. (2003). Use of normalized difference built-up index in automatically mapping urban areas from TM imagery. *International Journal of Remote Sensing, 24*(3), 583–594. https://doi.org/10.1080/01431160304987

Zhao, X. F., Deng, L., Wang, H. N., Hua, L. Z., & Chen, F. (2014). Landscape classifications for landscape metrics-based assessment of urban heat island: A comparative study. *IOP Conference Series: Earth and Environmental Science, 17*, Article 012155. https://doi.org/10.1088/1755-1315/17/1/012155

Zhong, Y., Hu, X., & Zhang, L. (2019). Cross-scene deep transfer learning for urban land-use classification with remote-sensing images. *IEEE Transactions on Geoscience and Remote Sensing, 57*(8), 4959–4973.

Zoulia, I., Santamouris, M., & Dimoudi, A. (2009). Monitoring the effect of urban green areas on the heat island in Athens. *Environmental Monitoring and Assessment, 156*, 275–292.

7. Appendices

Appendix A. Google Earth Engine Scripts

NDVI scripts:

NDVI scripts

https://drive.google.com/drive/folders/1zYkB5BW_Z7VTyKYedyZKXZrRoQPCzvj2?usp=sharing

NDBI scripts:

NDBI scripts

https://drive.google.com/drive/folders/1zYkB5BW_Z7VTyKYedyZKXZrRoQPCzvj2?usp=sharing

DEM script:

DEM script

https://drive.google.com/drive/folders/1zYkB5BW_Z7VTyKYedyZKXZrRoQPCzvj2?usp=sharing

Appendix B. Machine-Learning Code

Machine Learning Codes

https://drive.google.com/drive/folders/1zYkB5BW_Z7VTyKYedyZKXZrRoQPCzvj2?usp=sharing

Appendix C. Colab results

Comprehensive Colab results

https://drive.google.com/drive/folders/1zYkB5BW_Z7VTyKYedyZKXZrRoQPCzvj2?usp=sharing

Appendix D. Neighborhood-Level Metrics and Input Variables

Comprehensive table of landscape metrics (PLAND, LPI, FRAC, ED, LSI) per neighborhood used as input for machine-learning models.

https://drive.google.com/drive/folders/1zYkB5BW_Z7VTyKYedyZKXZrRoQPCzvj2?usp=sharing

Appendix E Correlation Analysis Between LST and Spectral Indices from Google Earth Engine

Comprehensive Correlation Analysis Between LST and Spectral Indices from Google Earth Engine.

https://drive.google.com/drive/folders/1zYkB5BW_Z7VTyKYedyZKXZrRoQPCzvj2?usp=sharing

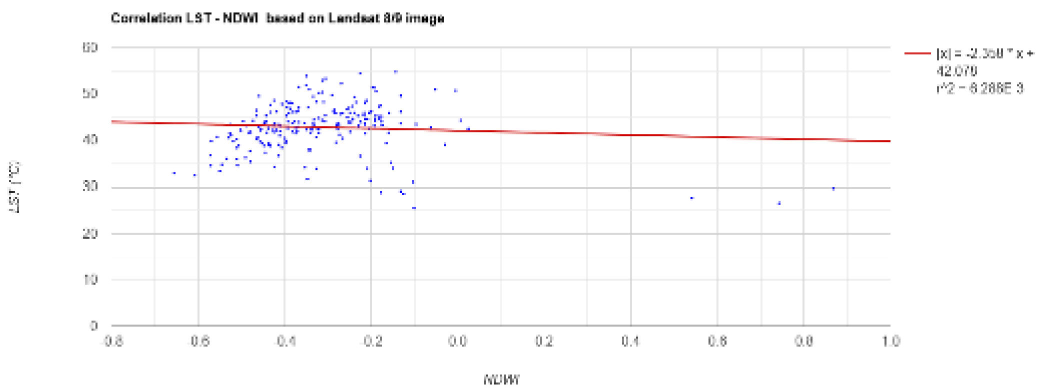

Figure 10 Correlation LST-NDWI (June 2024)

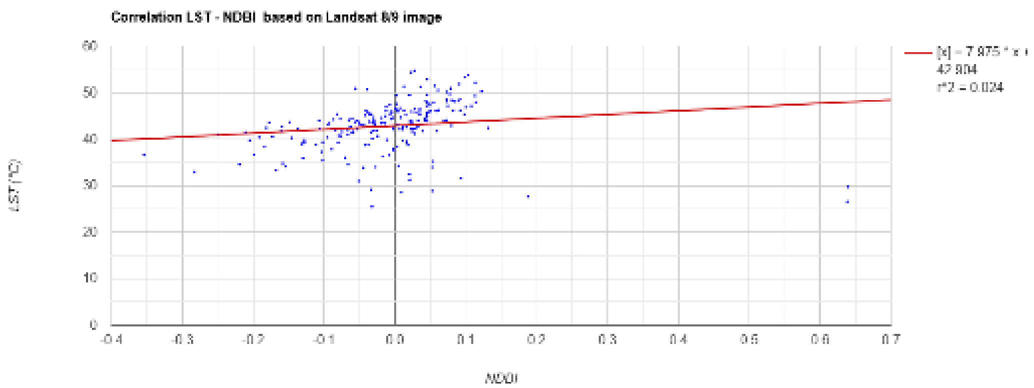

Figure 11 Correlation LST NDBI (June 2024)

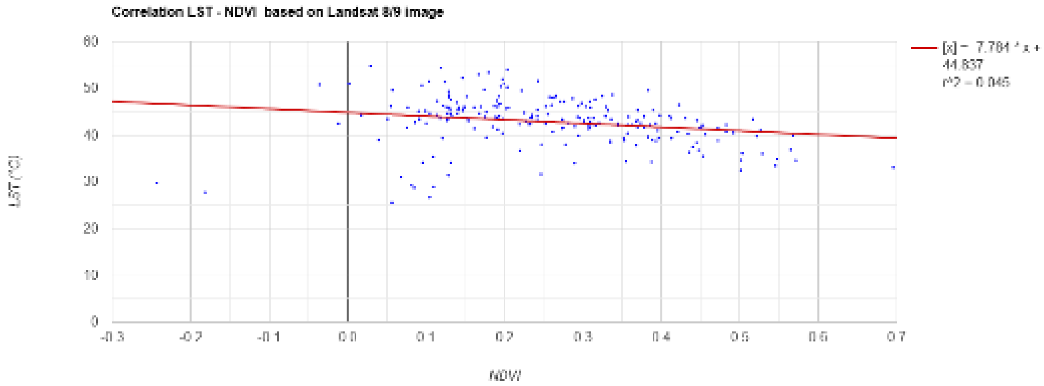

Figure 12 Correlation LST NDVI (June 2024)

June Results

The June results display that the relationship between LST and the examined indices is generally weak, with NDWI, NDBI, and NDVI each providing only limited explanatory power. The relationship of NDWI with LST was weakly negative (R^2=0.0063), showing that water and moisture presence applied only a marginal cooling effect on surface temperatures, as most pixels had not water feature. NDBI index showed a weak positive correlation (R^2=0.024), confirming that built-up density contributed to higher LST values, though the effect was minor. In comparison, NDVI presented the highest correlation of the three metrics, and its negative slope showed that vegetated areas had a greater effect on reducing surface temperatures. Overall, the results in June demonstrate that urban vegetated areas are the single greatest influence in reducing heat, however, the low r-squared values also suggest the thermal dynamics are complex and depend on multiple, interacting variables.

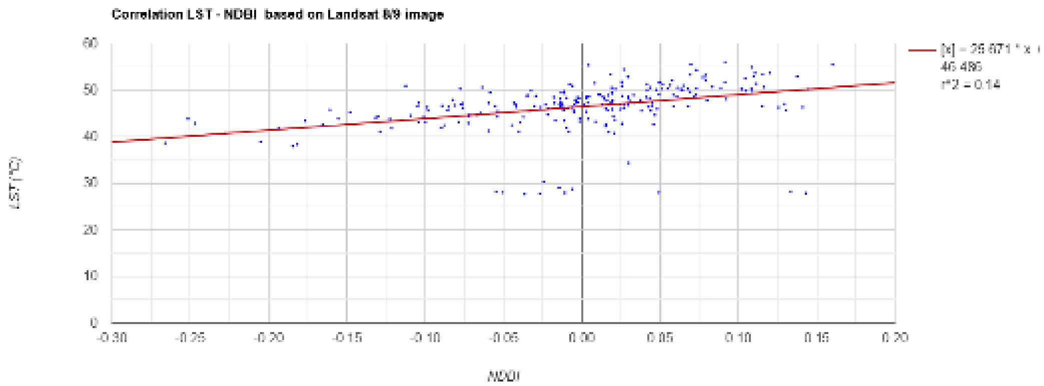

Figure 13 Correlation LST-NDBI (July 2024)

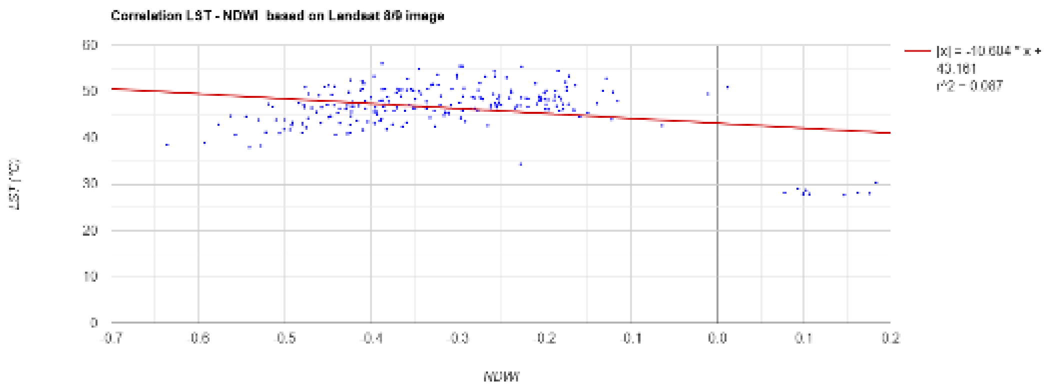

Figure 14 Correlation LST-NDWI (July 2024)

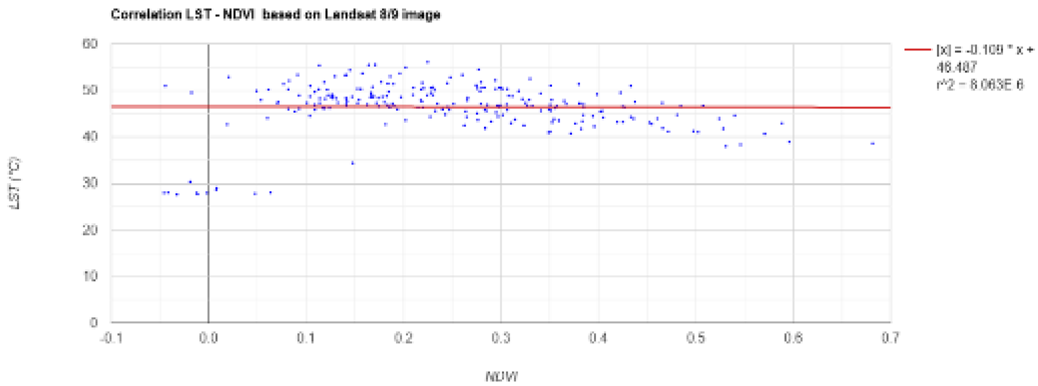

Figure 15 Correlation LST-NDVI (July 2024)

July Results

In July, the relationships of LST with the other three indices strengthened from June, indicating an increase of summer heat. Indeed, the relationship of NDWI with LST became more negative (R^2 = 0.087), showing the continued cooling effect of water presence, though it was still not strong in explanatory power. NDBI, however, had a more pronounced positive correlation (R^2 = 0.14), suggesting that built-up surfaces accounted for much more variation in LST than in June, emphasizing the increased impervious density during peak summer. On the other hand, NDVI in July showed no correlation with LST at all ($R^2 \approx 0$), indicating that the cooling role of vegetation in such extreme heat conditions, dominated by other key factors in urban morphology and surface properties, became less detectable. Overall, the July results reflect that built-up density is the main driver of surface heat in July, while any moderating influence of vegetation is weaker in extreme summer conditions.

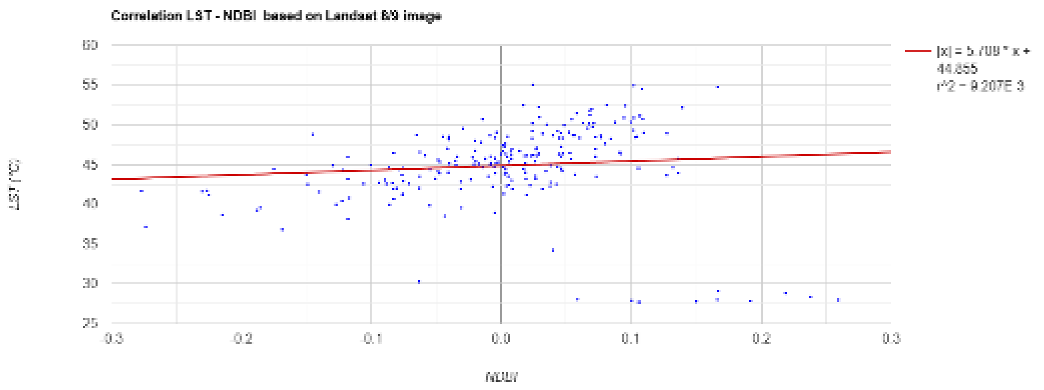

Figure 16 Correlation LST-NDBI (August 2024)

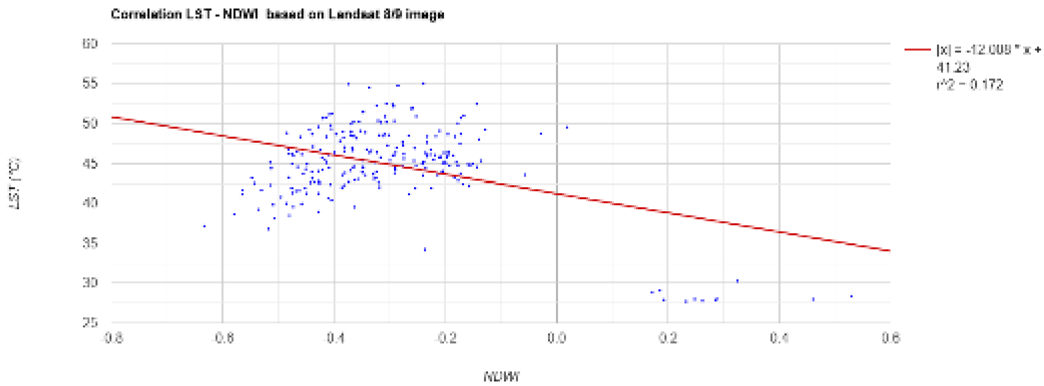

Figure 17 Correlation LST-NDWI (August 2024)

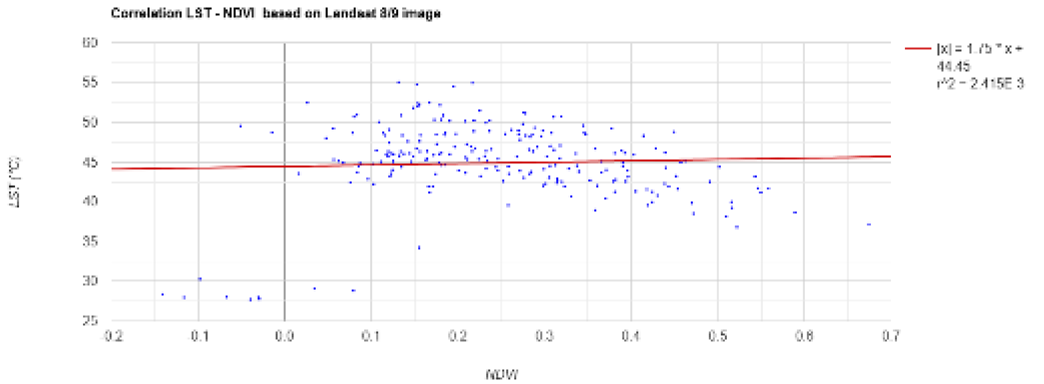

Figure 18 Correlation LST-NDVI (August 2024)

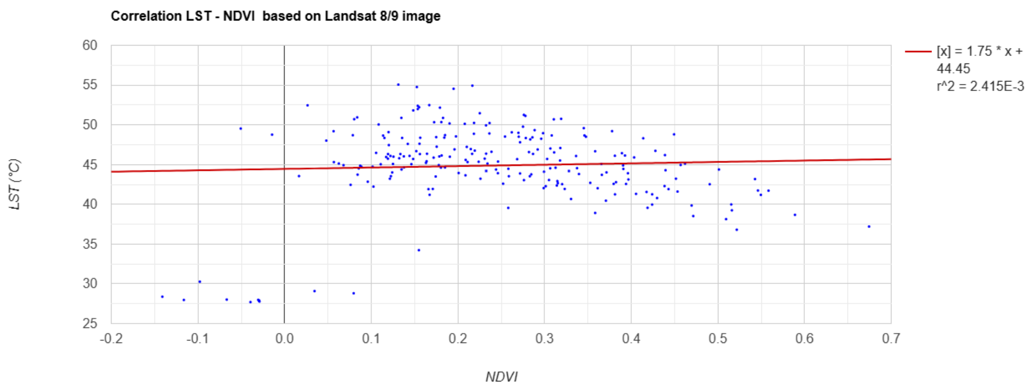

Figure 19 Correlation LST-NDVI (August 2024)

August Results

The August results show a mixed picture, with NDWI being the main LST predictor, while the NDVI and NDBI remain weakly associated. NDWI presented a negative relation (R^2=0.172), one that was stronger compared to previous months, probably reflecting an enhanced moist or water rich surface cooling effect under the late summer drying conditions where thermal contrasts may be more pronounced. NDBI has shown a minor positive slope of R^2=0.0029 and, thus, the variation in built-up density contributed little explanatory power during August, probably because other confounding factors are involved, such as soil moisture, reflectivity and sea breeze effects. NDVI shows a shallow positive slope with very low explanatory power (R^2=0.0024), hence effectively no correlation with LST during late summer for NDVI, probably due to NDVI saturation and mixed pixel effects. The analysis of August bolsters the idea of the primacy of water-related dynamics in regulating LST, while vegetation and built-up indices provided limited explanatory capacity during late summer.

Appendix F Supplemental Maps

Comprehensive Analysis of Supplemental Maps

https://drive.google.com/drive/folders/1zYkB5BW_Z7VTyKYedyZKXZrRoQPCzvj2?usp=sharing

DEM and Slope

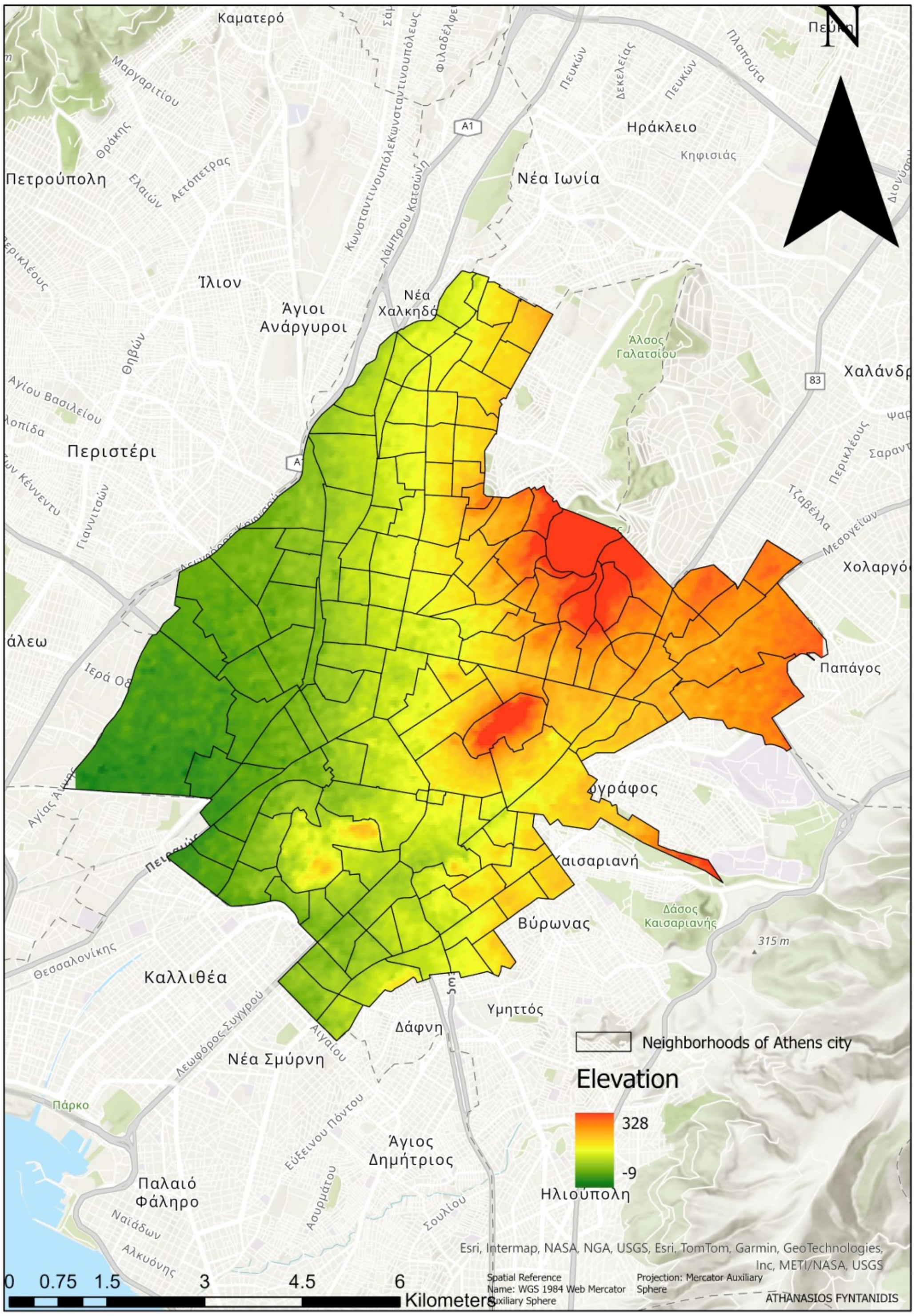

Figure 20 DEM map of Athens city.

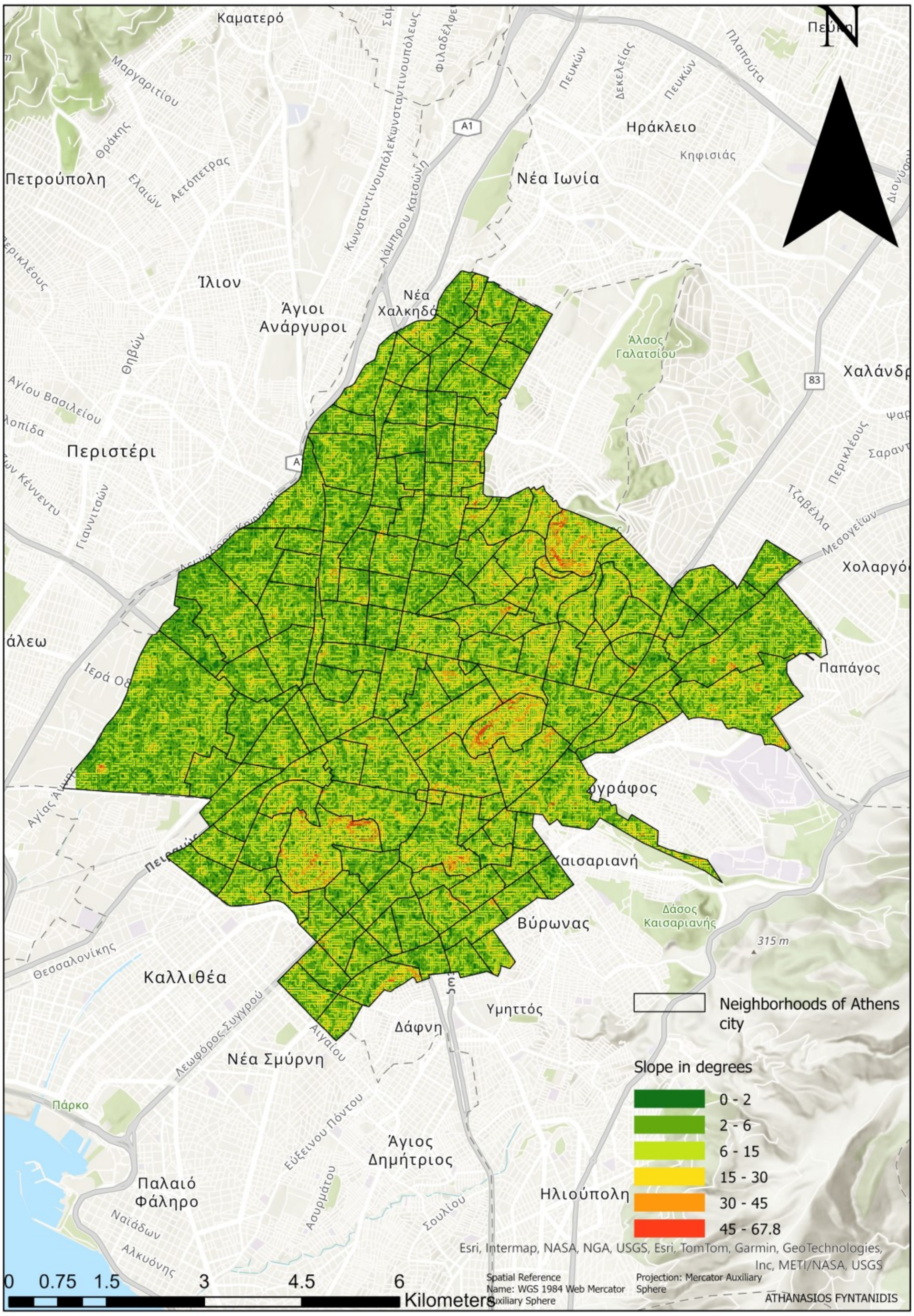

Figure 21 Slope map for Athens’s city.

LSI

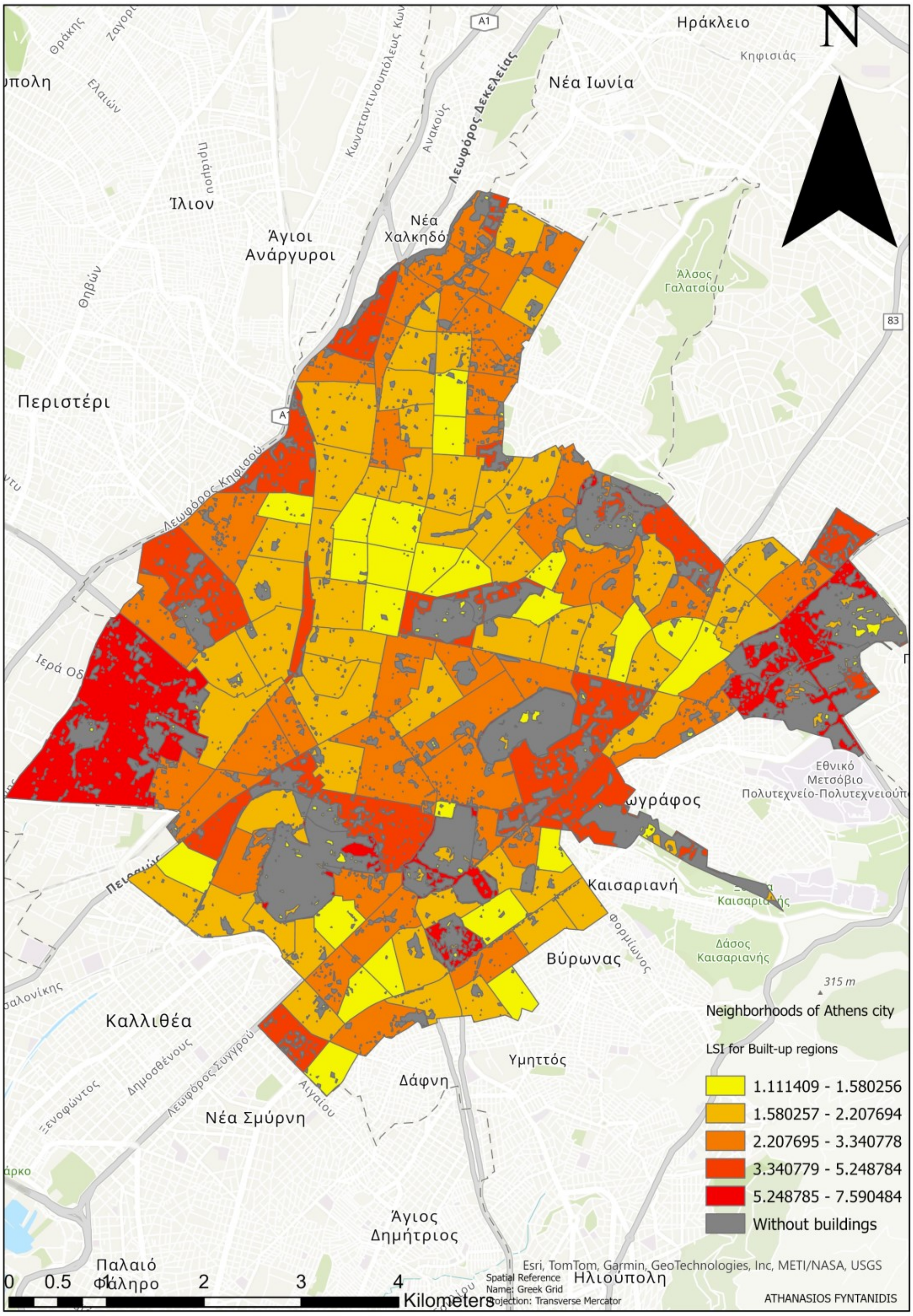

Figure 22 LSI map for Built-up regions of Athens city.

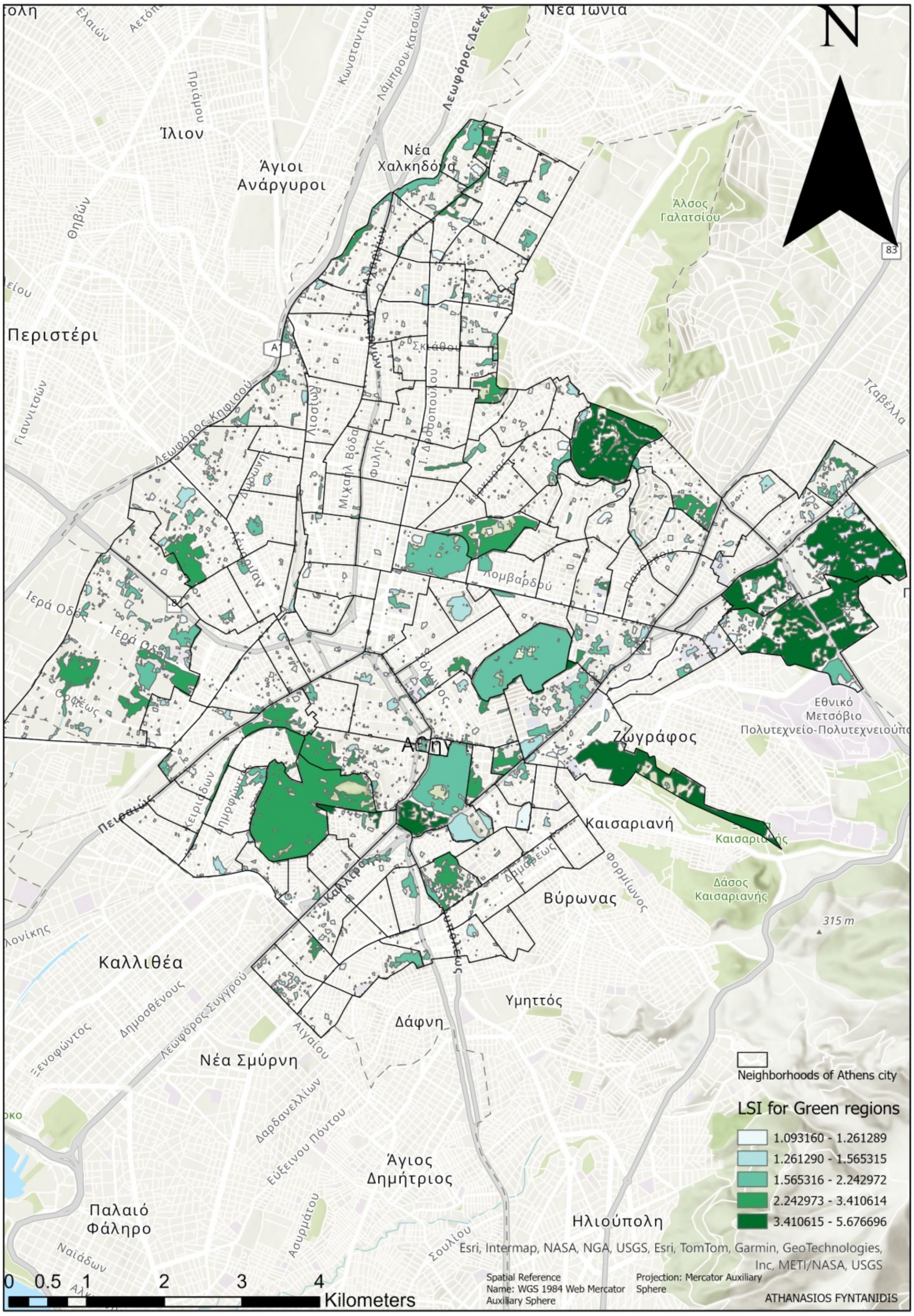

Figure 23 LSI map for Green regions of Athens city.

ED

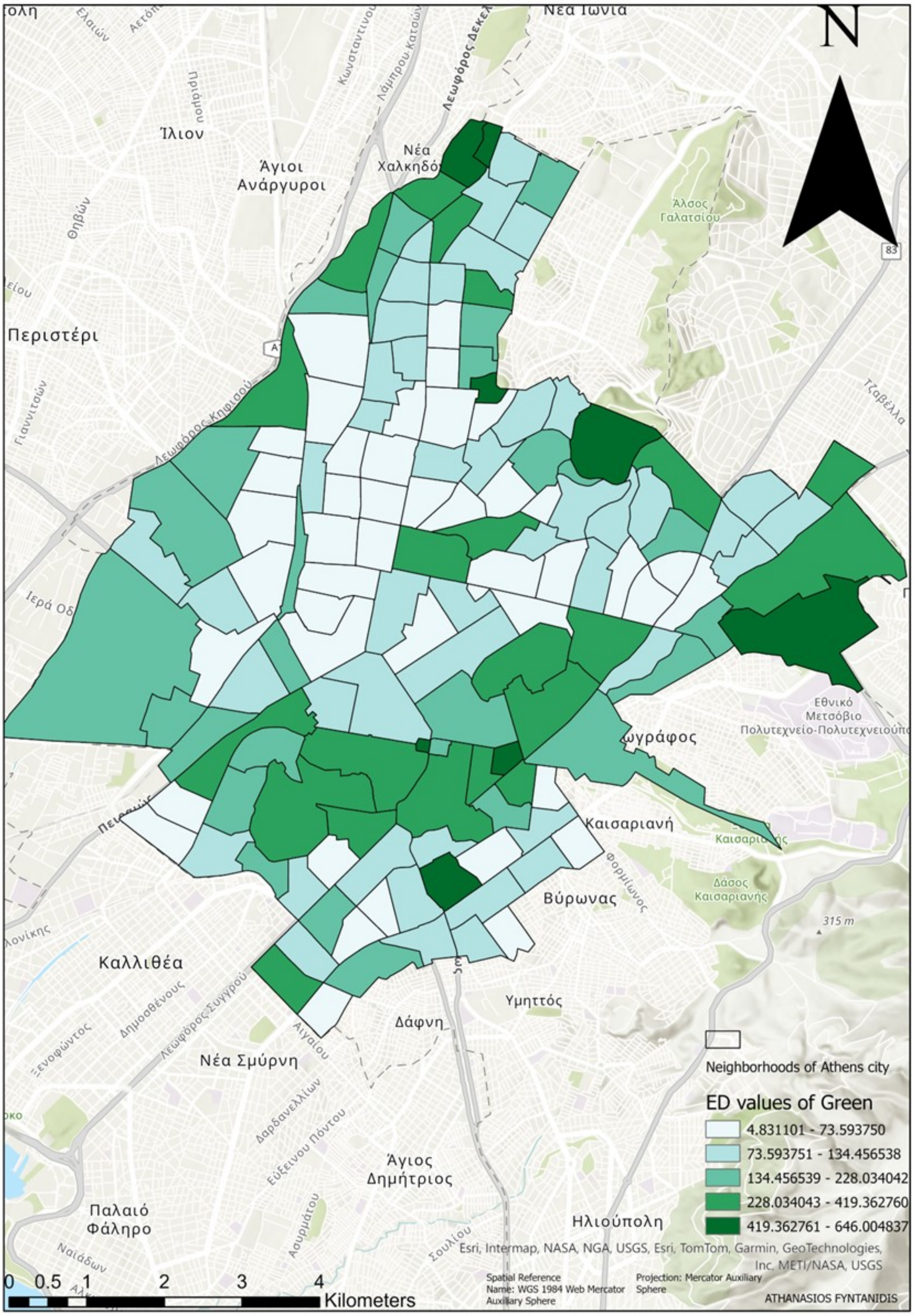

Figure 24 ED map for Green in Athens city.

LPI

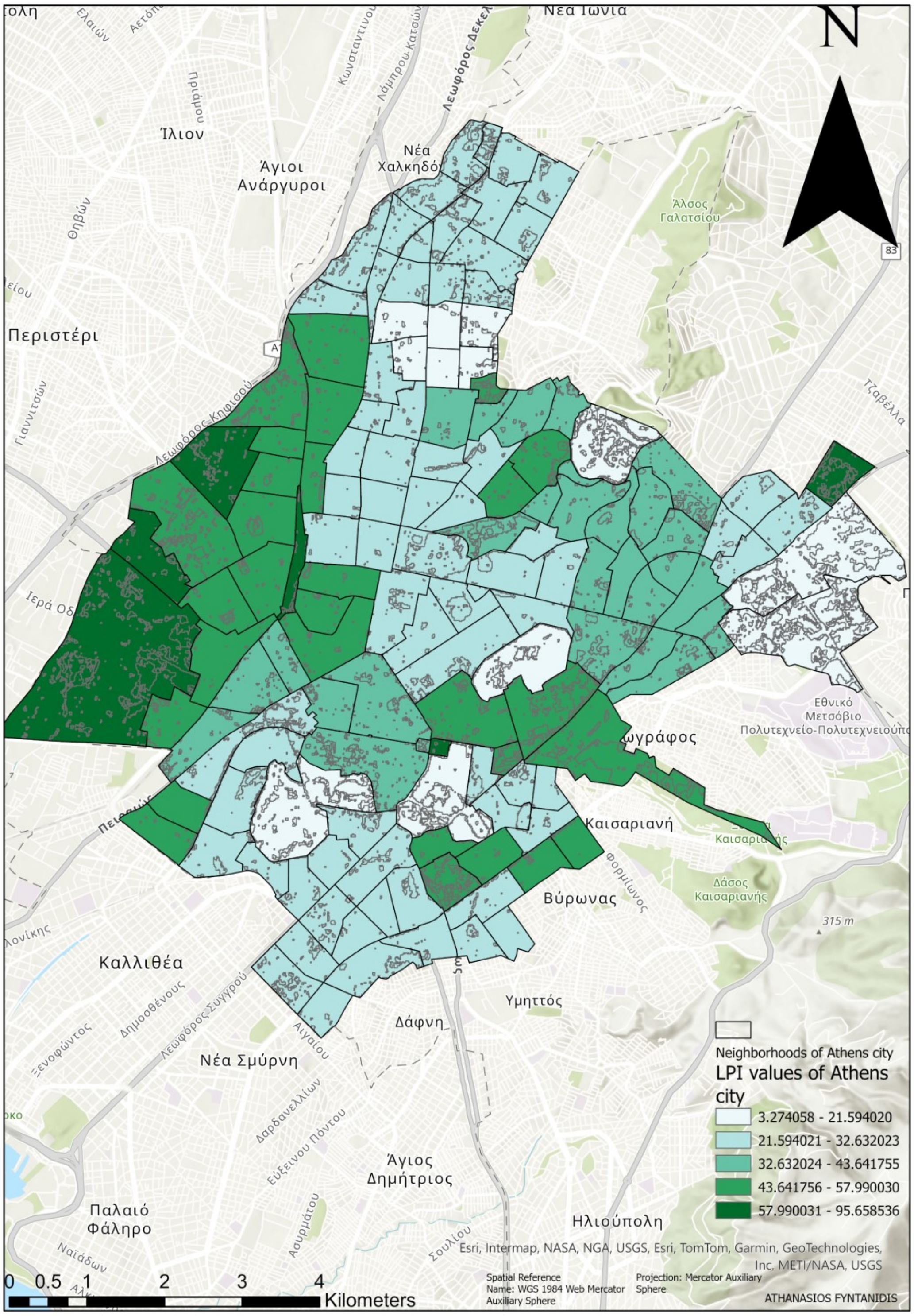

Figure 25 LPI map of Athens city.

FRAC

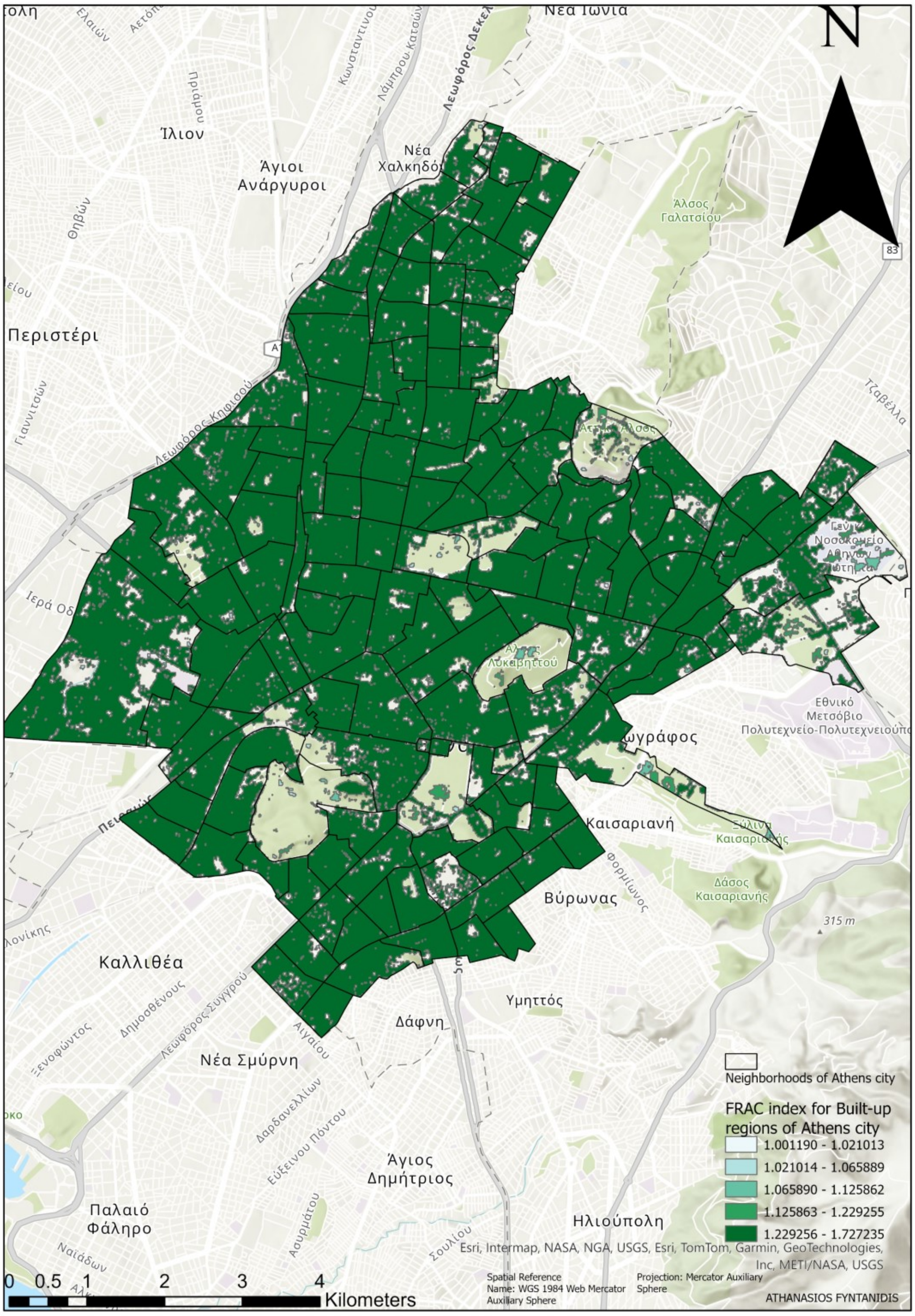

Figure 26 FRAC index map of Built-up regions in Athens’s city.

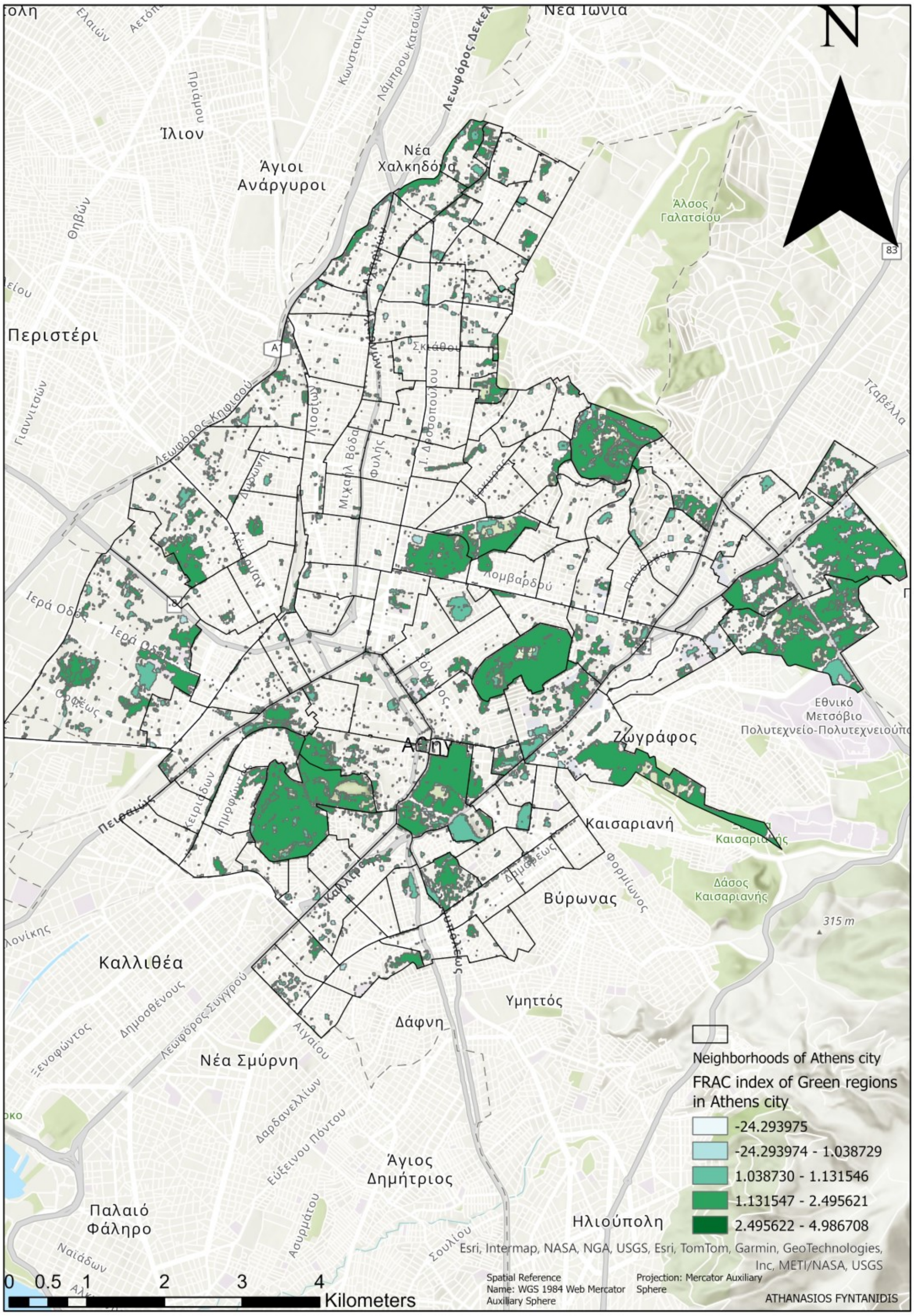

Figure 27 FRAC index map of Green regions in Athens's city

PLAND

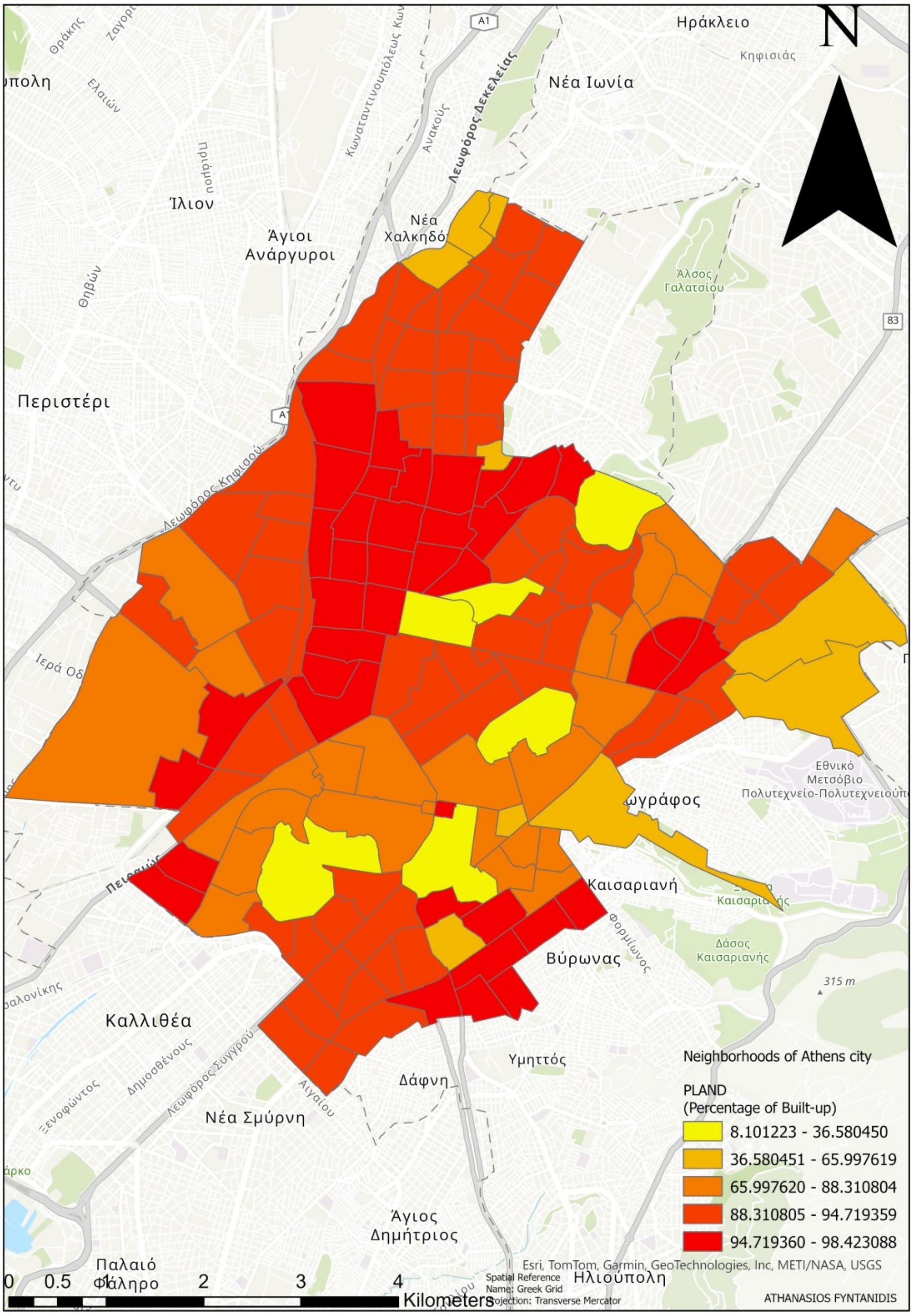

Figure 28 PLAND map of Built-up regions in Athens’s city.

LST

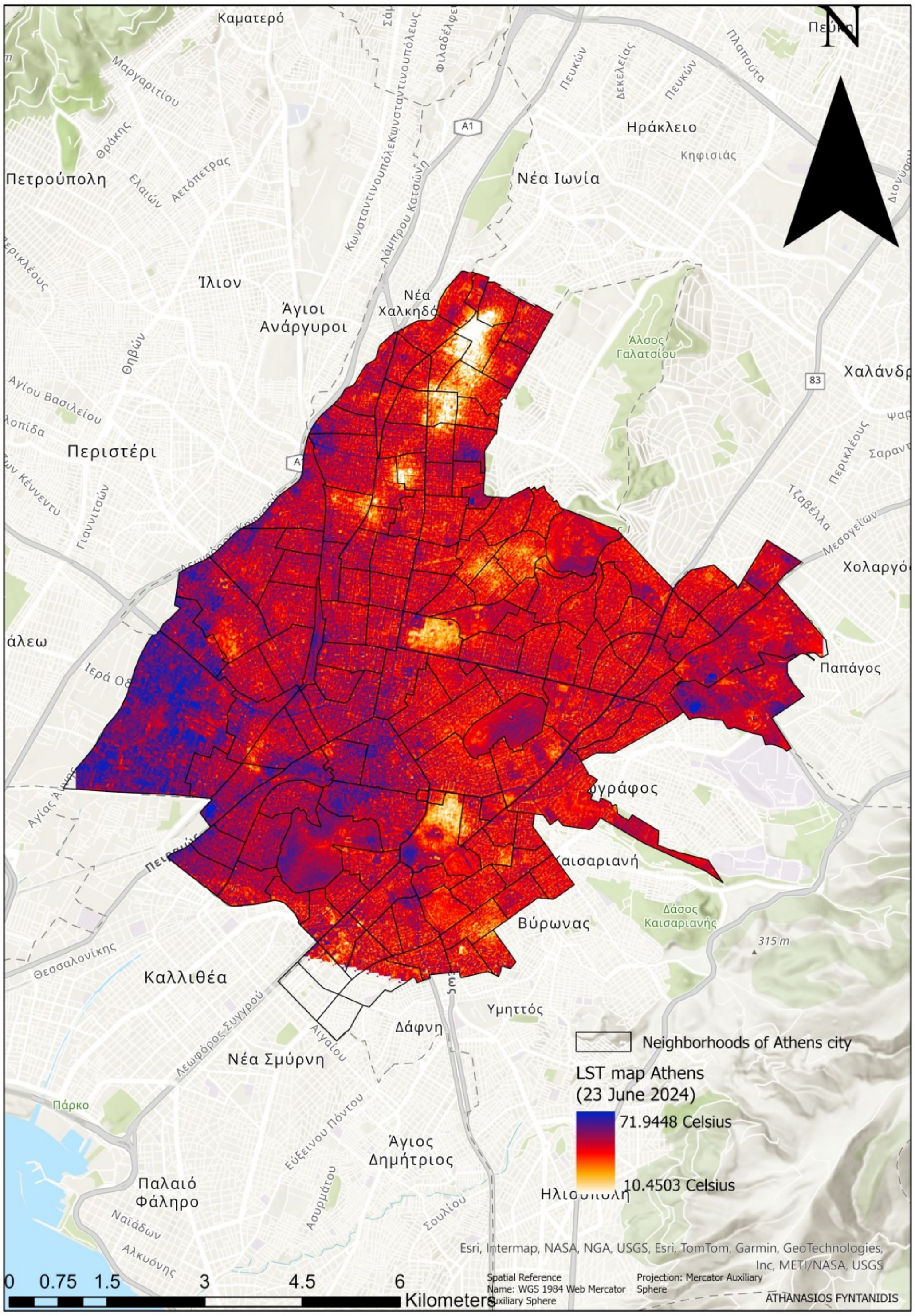

Figure 29 LST map in Athens's city (23 June 2024)

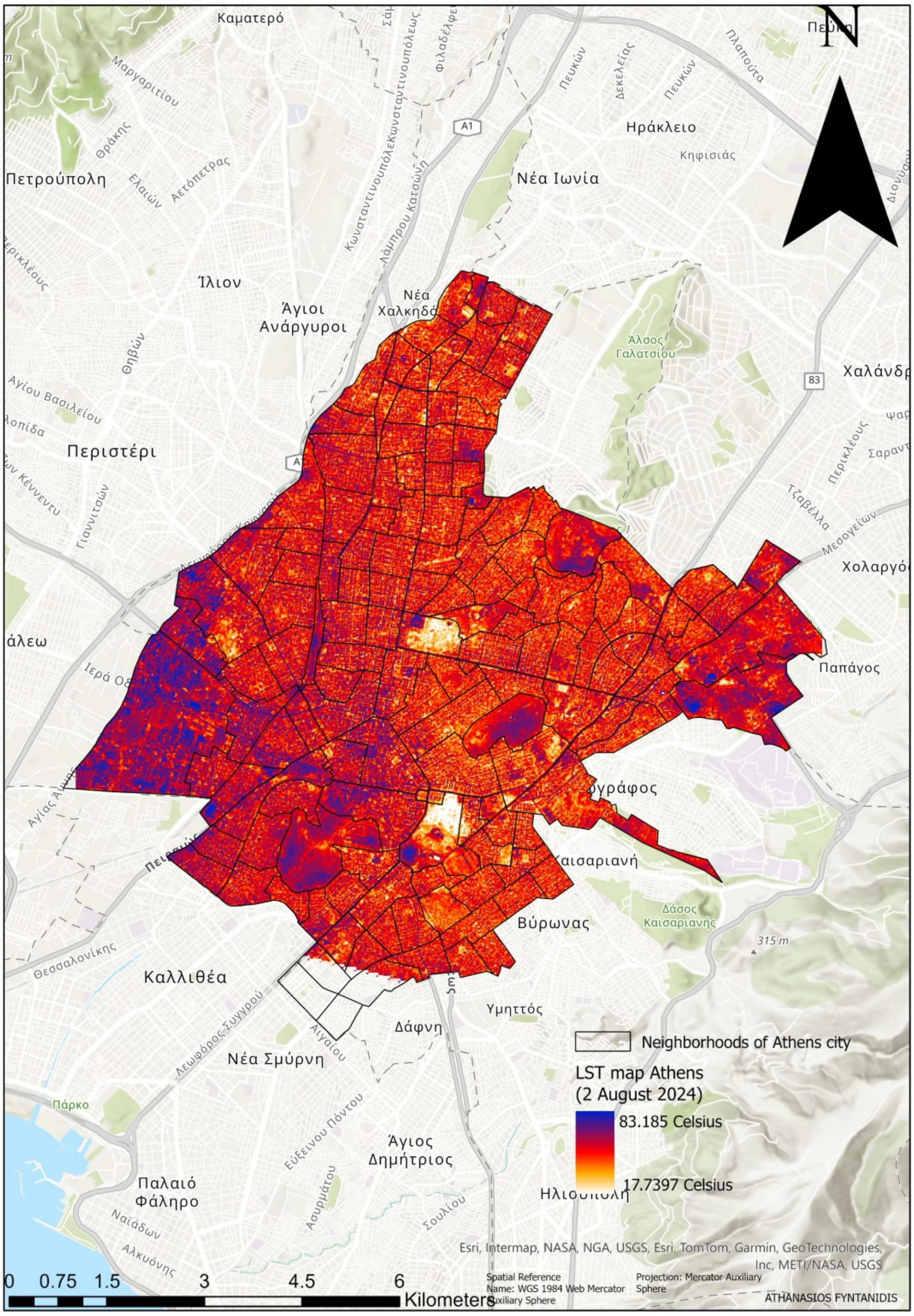

Figure 30 LST map in Athens's city (2 August 2024).

GWR

Interpretation of GWR Results (June - Built-up - TOPO – Green): The GWR coefficient maps provide insight into how built-up related variables influence LST across neighborhoods in Athens during June 2024. Also, there are GWR coefficient maps for Mean Values of DEM raster, for Mean Values of Slope, and for green areas.

Landscape Shape Index (LSI – Built-up): Areas with higher LSI coefficients, indicated by positive values in a range from 0.29885 to 18.174064, show a strong link between irregular and fragmented built-up forms and elevated land surface temperatures (LST). In contrast, negative coefficients denoted in a range from -18.736330 to 0.29885, showing neighborhoods where built-up fragmentation does not significantly influence warming, likely due to a mix of land uses or shading effects. Central and densely populated districts exhibit the strongest positive correlations, emphasizing how irregular built structures can increase local heat.

Edge Density (ED – Built-up): Positive coefficients also reveal neighborhoods where a greater density of built-up edges—meaning more boundaries between urban areas and other types of land—correlates with higher LST. Negative values, found in some of the peripheral neighborhoods, mean that ED there does not increase LST noticeably, maybe because of the green surroundings or lower urban densities. This is the double effect of edges: in densely urbanized areas, they contain heat, whereas in the larger urban formations, their effect gets diluted.

Normalized Difference Built-up Index (NDBI): NDBI uncovers the strongest pattern: strong positive coefficients (turquoise–green) emerge over most of the inner neighborhoods, as predicted, confirming that higher built-up intensity is a dominant driver for LST. Negative coefficients in a few regions are potential markers for local conditions where developed pixels are mixed with vegetation or open ground and diminish their thermal impact. This heterogeneity in space is also in line with earlier findings that NDBI is a strong predictor of UHI intensity (Zha et al. 2003) (Guha et al. 2018).

General Insight

Overall, the GWR results confirm that built-up form, density, and intensity are determinants of neighborhood-scale thermal conditions in Athens. The space variability underscores that while some areas have obvious built-up–heat relations, others may be influenced by moderated effects of local greening, slope, or airflow corridors. This underscores the importance of adopting localized neighborhood-based strategies for UHI mitigation rather than blanket interventions.

Mean Values DEM and Slope

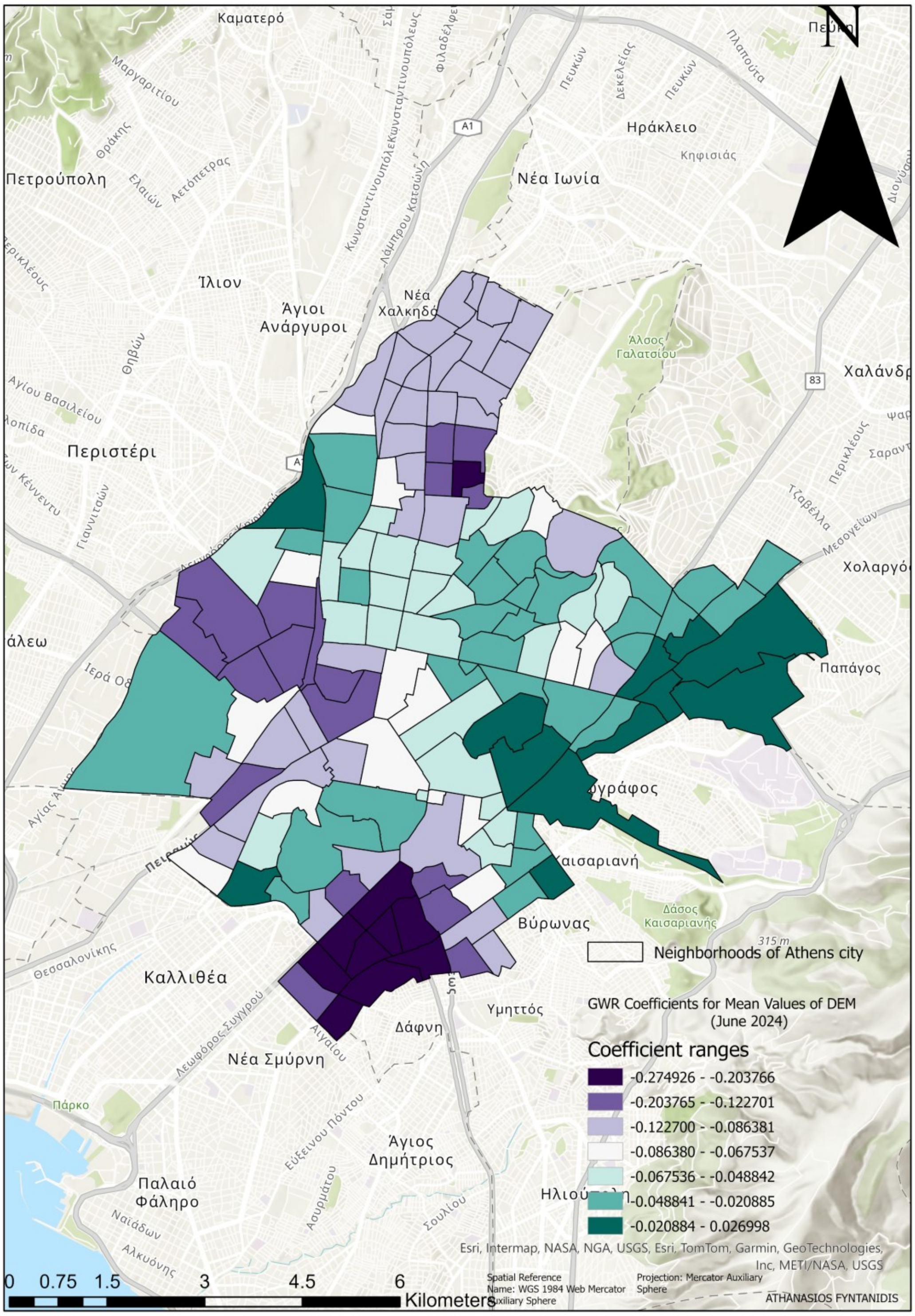

Figure 31 GWR map of Coefficient ranges for Mean Values of DEM.

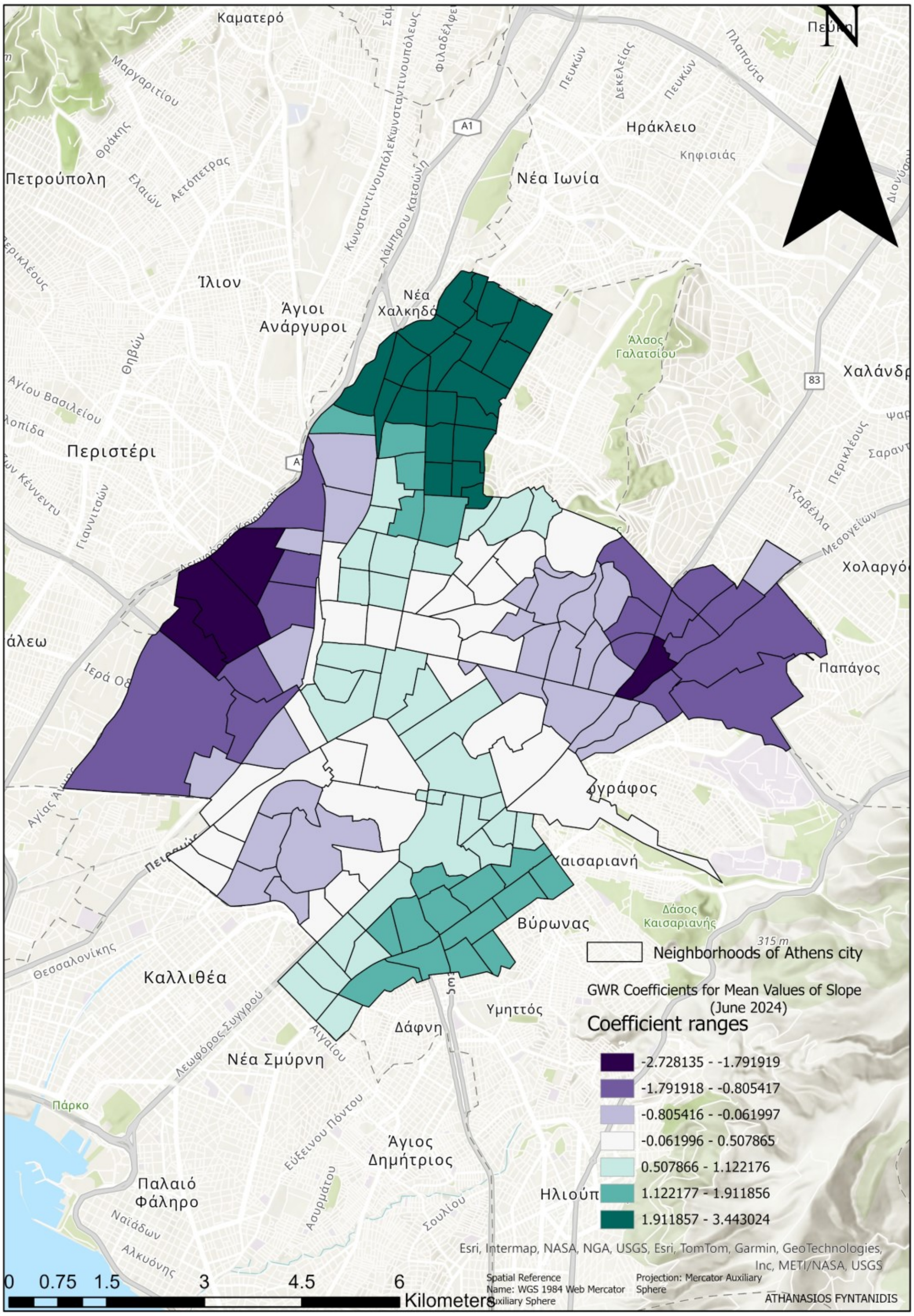

Figure 32 GWR map of Coefficient ranges for Mean Values of Slope.

Mean Values of NDVI

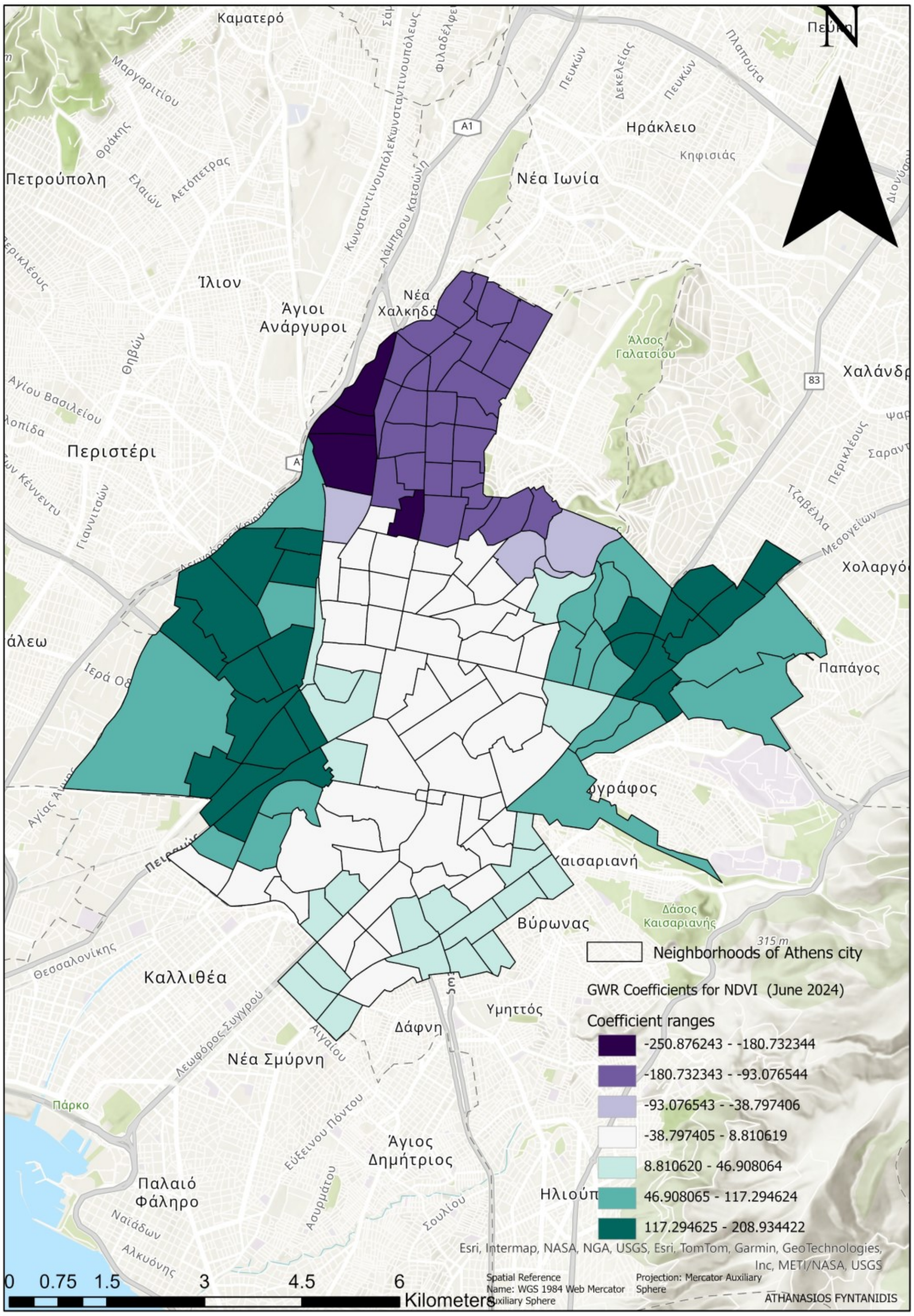

Figure 33 GWR map of Coefficient ranges for Mean Values of NDVI (June 2024).

FRAC

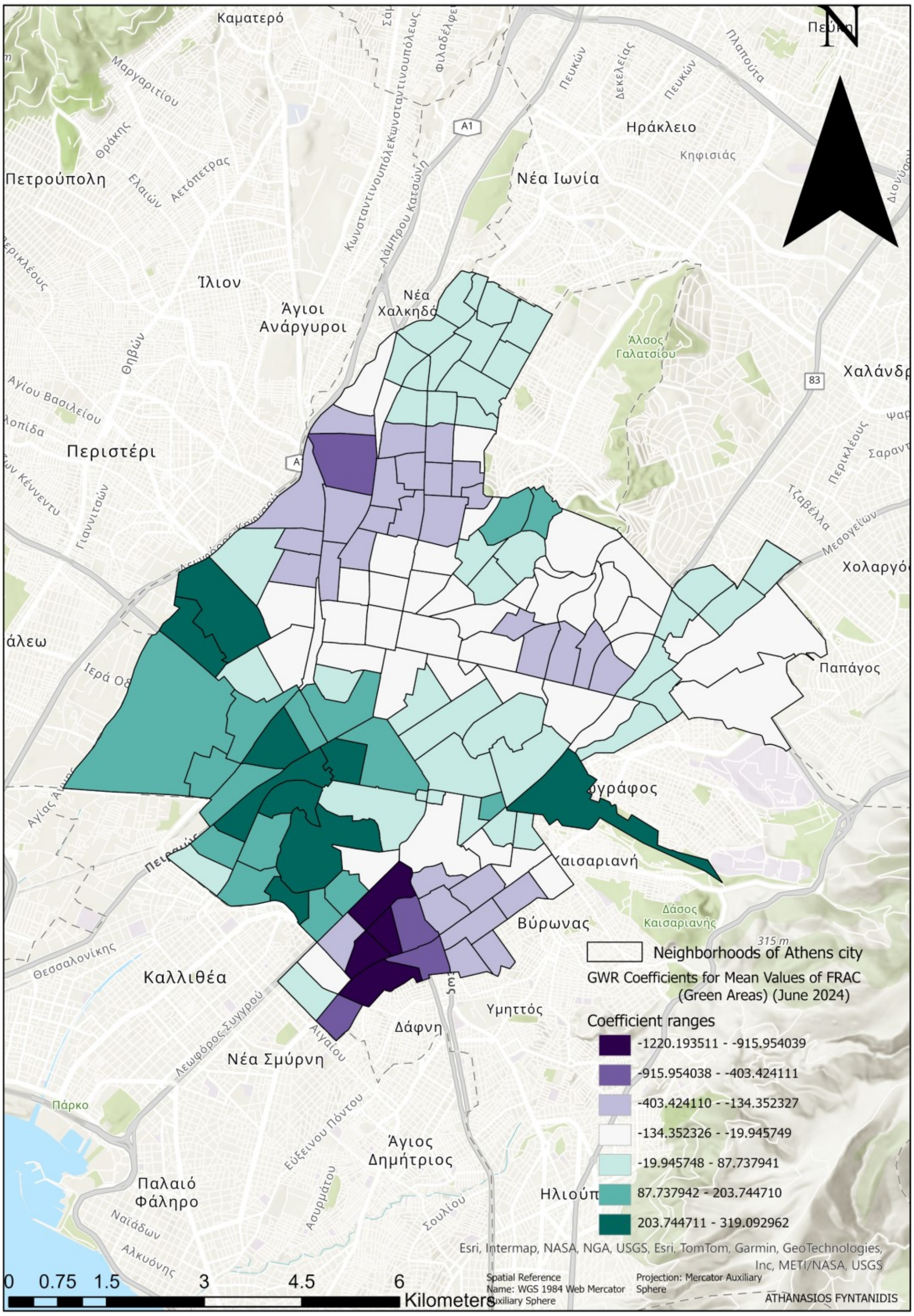

Figure 34 GWR map of Coefficient ranges for Mean Values of FRAC (Green Areas).

NDVI patterns

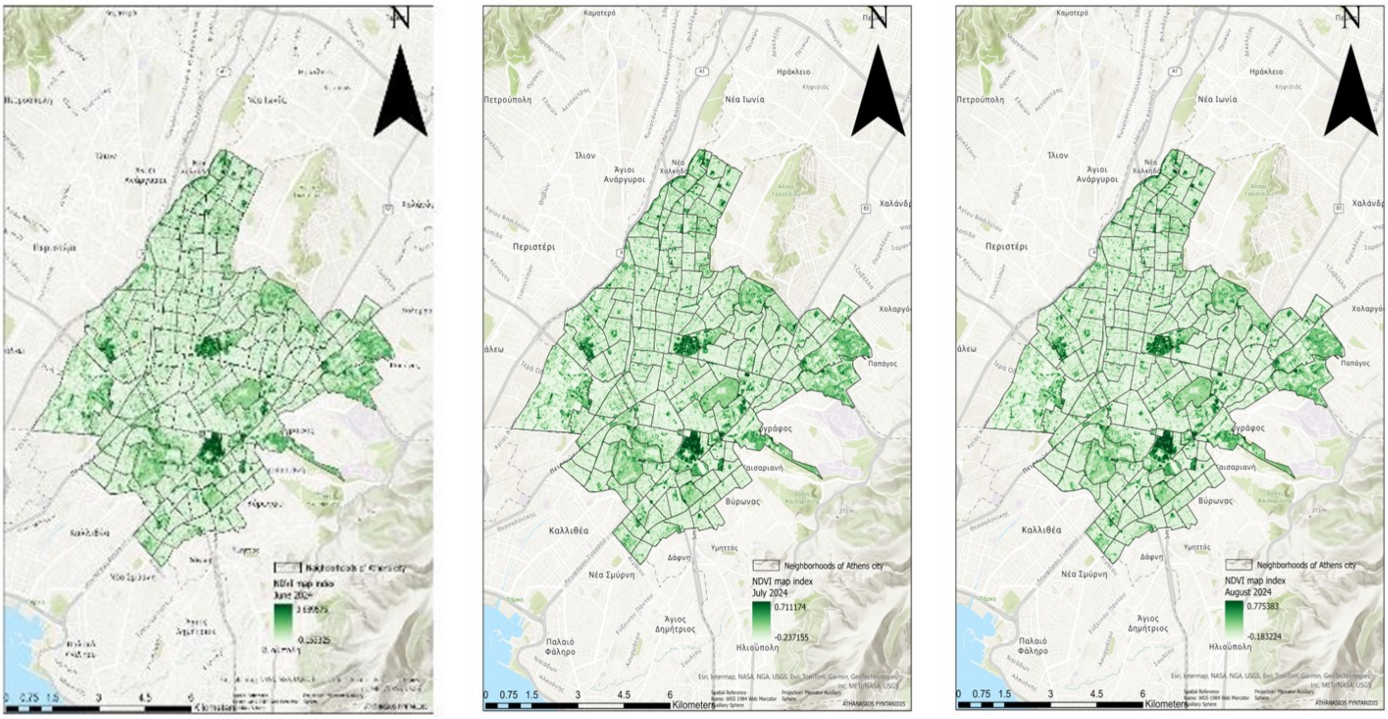

Figure 35 NDVI map in Athens's city (23 June 2024/ 13 July 2024/ 02 August 2024).

NDBI patterns

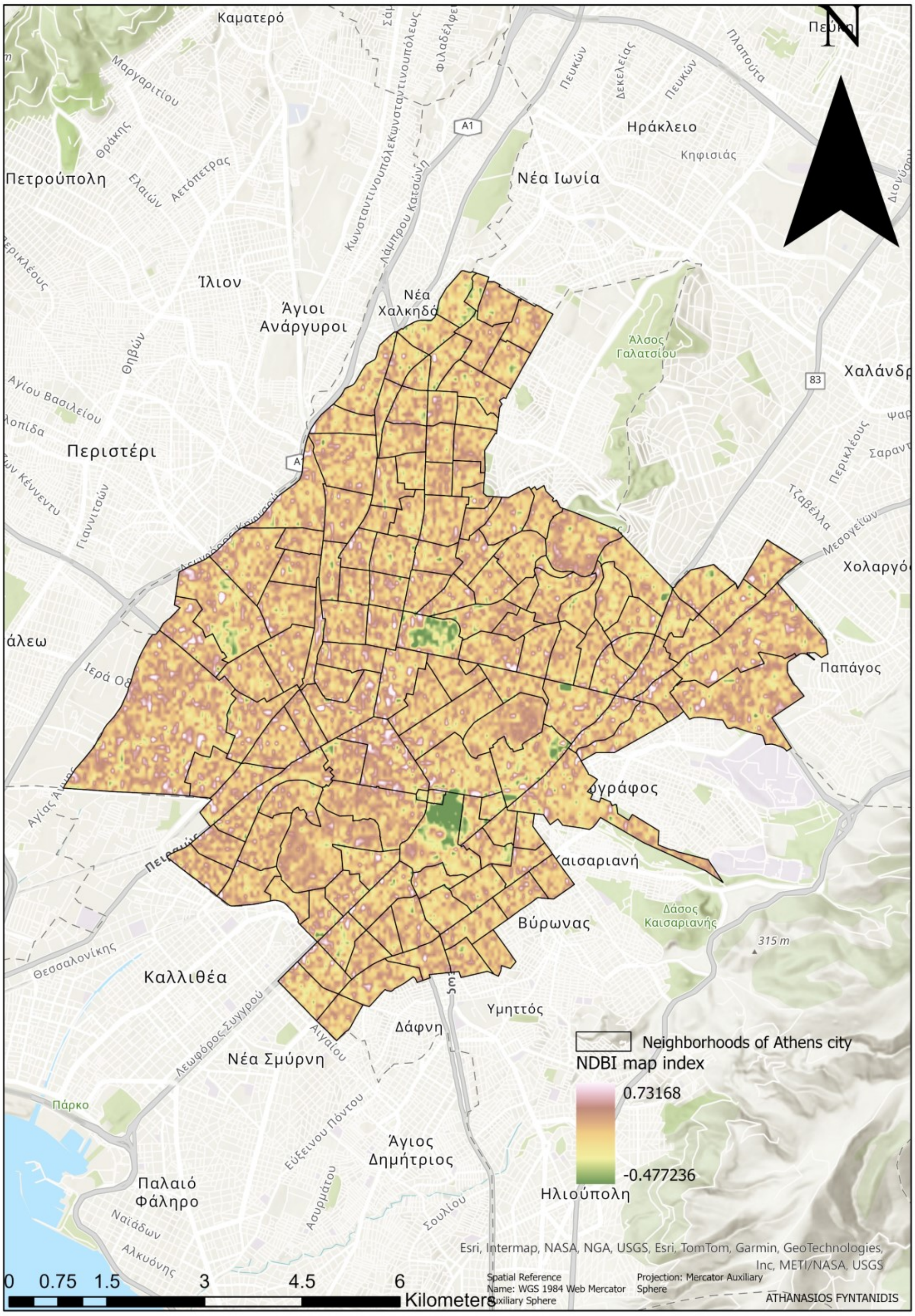

Figure 36 NDBI map of Athens city.

Series from Lund University

Department of Physical Geography and Ecosystem Science

Master Thesis in Geographical Information Science

1. Anthony Lawther: The application of GIS-based binary logistic regression for slope failure susceptibility mapping in the Western Grampian Mountains, Scotland (2008).

2. Rickard Hansen: Daily mobility in Grenoble Metropolitan Region, France. Applied GIS methods in time geographical research (2008).

3. Emil Bayramov: Environmental monitoring of bio-restoration activities using GIS and Remote Sensing (2009).

4. Rafael Villarreal Pacheco: Applications of Geographic Information Systems as an analytical and visualization tool for mass real estate valuation: a case study of Fontibon District, Bogota, Columbia (2009).

5. Siri Oestreich Waage: a case study of route solving for oversized transport: The use of GIS functionalities in transport of transformers, as part of maintaining a reliable power infrastructure (2010).

6. Edgar Pimiento: Shallow landslide susceptibility – Modelling and validation (2010).

7. Martina Schäfer: Near real-time mapping of floodwater mosquito breeding sites using aerial photographs (2010).

8. August Pieter van Waarden-Nagel: Land use evaluation to assess the outcome of the programme of rehabilitation measures for the river Rhine in the Netherlands (2010).

9. Samira Muhammad: Development and implementation of air quality data mart for Ontario, Canada: A case study of air quality in Ontario using OLAP tool. (2010).

10. Fredros Oketch Okumu: Using remotely sensed data to explore spatial and temporal relationships between photosynthetic productivity of vegetation and malaria transmission intensities in selected parts of Africa (2011).

11. Svajunas Plunge: Advanced decision support methods for solving diffuse water pollution problems (2011).

12. Jonathan Higgins: Monitoring urban growth in greater Lagos: A case study using GIS to monitor the urban growth of Lagos 1990 - 2008 and produce future growth prospects for the city (2011).

13. Mårten Karlberg: Mobile Map Client API: Design and Implementation for Android (2011).

14. Jeanette McBride: Mapping Chicago area urban tree canopy using color infrared imagery (2011).

15. Andrew Farina: Exploring the relationship between land surface temperature and vegetation abundance for urban heat island mitigation in Seville, Spain (2011).

16. David Kanyari: Nairobi City Journey Planner: An online and a Mobile Application (2011).

17. Laura V. Drews: Multi-criteria GIS analysis for siting of small wind power plants - A case study from Berlin (2012).

18. Qaisar Nadeem: Best living neighborhood in the city - A GIS based multi criteria evaluation of ArRiyadh City (2012).

19. Ahmed Mohamed El Saeid Mustafa: Development of a photo voltaic building rooftop integration analysis tool for GIS for Dokki District, Cairo, Egypt (2012).

20. Daniel Patrick Taylor: Eastern Oyster Aquaculture: Estuarine Remediation via Site Suitability and Spatially Explicit Carrying Capacity Modeling in Virginia's Chesapeake Bay (2013).

21. Angeleta Oveta Wilson: A Participatory GIS approach to unearthing Manchester's Cultural Heritage 'gold mine' (2013).

22. Ola Svensson: Visibility and Tholos Tombs in the Messenian Landscape: A Comparative Case Study of the Pylian Hinterlands and the Soulima Valley (2013).

23. Monika Ogden: Land use impact on water quality in two river systems in South Africa (2013).

24. Stefan Rova: A GIS based approach assessing phosphorus load impact on Lake Flaten in Salem, Sweden (2013).

25. Yann Buhot: Analysis of the history of landscape changes over a period of 200 years. How can we predict past landscape pattern scenario and the impact on habitat diversity? (2013).

26. Christina Fotiou: Evaluating habitat suitability and spectral heterogeneity models to predict weed species presence (2014).

27. Inese Linuza: Accuracy Assessment in Glacier Change Analysis (2014).

28. Agnieszka Griffin: Domestic energy consumption and social living standards: a GIS analysis within the Greater London Authority area (2014).

29. Brynja Guðmundsdóttir: Detection of potential arable land with remote sensing and GIS - A Case Study for Kjósarhreppur (2014).

30. Oleksandr Nekrasov: Processing of MODIS Vegetation Indices for analysis of agricultural droughts in the southern Ukraine between the years 2000-2012 (2014).

31. Sarah Tressel: Recommendations for a polar Earth science portal in the context of Arctic Spatial Data Infrastructure (2014).

32. Caroline Gevaert: Combining Hyperspectral UAV and Multispectral Formosat-2 Imagery for Precision Agriculture Applications (2014).

33. Salem Jamal-Uddeen: Using GeoTools to implement the multi-criteria evaluation analysis - weighted linear combination model (2014).

34. Samanah Seyedi-Shandiz: Schematic representation of geographical railway network at the Swedish Transport Administration (2014).

35. Kazi Masel Ullah: Urban Land-use planning using Geographical Information System and analytical hierarchy process: case study Dhaka City (2014).

36. Alexia Chang-Wailing Spitteler: Development of a web application based on MCDA and GIS for the decision support of river and floodplain rehabilitation projects (2014).

37. Alessandro De Martino: Geographic accessibility analysis and evaluation of potential changes to the public transportation system in the City of Milan (2014).

38. Alireza Mollasalehi: GIS Based Modelling for Fuel Reduction Using Controlled Burn in Australia. Case Study: Logan City, QLD (2015).

39. Negin A. Sanati: Chronic Kidney Disease Mortality in Costa Rica; Geographical Distribution, Spatial Analysis and Non-traditional Risk Factors (2015).

40. Karen McIntyre: Benthic mapping of the Bluefields Bay fish sanctuary, Jamaica (2015).

41. Kees van Duijvendijk: Feasibility of a low-cost weather sensor network for agricultural purposes: A preliminary assessment (2015).

42. Sebastian Andersson Hylander: Evaluation of cultural ecosystem services using GIS (2015).

43. Deborah Bowyer: Measuring Urban Growth, Urban Form and Accessibility as Indicators of Urban Sprawl in Hamilton, New Zealand (2015).

44. Stefan Arvidsson: Relationship between tree species composition and phenology extracted from satellite data in Swedish forests (2015).

45. Damián Giménez Cruz: GIS-based optimal localisation of beekeeping in rural Kenya (2016).

46. Alejandra Narváez Vallejo: Can the introduction of the topographic indices in LPJ-GUESS improve the spatial representation of environmental variables? (2016).

47. Anna Lundgren: Development of a method for mapping the highest coastline in Sweden using breaklines extracted from high resolution digital elevation models (2016).

48. Oluwatomi Esther Adejoro: Does location also matter? A spatial analysis of social achievements of young South Australians (2016).

49. Hristo Dobrev Tomov: Automated temporal NDVI analysis over the Middle East for the period 1982 - 2010 (2016).

50. Vincent Muller: Impact of Security Context on Mobile Clinic Activities A GIS Multi Criteria Evaluation based on an MSF Humanitarian Mission in Cameroon (2016).

51. Gezahagn Negash Seboka: Spatial Assessment of NDVI as an Indicator of Desertification in Ethiopia using Remote Sensing and GIS (2016).

52. Holly Buhler: Evaluation of Interfacility Medical Transport Journey Times in Southeastern British Columbia. (2016).

53. Lars Ole Grottenberg: Assessing the ability to share spatial data between emergency management organisations in the High North (2016).

54. Sean Grant: The Right Tree in the Right Place: Using GIS to Maximize the Net Benefits from Urban Forests (2016).

55. Irshad Jamal: Multi-Criteria GIS Analysis for School Site Selection in Gorno-Badakhshan Autonomous Oblast, Tajikistan (2016).

56. Fulgencio Sanmartín: Wisdom-volkano: A novel tool based on open GIS and time-series visualization to analyse and share volcanic data (2016).

57.

Nezha Acil: Remote sensing-based monitoring of snow cover dynamics and its influence on vegetation growth in the Middle Atlas Mountains (2016).

58. Julia Hjalmarsson: A Weighty Issue: Estimation of Fire Size with Geographically Weighted Logistic Regression (2016).

59. Mathewos Tamiru Amato: Using multi-criteria evaluation and GIS for chronic food and nutrition insecurity indicators analysis in Ethiopia (2016).

60. Karim Alaa El Din Mohamed Soliman El Attar: Bicycling Suitability in Downtown, Cairo, Egypt (2016).

61. Gilbert Akol Echelai: Asset Management: Integrating GIS as a Decision Support Tool in Meter Management in National Water and Sewerage Corporation (2016).

62. Terje Slinning: Analytic comparison of multibeam echo soundings (2016).

63. Gréta Hlín Sveinsdóttir: GIS-based MCDA for decision support: A framework for wind farm siting in Iceland (2017).

64. Jonas Sjögren: Consequences of a flood in Kristianstad, Sweden: A GIS-based analysis of impacts on important societal functions (2017).

65. Nadine Raska: 3D geologic subsurface modelling within the Mackenzie Plain, Northwest Territories, Canada (2017).

66. Panagiotis Symeonidis: Study of spatial and temporal variation of atmospheric optical parameters and their relation with PM 2.5 concentration over Europe using GIS technologies (2017).

67. Michaela Bobeck: A GIS-based Multi-Criteria Decision Analysis of Wind Farm Site Suitability in New South Wales, Australia, from a Sustainable Development Perspective (2017).

68. Raghdaa Eissa: Developing a GIS Model for the Assessment of Outdoor Recreational Facilities in New Cities Case Study: Tenth of Ramadan City, Egypt (2017).

69. Zahra Khais Shahid: Biofuel plantations and isoprene emissions in Svea and Götaland (2017).

70. Mirza Amir Liaquat Baig: Using geographical information systems in epidemiology: Mapping and analyzing occurrence of diarrhea in urban - residential area of Islamabad, Pakistan (2017).

71. Joakim Jörwall: Quantitative model of Present and Future well-being in the EU-28: A spatial Multi-Criteria Evaluation of socioeconomic and climatic comfort factors (2017).

72. Elin Haettner: Energy Poverty in the Dublin Region: Modelling Geographies of Risk (2017).

73. Harry Eriksson: Geochemistry of stream plants and its statistical relations to soil- and bedrock geology, slope directions and till geochemistry. A GIS-analysis of small catchments in northern Sweden (2017).

74. Daniel Gardevärn: PPGIS and Public meetings – An evaluation of public participation methods for urban planning (2017).

75. Kim Friberg: Sensitivity Analysis and Calibration of Multi Energy Balance Land Surface Model Parameters (2017).

76. Viktor Svanerud: Taking the bus to the park? A study of accessibility to green areas in Gothenburg through different modes of transport (2017).

77. Lisa-Gaye Greene: Deadly Designs: The Impact of Road Design on Road Crash Patterns along Jamaica’s North Coast Highway (2017).

78. Katarina Jemec Parker: Spatial and temporal analysis of fecal indicator bacteria concentrations in beach water in San Diego, California (2017).

79. Angela Kabiru: An Exploratory Study of Middle Stone Age and Later Stone Age Site Locations in Kenya's Central Rift Valley Using Landscape Analysis: A GIS Approach (2017).

80. Kristean Björkmann: Subjective Well-Being and Environment: A GIS-Based Analysis (2018).

81. Williams Erhunmonmen Ojo: Measuring spatial accessibility to healthcare for people living with HIV-AIDS in southern Nigeria (2018).

82. Daniel Assefa: Developing Data Extraction and Dynamic Data Visualization (Styling) Modules for Web GIS Risk Assessment System (WGRAS). (2018).

83. Adela Nistora: Inundation scenarios in a changing climate: assessing potential impacts of sea-level rise on the coast of South-East England (2018).

84. Marc Seliger: Thirsty landscapes - Investigating growing irrigation water consumption and potential conservation measures within Utah's largest master-planned community: Daybreak (2018).

85. Luka Jovičić: Spatial Data Harmonisation in Regional Context in Accordance with INSPIRE Implementing Rules (2018).

86. Christina Kourdounouli: Analysis of Urban Ecosystem Condition Indicators for the Large Urban Zones and City Cores in EU (2018).

87. Jeremy Azzopardi: Effect of distance measures and feature representations on distance-based accessibility measures (2018).

88. Patrick Kabatha: An open source web GIS tool for analysis and visualization of elephant GPS telemetry data, alongside environmental and anthropogenic variables (2018).

89. Richard Alphonce Giliba: Effects of Climate Change on Potential Geographical Distribution of Prunus africana (African cherry) in the Eastern Arc Mountain Forests of Tanzania (2018).

90. Eiður Kristinn Eiðsson: Transformation and linking of authoritative multi-scale geodata for the Semantic Web: A case study of Swedish national building data sets (2018).

91. Niamh Harty: HOP!: a PGIS and citizen science approach to monitoring the condition of upland paths (2018).

92. José Estuardo Jara Alvear: Solar photovoltaic potential to complement hydropower in Ecuador: A GIS-based framework of analysis (2018).

93. Brendan O'Neill: Multicriteria Site Suitability for Algal Biofuel Production Facilities (2018).

94. Roman Spataru: Spatial-temporal GIS analysis in public health – a case study of polio disease (2018).

95. Alicja Miodońska: Assessing evolution of ice caps in Suðurland, Iceland, in years 1986 - 2014, using multispectral satellite imagery (2019).

96. Dennis Lindell Schettini: A Spatial Analysis of Homicide Crime's Distribution and Association with Deprivation in Stockholm Between 2010-2017 (2019).

97. Damiano Vesentini: The Po Delta Biosphere Reserve: Management challenges and priorities deriving from anthropogenic pressure and sea level rise (2019).

98. Emilie Arnesten: Impacts of future sea level rise and high water on roads, railways and environmental objects: a GIS analysis of the potential effects of increasing sea levels and highest projected high water in Scania, Sweden (2019).

99. Syed Muhammad Amir Raza: Comparison of geospatial support in RDF stores: Evaluation for ICOS Carbon Portal metadata (2019).

100. Hemin Tofiq: Investigating the accuracy of Digital Elevation Models from UAV images in areas with low contrast: A sandy beach as a case study (2019).

101. Evangelos Vafeiadis: Exploring the distribution of accessibility by public transport using spatial analysis. A case study for retail concentrations and public hospitals in Athens (2019).

102. Milan Sekulic: Multi-Criteria GIS modelling for optimal alignment of roadway by-passes in the Tlokweng Planning Area, Botswana (2019).

103. Ingrid Piirisaar: A multi-criteria GIS analysis for siting of utility-scale photovoltaic solar plants in county Kilkenny, Ireland (2019).

104. Nigel Fox: Plant phenology and climate change: possible effect on the onset of various wild plant species' first flowering day in the UK (2019).

105. Gunnar Hesch: Linking conflict events and cropland development in Afghanistan, 2001 to 2011, using MODIS land cover data and Uppsala Conflict Data Programme (2019).

106. Elijah Njoku: Analysis of spatial-temporal pattern of Land Surface Temperature (LST) due to NDVI and elevation in Ilorin, Nigeria (2019).

107. Katalin Bunyevácz: Development of a GIS methodology to evaluate informal urban green areas for inclusion in a community governance program (2019).

108. Paul dos Santos: Automating synthetic trip data generation for an agent-based simulation of urban mobility (2019).

109. Robert O' Dwyer: Land cover changes in Southern Sweden from the mid-Holocene to present day: Insights for ecosystem service assessments (2019).

110. Daniel Klingmyr: Global scale patterns and trends in tropospheric NO2 concentrations (2019).

111. Marwa Farouk Elkabbany: Sea Level Rise Vulnerability Assessment for Abu Dhabi, United Arab Emirates (2019).

112. Jip Jan van Zoonen: Aspects of Error Quantification and Evaluation in Digital Elevation Models for Glacier Surfaces (2020).

113. Georgios Efthymiou: The use of bicycles in a mid-sized city – benefits and obstacles identified using a questionnaire and GIS (2020).

114. Haruna Olayiwola Jimoh: Assessment of Urban Sprawl in MOWE/IBAFO Axis of Ogun State using GIS Capabilities (2020).

115. Nikolaos Barmpas Zachariadis: Development of an iOS, Augmented Reality for disaster management (2020).

116. Ida Storm: ICOS Atmospheric Stations: Spatial Characterization of CO2 Footprint Areas and Evaluating the Uncertainties of Modelled CO2 Concentrations (2020).

117. Alon Zuta: Evaluation of water stress mapping methods in vineyards using airborne thermal imaging (2020).

118. Marcus Eriksson: Evaluating structural landscape development in the municipality Upplands-Bro, using landscape metrics indices (2020).

119. Ane Rahbek Vierø: Connectivity for Cyclists? A Network Analysis of Copenhagen's Bike Lanes (2020).

120. Cecilia Baggini: Changes in habitat suitability for three declining Anatidae species in saltmarshes on the Mersey estuary, North-West England (2020).

121. Bakrad Balabanian: Transportation and Its Effect on Student Performance (2020).

122. Ali Al Farid: Knowledge and Data Driven Approaches for Hydrocarbon Microseepage Characterizations: An Application of Satellite Remote Sensing (2020).

123. Bartlomiej Kolodziejczyk: Distribution Modelling of Gene Drive-Modified Mosquitoes and Their Effects on Wild Populations (2020).

124. Alexis Cazorla: Decreasing organic nitrogen concentrations in European water bodies - links to organic carbon trends and land cover (2020).

125. Kharid Mwakoba: Remote sensing analysis of land cover/use conditions of community-based wildlife conservation areas in Tanzania (2021).

126. Chinatsu Endo: Remote Sensing Based Pre-Season Yellow Rust Early Warning in Oromia, Ethiopia (2021).

127. Berit Mohr: Using remote sensing and land abandonment as a proxy for long-term human out-migration. A Case Study: Al-Hassakeh Governorate, Syria (2021).

128. Kanchana Nirmali Bandaranayake: Considering future precipitation in delineation locations for water storage systems - Case study Sri Lanka (2021).

129. Emma Bylund: Dynamics of net primary production and food availability in the aftermath of the 2004 and 2007 desert locust outbreaks in Niger and Yemen (2021).

130. Shawn Pace: Urban infrastructure inundation risk from permanent sea-level rise scenarios in London (UK), Bangkok (Thailand) and Mumbai (India): A comparative analysis (2021).

131. Oskar Evert Johansson: The hydrodynamic impacts of Estuarine Oyster reefs, and the application of drone technology to this study (2021).

132. Pritam Kumarsingh: A Case Study to develop and test GIS/SDSS methods to assess the production capacity of a Cocoa Site in Trinidad and Tobago (2021).

133. Muhammad Imran Khan: Property Tax Mapping and Assessment using GIS (2021).

134. Domna Kanari: Mining geosocial data from Flickr to explore tourism patterns: The case study of Athens (2021).

135. Mona Tykesson Klubien: Livestock-MRSA in Danish pig farms (2021).

136. Ove Njøten: Comparing radar satellites. Use of Sentinel-1 leads to an increase in oil spill alerts in Norwegian waters (2021).

137. Panagiotis Patrinos: Change of heating fuel consumption patterns produced by the economic crisis in Greece (2021).

138. Lukasz Langowski: Assessing the suitability of using Sentinel-1A SAR multi-temporal imagery to detect fallow periods between rice crops (2021).

139. Jonas Tillman: Perception accuracy and user acceptance of legend designs for opacity data mapping in GIS (2022).

140. Gabriela Olekszyk: ALS (Airborne LIDAR) accuracy: Can potential low data quality of ground points be modelled/detected? Case study of 2016 LIDAR capture over Auckland, New Zealand (2022).

141. Luke Aspland: Weights of Evidence Predictive Modelling in Archaeology (2022).

142. Luís Fareleira Gomes: The influence of climate, population density, tree species and land cover on fire pattern in mainland Portugal (2022).

143. Andreas Eriksson: Mapping Fire Salamander (Salamandra salamandra) Habitat Suitability in Baden-Württemberg with Multi-Temporal Sentinel-1 and Sentinel-2 Imagery (2022).

144. Lisbet Hougaard Baklid: Geographical expansion rate of a brown bear population in Fennoscandia and the factors explaining the directional variations (2022).

145. Victoria Persson: Mussels in deep water with climate change: Spatial distribution of mussel (Mytilus galloprovincialis) growth offshore in the French Mediterranean with respect to climate change scenario RCP 8.5 Long Term and Integrated Multi-Trophic Aquaculture (IMTA) using Dynamic Energy Budget (DEB) modelling (2022).

146. Benjamin Bernard Fabien Gérard Borgeais: Implementing a multi-criteria GIS analysis and predictive modelling to locate Upper Palaeolithic decorated caves in the Périgord noir, France (2022).

147. Bernat Dorado-Guerrero: Assessing the impact of post-fire restoration interventions using spectral vegetation indices: A case study in El Bruc, Spain (2022).

148. Ignatius Gabriel Aloysius Maria Perera: The Influence of Natural Radon Occurrence on the Severity of the COVID-19 Pandemic in Germany: A Spatial Analysis (2022).

149. Mark Overton: An Analysis of Spatially-enabled Mobile Decision Support Systems in a Collaborative Decision-Making Environment (2022).

150. Viggo Lunde: Analysing methods for visualizing time-series datasets in open-source web mapping (2022).

151. Johan Viscarra Hansson: Distribution Analysis of Impatiens glandulifera in Kronoberg County and a Pest Risk Map for Alvesta Municipality (2022).

152. Vincenzo Poppiti: GIS and Tourism: Developing strategies for new touristic flows after the Covid-19 pandemic (2022).

153. Henrik Hagelin: Wildfire growth modelling in Sweden - A suitability assessment of available data (2023).

154. Gabriel Romeo Ferriols Pavico: Where there is road, there is fire (influence): An exploratory study on the influence of roads in the spatial patterns of Swedish wildfires of 2018 (2023).

155. Colin Robert Potter: Using a GIS to enable an economic, land use and energy output comparison between small wind powered turbines and large-scale wind farms: the case of Oslo, Norway (2023).

156. Krystyna Muszel: Impact of Sea Surface Temperature and Salinity on Phytoplankton blooms phenology in the North Sea (2023).

157. Tobias Rydlinge: Urban tree canopy mapping - an open source deep learning approach (2023).

158. Albert Wellendorf: Multi-scale Bark Beetle Predictions Using Machine Learning (2023).

159. Manolis Papadakis: Use of Satellite Remote Sensing for Detecting Archaeological Features: An Example from Ancient Corinth, Greece (2023).

160. Konstantinos Sourlamtas: Developing a Geographical Information System for a water and sewer network, for monitoring, identification and leak repair - Case study: Municipal Water Company of Naoussa, Greece (2023).

161. Xiaoming Wang: Identification of restoration hotspots in landscape-scale green infrastructure planning based on model-predicted connectivity forest (2023).

162. Sarah Sienaert: Usability of Sentinel-1 C-band VV and VH SAR data for the detection of flooded oil palm (2023).

163. Katarina Ekeroot: Uncovering the spatial relationships between Covid-19 vaccine coverage and local politics in Sweden (2023).

164. Nikolaos Kouskoulis: Exploring patterns in risk factors for bark beetle attack during outbreaks triggered by drought stress with harvester data on attacked trees: A case study in Southeastern Sweden (2023).

165. Jonas Almén: Geographic polarization and clustering of partisan voting: A local-level analysis of Stockholm Municipality (2023).

166. Sara Sharon Jones: Tree species impact on Forest Fire Spread Susceptibility in Sweden (2023).

167. Takura Matswetu: Towards a Geographic Information Systems and Data-Driven Integration Management. Studying holistic integration through spatial accessibility of services in Tampere, Finland. (2023).

168. Duncan Jones: Investigating the influence of the tidal regime on harbour porpoise Phocoena phocoena distribution in Mount’s Bay, Cornwall (2023).

169. Jason Craig Joubert: A comparison of remote sensed semi-arid grassland vegetation anomalies detected using MODIS and Sentinel-3, with anomalies in ground-based eddy covariance flux measurements (2023).

170. Anastasia Sarelli: Land cover classification using machine-learning techniques applied to fused multi-modal satellite imagery and time series data (2024).

171. Athanasios Senteles: Integrating Local Knowledge into the Spatial Analysis of Wind Power: The case study of Northern Tzoumerka, Greece (2024).

172. Rebecca Borg: Using GIS and satellite data to assess access of green area for children living in growing cities (2024).

173. Panagiotis–Dimitrios Tsachageas: Multicriteria Evaluation in Real Estate Land-use Suitability Analysis: The case of Volos, Greece (2024).

174. Hugo Nilsson: Inferring lane-level topology of signalised intersections from aerial imagery and OpenStreetMap using deep learning (2024).

175. Pavlos Alexantonakis: Estimating lake water volume fluctuations using Sentinel-2 and ICESat-2 remote sensing data (2024).

176. Karl-Martin Wigen: Physical barriers and where to find them (2024).

177. Martin Storsnes: Temporal RX-algorithm performance on Sentinel-2 images (2024).

178. Saulė Gabrielė Petraitytė: The Relation Between Covid-19 Vaccination and Voting Trends in Lithuania: A Spatial Analysis (2024).

179. Pedro Martinez Duran: Olive yield forecasting from remote sensing and climate datasets in the Jaen province (Spain) (2024).

180. Josefine Kynde Hämberg: Proximity to Urban Green Spaces for Older Adults in Specific Housings - a Case Study of Malmö, Sweden (2024).

181. Max Bengtsson: A Site Selection of An Energy Island in the North Sea: Optimal Location in an Ecological and an Economic Scenario Using a Multicriteria Decision Analysis (MCDA) (2024).

182. Anna Börmann: Assessing Great Britain as a relocation site for the threatened Iberian Lynx in a changing climate (2024).

183. Josephine Roosli: Flood Risk Assessment for the Kävlinge River for Present and Future Climate Scenarios using HEC-RAS Rain-on-Grid (2024).

184. Seán Flanagan: Spatiotemporal dynamics of E-scooter sharing ridership and their associations with the built environment: A Swedish comparative study (2024).

185. Wouter Vorsters: Assessing the Impact of Combined Sewer Overflow on the Habitat of Lampetra planeri: A Case Study in Flanders, Belgium (2025).

186. Kathleen Macdonald: Cetacean strandings on the Scottish coast: coastal accessibility factors lead to underreporting (2025).

187. Athanasios Emmanouil Mourampetzis: Navigating the Shadows: A Comparative Analysis of SAR and Optical Imagery for Detecting (Dark) Vessels (2025).

188. Nizam-ud-Din: Spatial Land Records System using Geospatial Techniques: a case study of a Mid-Sized Village in Pakistan (2025).

189. Nedim Nasic Kjellgren: Linked Geodata: Improving Rooftop Photovoltaic Production Estimates through BIM-GIS Integration using Semantic Web Technologies (2025).

190. Vedrana Pretkovic: Spatio-temporal vegetation changes in the Pacific-Chocó region of Colombia during the conflict and post-conflict periods (2025).

191. Evelina Bengtsson: A Socioeconomic Dimension of Crime: A Spatial Study of Firearm-related Violence in Malmö (2025).

192. Martynas Bielinis: Application of C-band Radar Interferometry for Dune Monitoring in the Curonian Spit (2025).

193. Paulina Magdalena Rieke: Case study of the benefits of BIM and GIS solutions used on a live infrastructure project (2025).

194. Alina Schärer: Evaluating the Impact of Urban Green Spaces and Vegetation Characteristics on Land Surface Temperature Across Swiss Cities Using Machine Learning (2025).

195. Paul Stewart: Where is wild in Glasgow’s Southside? A test of the applicability of relative wildness mapping to suburban Scotland (2025).

196. Georgios Fylakis: Spatiotemporal analysis of the integration between shared e-scooters and public transport: Case studies in Oslo and Stockholm (2025).

197. Andreas Klasson: Generating 3D building models according to Swedish building specification using footprints and airborne laser scanning (2025).

198. Agaton Järemo Lawin: The spread of Japanese knotweed in Scania: Invasion suitability prediction using species distribution modelling (2025).

199. Jesse Stewart: Contextualizing the Geographic Influence on Infantry Manoeuvrability in a Historical Battlefield Using GIS: A Case Study of the Canadian Corps in the Second Battle of Passchendaele, First World War (2025).

200. Oskar Vejkdal Thorsberg: Automatic geometry extraction in digital building permits: A case study using BIM and NS Building (2025).

201. Spyridon Gerafentis: Impact of the COVID-19 “Lockdown” on Air Quality in Athens (2025).

202. Symeon Andriotis: Political Violence in Athens, Greece (2008-2024): A Machine Learning Approach for Predictive Modelling of Spatial Risk Patterns (2025).

203. Simon Westman: Detecting Structurally Old Scots Pine: A Crown-Metric Approach Using National ALS and LIFT Enrichment (2026).

204. Freja Randeris Kristoffersen: Satellite-Derived Bathymetry of Danish Coastal Waters Using Machine Learning with Sentinel-2 and ICESat-2 data (2026).

205. Markus Honkanen: Securitas Per Scientiam: GIS-MCDA of Civil Defence Shelter Distribution Efficiency in the Helsinki Capital Region (2026).

206. Amanda Carolina Santos Motta: Visualization Tools for Simulation Results Based on 3D City Models: An Urban Planner-Focused Study (2026).

207. Gintars Krumins: Mapping forest felling activities in Latvia from Sentinel-2 satellite imagery using machine learning (2026).

208. Jenny Berntsson: Using Multi-criteria GIS analysis in nature conservation planning in Lilla Edet municipality (2026).

209. Sebastian Daland: Flood impacts on road accessibility and buildings in Gothenburg during a 100-year rainfall event (2026).

210. Polyxeni Karapanagiotidou: GIS-based Multi-Criteria Decision Analysis (MCDA) framework for Flood Risk Assessment in the Thermi Basin (2026).

211. Nour Abdulmagid A. Bensaid: Urban Expansion and its Relation to the Urban Heat Island Effect: A Case Study of Tripoli, Libya (2026).

212. Iris Krohn: Compound Extreme Events in Hamburg, Germany: A Flood Risk Assessment (2026).

213. Johan Wahlberg: Towards Data-Centric Geospatial Applications: A Knowledge Graph Approach to Road Maintenance in Stockholm, Sweden (2026).

214. Athanasios Fyntanidis: Towards Data-Centric Geospatial Applications: Machine Learning–Driven Assessment of Urban Heat Island Intensity in Athens: Integrating Remote Sensing, Landscape Metrics, and Green Infrastructure for Climate-Resilient Urban Planning (2026).